On the Manipulation of A Turbulent Boundary Layer by Unsteady Boundary Conditions

Thesis by
Cong Wang

In Partial Fulfillment of the Requirements for the
Degree of
Doctor of Philosophy

Caltech

CALIFORNIA INSTITUTE OF TECHNOLOGY
Pasadena, California

2019
Defended May 29, 2019

ACKNOWLEDGEMENTS

program. I am thankful to the amazing colleagues in this program, Brian Schmidt, David Huynh, Yichuan Song, Arnold Deffo, Akshay Sridhar and Joel Lawson, from whom I learned the joy of helping others. Support for this research work through the Office of Naval Research under grant N00014-15-1-2479 was greatly appreciated.

I want to thank friends I made over the years. I had the great fortune to over-lap with talented group members, including Nathan Martin, Chirs Roh, Morgane Grivel, Damian Hirsch, Jinglin Huang, Manuel Bedrossian, Christopher Dougherty, Cecilia Huertas-Cerdeira, Emile Oshima, Alexandros Rosakis and Marcel Veismann. We always had fun memories at beer hour, the annual APS trip and parties at Mory's house. I am indebted to Nathan and Jinglin, who were always willing to help whenever I asked. Out of lab, I thank my friends since my first year at Caltech, Yuchen Wei, Pengfei Sui and Xiaoxing Xia. My three-years roommate Cheng Li, with whom I can always discuss fluid mechanics. Especially, I want to thank my lab buddy and best man at my wedding Chris Roh, who always supports me and positively influences me. I always look for Chris when I am confused or excited about fluid mechanics. It is through discussion with him that many ideas in this thesis were inspired.

I would like to thank my parents, Mingdong Wang and Cuiling Xu, who have always been the source of unlimited and unconditional love. My parents' characters have deeply influenced me since childhood. It is through their example I learned to be honest, love life and love others. They always try their best to create a positive environment for me. They are the ultimate reason that I can come to Caltech and take the challenge to pursue this degree.

Finally, I could not have gone this far without my wonderful wife, Shanshan Chen, who always takes care of me and backs me up. She always has ideas of what we can do for fun. After I met her, my life become so much more meaningful and enjoyable. On rainy days, she is my shelter. Too many times when I am about to cry because of stress and frustration, she comforts me down by giving me a tight hug and telling me "do not worry, I am here". Her embrace is my relief at those moments. All along this journey, she has been my armor to move forward. I will never be able to thank her enough, but I will try with the rest of my life.

ABSTRACT

Reducing the frictional drag generated by a turbulent boundary layer (TBL) is critical for many engineering applications. Motivated by existing turbulent drag reduction methods, this study explores the possibility of sustaining wall-attached air-films and manipulating the near-wall turbulence in hydrodynamic TBL. An innovative air-retaining system is designed to sustain and dynamically modulate the wall-attached air-films in TBL. In still water, the oscillating air-films induce vortical motions in the near-region of air-films. In TBL, phenomena such as Stokes-type oscillatory motion, zero-shear-stress layer, 'inactive' turbulence and reduced viscous shear stress are observed in the vicinity region of air-films. The analysis shows that TBL momentum transfer toward the wall is suppressed and a turbulence re-laminarization mechanism is induced in the near-wall region. One potential physical mechanism points to the process of vorticity generation in the near-region of oscillating air-films, which 'pushes' the TBL near-wall vortical structures away from the wall. With this viewpoint, the phenomena mentioned above can be explained. The modified momentum transfer mechanism and turbulence re-laminarization process are shown to be the potential cause of suppressed viscous shear stress in the near-wall region. Estimated using the Clauser chart method, the turbulent wall-skin friction shows a noticeable decrease in the presence of air-films.

TABLE OF CONTENTS

LIST OF ILLUSTRATIONS

LIST OF TABLES

NOMENCLATURE

$()^+$.   Inner scaled quantity.

$()'$.   Turbulent fluctuation.

δ . Boundary layer thickness based on 99% of the free stream velocity.

δ^*.   Displacement thickness.

δ_0 . Baseline Boundary layer thickness based on 99% of the free-stream velocity.

δ_ν . Inner length scale $\delta_\nu = \frac{\nu}{u_\tau}$.

$\delta_{\nu 0}$. Baseline TBL inner length scale $\delta_{\nu 0} = \frac{\nu}{u_{\tau 0}}$.

$\langle \cdot \rangle$.   Phase average.

x, y, z . Streamwise, wall-normal, and spanwise directions.

μ . Dynamic viscosity.

ν . Kinematic viscosity.

ω_z . Transverse vorticity.

$\overline{()}$.   Time mean value.

ρ . Water density.

τ_w . Shear stress at the wall.

θ . Momentum thickness.

$\widetilde{()}$.   Periodically oscillatory motion.

A . Air-film oscillation amplitude.

a_1.   Townsend's structure parameter $a_1 = \frac{-\overline{u'v'}}{\overline{u'^2} + \overline{v'^2} + \overline{w'^2}}$.

C_{f0} . Baseline TBL skin friction coefficient.

C_f . Skin friction coefficient.

f . Air-film modulation frequency.

F_D . Form drag.

h . Air-film height.

H^* . TBL shape factor.

K . Free stream acceleration parameter $K = \frac{\nu}{U_\infty^2}\frac{dU_\infty}{dx}$.

k . Turbulent kinetic energy $k = \frac{1}{2}(\overline{u'^2} + \overline{v'^2} + \overline{w'^2})$.

K_l . Local acceleration parameter $K_l = \frac{\nu}{\overline{U}^2}\frac{d\overline{U}}{dx}$ with local mean velocity $\overline{U}$.

KP_{MO} . Kinetic energy transfer rate from mean motion to periodically oscillatory motion.

KP_{MT} . Kinetic energy transfer rate from mean motion to turbulent motion.

KP_{OT} . Kinetic energy transfer rate from periodically oscillatory motion to turbulent motion.

Re_τ . Friction Reynolds number $(\delta u_\tau/\nu)$.

Re_θ. Momentum thickness Reynolds number $(\theta U_\infty/\nu)$.

Re_o . Reynolds number based on the periodic oscillatory motion.

TBL. Turbulent boundary layer.

TKP . Turbulent kinetic energy production.

U, V, W. Instantaneous streamwise, wall-normal, and span-wise velocities.

u', v', w' . Streamwise, wall-normal, and spanwise velocity fluctuations.

U_∞ . Free stream velocity.

$u_{\tau 0}$. Baseline skin friction velocity.

u_τ . Friction velocity $\left(\sqrt{\tau_w/\rho}\right)$.

x_0^+, y_0^+. Length unit along the streamwise and wall-normal direction in the baseline TBL inner length scale.

Chapter 1

INTRODUCTION

Wall-bounded shear flows are of significant importance because they are intrinsically linked to many industrial applications, from over the surface of airplanes to those formed inside piping systems. At high Reynolds number, the shear flows become fully turbulent and the skin friction they exert on the wall surface drastically increases, when compared with the laminar case. One striking example is the turbulent boundary layer (TBL) generated over the surfaces of sea-crossing oil tankers. Previous research work found that turbulent frictional drag is responsible for up to 70% - 80% of total energy consumption for such surface vessels (Fukuda et al., 2000). To address this concern, many drag reduction methods have been developed over the past decades, which show the promising effect of suppressing the turbulent skin friction. The current understanding about the mechanism of wall friction points to vortical structures in turbulent shear flow Jiménez and Pinelli (1999). Fully resolving the complete mechanism is challenging, mainly due to the intrinsic unsteady and multi-scale nature of turbulent flow. This chapter will briefly review the fundamental concepts of TBL and a few typical turbulent drag reduction methods, which lay out the context for this thesis work. The approach of this thesis work is demonstrated thereafter.

In this thesis, the streamwise, wall-normal and spanwise directions are denoted by x, y and z, respectively. The streamwise, wall-normal and spanwise velocities are denoted by the capital letters U, V and W, respectively.

1.1 Background

Canonical Zero-Pressure-Gradient TBL

The canonical zero-pressure-gradient TBL is one of the simplest forms of wall-bounded turbulent flow. TBL is formed when viscous flow moves parallel to a smooth flat solid surface. In the near-wall region, the existence of solid wall slows down the flow speed. In fact, the flow velocity at the wall surface is forced to be zero, which is known as the 'no-slip' boundary condition. In regions far away from the wall, the flow is not influenced by the wall and acts like inviscid flow. It is known that all zero-pressure-gradient TBLs are self-similar, which are composed of an inner layer and an outer layer (AAR Townsend, 1980). To describe its self-similar

behavior, two sets of length and velocity scales are required. The choice of scales depends on the distance from the wall, denoted by y. In the inner layer, the flow viscosity v dominates the flow motion. Therefore, the velocity in the inner layer only depends on the wall-shear stress τ_w, viscosity v and the fluid density ρ. A viscous velocity u_τ and associated length scale δ_v can be defined, as shown in equation 1.1.

$$u_\tau = \sqrt{\frac{\tau_w}{\rho}}, \delta_v = \frac{v}{u_\tau} \qquad (1.1)$$

The velocity is often called frictional velocity and the length scale called viscous length scale. The scaling law for TBL inner layer mean streamwise velocity $\overline{U}$ and wall normal distance y can thus be defined as shown in equation 1.2, where the superscript '+' denotes normalized velocity and length. This scale set is often referred to as the TBL inner scale because of its scaling function for TBL inner layer.

$$\overline{U^+} = \frac{\overline{U}}{u_\tau}$$
$$y^+ = \frac{y}{\delta_v} \qquad (1.2)$$

The outer layer is in the region far away from the wall, where the viscosity effect is insignificant. The relevant length and velocity scale are the TBL thickness δ and the free stream velocity U_∞. The TBL thickness δ is defined as the y location at which the mean velocity profile attains 99% of the free stream value. An alternative choice for the outer layer length scale is the momentum thickness θ defined in equation 1.3,

$$\theta = \int_0^\infty \frac{\overline{U}}{U_\infty} \left(1 - \frac{\overline{U}}{U_\infty} \right) dy \qquad (1.3)$$

The Reynolds number based on momentum thickness is defined as $Re_\theta = \frac{U_\infty \theta}{v}$, which is frequently used to describe TBL.

If the difference between TBL inner scale and outer scale is large enough, i.e., $\frac{\delta}{\delta_v} = \frac{\delta u_\tau}{v} \gg 1$, an overlapping region between the inner layer and outer layer exists where both the inner scale and outer scale can be used to describe the flow behavior. This region is known as the log region because the non-dimensional velocity $\overline{U^+}$ is found to be a logarithmic function of y^+ in this layer (Millikan, 1939). The scaling

law in this region is often known as the *'log law'*, which is expressed in equation 1.4. The constant κ is known as the Kármán constant. For TBL, the commonly used values for κ and B are 0.41 and 5.0 (Coles, 1956).

$$U^+ = \frac{1}{\kappa} \log \left(y^+ \right) + B \tag{1.4}$$

The log law holds within the wall-normal range between 30 δ_ν and 0.3 δ (Pope, 2001). The existence of log law enables the calculation of friction velocity u_τ using the log layer velocity profile, the procedure of which is known as the Clauser chart method (Clauser, 1954). Clauser chart method determines wall frictional velocity by fitting the log region of velocity profile to a straight line with a fixed slope. More details about the canonical TBL can be found in the classical texts by AAR Townsend (1980) and Tennekes, John Leask Lumley, J. Lumley, et al. (1972).

Turbulent Drag Reduction Methods

Many promising drag reduction techniques have been developed, which can be approximately categorized as active or passive depending on whether extra energy consumption is required. In this section, a few drag reduction methods that are relevant to this thesis will be briefly reviewed.

Active Injection Methods

One popular active drag reduction method involves injecting elastic agents such as polymers into TBL. It was found that a TBL with very low polymer concentration can reduce frictional drag up to 80% Procaccia, L'vov, and Benzi (2008). Either rigid or elastic polymers can reduce turbulent frictional drag. However, elastic polymers have superior drag reduction effect. A similar trend was observed with injection of air-bubbles into TBL. Verschoof et al. (2016) found that deformable air-bubbles have stronger drag reduction effect (more than 40%) than rigid air-bubbles (4%). Elbing et al. (2008) found that when air-bubble volume concentration is large, the air-bubbles connect and form an air-layer which generates a high drag reduction effect (more than 80%). Recent reviews about the active injection method can be found in White and Mungal (2008) and Ceccio (2010).

The current understanding of the mechanism lies in the elastic agents interacting with TBL, which modifies the shear-generating structures Lu, Fernández, and Tryggvason (2005) examined the effect of a few deformable bubbles in channel flow. They found that the wall-skin friction is reduced by the entertainment of air-bubbles in the TBL

streamwise vortical structures. However, this effect was absent with non-deformable air-bubbles. Many models have been proposed to explain the mechanism. John L Lumley (1977) hypothesized that the elastic agents locally increase the TBL effective viscosity, which suppresses the turbulent fluctuation level. Meng and Uhlman (1989) proposed that energy is extracted from the turbulent flow during the process of air-bubbles splitting into two or more bubbles, which suppresses the turbulent fluctuations.

Constraints exist when it comes to applying the active injection methods to actual vessels. For the case of polymer injection, environmental contamination concern outweighs the drag reducing potential. In addition, extra energy consumption is always required for the injection process, which may compromise the actual energy saving.

Riblet and Super-hydrophobic Surface Method

Unlike active methods, passive drag reduction methods do not require energy input. Typical passive drag reduction methods often involve textured surfaces, such as riblet or a super-hydrophobic surface. Inspired by the fast swimmers in the biological world, such as sharks, surface-attached riblets that mimics shark skin were developed. The surface riblets are often two-dimensional and aligned in the flow direction. Typical drag reduction effect using riblets is generally around 10% (Garcia-Mayoral, Gómez-de-Segura, and Fairhall, 2019). It is found that riblets with certain geometrical dimension and spacing could effectively interact with the TBL near-wall vortical structures (Garcia-Mayoral and Jiménez, 2011), which could be the underlying mechanism for the observed drag reduction effect. A recent review of riblet method can be found in (Dean and Bhushan, 2010).

Another promising passive drag reduction method is through inducing slip-flow by maintaining a layer of low-viscosity fluid (i.e., air-film) at the wall, such as using a super-hydrophobic surface. Super-hydrophobic surface can entrap air bubbles in the surface air-pockets created by a dense distribution of surface roughness. The entrapped air bubbles together act like a lubricating layer, which allows the TBL flow to *'slip'* on top. The slip velocity offsets the shear strain rate and thus reduces the wall friction (Choi and C.-J. Kim, 2006). This effect is often known as the lotus-leaf effect, which is named after the phenomenon of water droplets rolling off plant leaves. The reported drag reduction effect by using a super-hydrophobic surface is very scattered, ranging from 10% - 75% under turbulent conditions (Ou and Rothstein,

2005; Park, Sun, et al., 2014; Bidkar et al., 2014). To understand the controversy in reported drag reduction effect, the interaction between the super-hydrophobic surface and TBL was numerically investigated (Seo, García-Mayoral, and Mani, 2015). Recent reviews on the super-hydrophobic surface for drag reduction can be found in Rothstein (2010) and Golovin et al. (2016).

The drag reduction effect of super-hydrophobic surface only exists when air-bubbles are entrapped in the surface air-pockets. However, air-bubbles are frequently depleted from the air-pocket by turbulent fluctuations or large wall-shear stress in high Reynolds number turbulent flow. Even without any air loss due to turbulent fluctuations, the air-bubbles diffuse away over time anyway (Choi and C.-J. Kim, 2006). The issue of air-bubble longevity challenges the super-hydrophobic surface drag reduction effect. In fact, if air-film is lost, the super-hydrophobic surface acts like a rough surface which induces more skin-friction drag (Bidkar et al., 2014). Therefore, it is challenging to sustain drag reduction effect by using a super-hydrophobic surface in high Reynolds number turbulent flow.

1.2   Approaches

One motivation for this thesis work is to address the challenges faced by the above-mentioned drag reduction methods, such as the energy consumption for active injection method and air-bubble sustainability for super-hydrophobic surface method. One design that can potentially satisfy such demand is shown by the schematic diagram in figure 1.1. First, over the flat surface, a dense distribution of closely-packed surface dimples (i.e., squares) is created to act as air-pocket containers. The dimples' inner surface is selectively coated with super-hydrophobic material (denoted by the forward stripes) while the outside surface remained untreated super-hydrophilic. Because of the sharp surface wettability gradient between the inner and outer surface of each dimple, when the surface is immersed in water, an air-water interface will form and pin at the edges of the dimple, as illustrated by the cross-sectional view along with the red dashed line. Therefore, the air-film tendency to reconnect to neighboring air-films is suppressed. Due to the surface dimple's small size, the stability of wall-attached air-films is enhanced by the surface tension effect.

Inspired by the success of surface textures (such as riblets) interacting with TBL and suppressing the shear-generating structures, the interaction between wall-attached air-film and TBL may reduce turbulent drag. Similar to the wall-attached riblets, the air-film geometry influences the air-film/TBL interaction. To control the air-
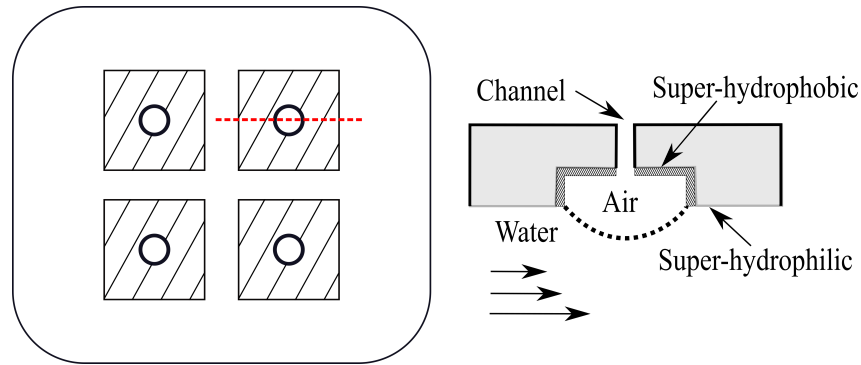
Figure 1.1: Schematic diagram showing the formation of air-films through creating square surface dimples and patterning surface wettability. Forward stripes represent super-hydrophobic surface. In the cross-sectional view, the air-film is pinned by the edge of surface dimple and denoted by the curved dashed line. An air-chamber is connected to the surface dimples through channels.

film/TBL interaction, the concavity of the air-film interface can be controlled by connecting the surface dimple to an air-chamber and regulating the air-chamber pressure. Figure 1.1 shows convex air-film protruding into TBL. The air-film can be maintained flat or concave (sagging into the dimple) as well with lower air-chamber static pressure. In addition, an extra beneficial point for having the air-chamber is that air-film can be promptly replenished when removed by severe turbulence or a prolonged diffusion process.

Furthermore, air-film/TBL interaction can be dynamically modified by incorporating a pressure source in the air-chamber. Driven by a periodically fluctuating air-chamber pressure, the wall-attached air-films oscillate and perturb the surrounding TBL. Analyzing the TBL dynamic response to the perturbations may reveal important information about the intrinsic nature of turbulent shear flow.

1.3   Objectives and Outline

This thesis focuses on investigating the air-film sustainability and understanding the TBL behavior in the presence of unsteady wall-attached air-films. The air-retaining system is designed and tested in various Reynolds number TBLs. The flow quantities are measured, and physical mechanisms behind the observed modifications are analyzed. The rest of this thesis is organized as follows.

Chapter 2 presents the air-retaining system design and experimental setup to test it in TBL. Chapter 3 analyzes the sustainability of air-films under various turbulence conditions. Chapter 4 presents modified TBL velocity profiles and turbulent stresses

under forcing conditions. Chapter 5 demonstrates that the observations in Chapter 4 are due to an unsteady vorticity field generated by oscillating air-films. Analysis of the momentum transfer process and a discussion of the generation of reduced wall-shear stress is also presented. Chapter 6 contains investigations of a case with stronger vorticity generation and Chapter 7 discusses the energy exchange process in this case and identifies a re-laminarization mechanism in the near-wall regions. Chapter 8 analyzes the potential drag reduction effect by the air-retaining system. Finally, Chapter 9 discusses the key non-dimensional parameters for the air-film/TBL interaction.

Chapter 2

EXPERIMENT SETUP

To test the air-film sustainability and investigate the air-film/TBL interaction, a canonical zero-pressure-gradient turbulent boundary layer was created in the free surface water tunnel facility in the Graduate Aerospace Laboratories at the California Institute of Technology. The detailed experimental design is presented in the following sections.

2.1 Water Tunnel Facility

A schematic diagram of the tunnel is shown in figure 2.1. The flow went through a 6:1 contraction before reaching the 2 m long, 1 m wide and 0.56 m deep test section. To suppress turbulent intensity in the bulk flow, the flow in the tunnel was conditioned by a perforated plate, a honeycomb, and three mesh screens with gradually reducing mesh size. With a fixed 0.45 m deep water, the tunnel can generate a bulk flow with a maximum velocity of approximately 0.9 m/s. Further increasing the tunnel pumping speed results in standing waves on the free surface, which may influence the experimental measurements. In the test section, the freestream turbulence intensity $\frac{\sqrt{(U-U_\infty)^2}}{U_\infty}$ was found to be less than 0.1%.
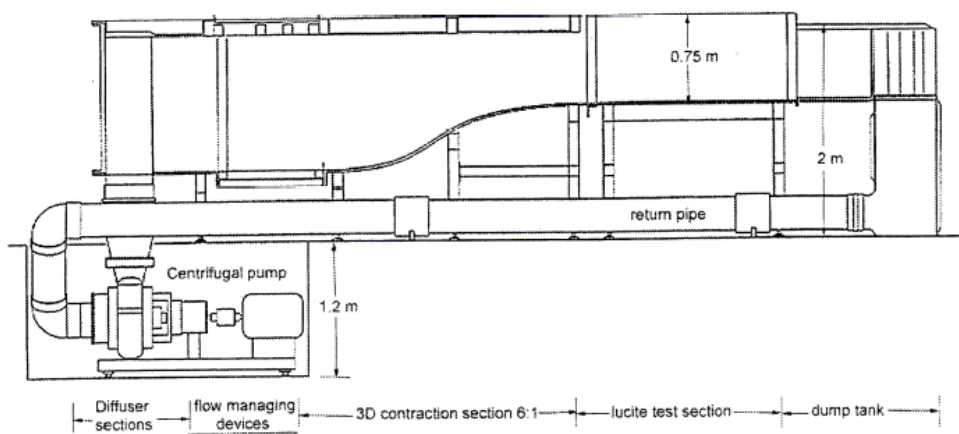
Figure 2.1: Schematic of the GALCIT free surface water tunnel

2.2 Air-film Cartridge

The air-retaining system was designed and 3-D printed in a cartridge form. The air-film cartridge consists of an air-pocket dimple surface, an air-chamber attached to the dimple surface and pressure source residing inside the air-chamber. A dimple surface model is shown in figure 2.2. The surface dimple was selected to be in a square shape for the convenience of close-packing. However, it can be of any geometrical shape. The square length l and gap distance d between neighbouring dimples determine the ratio of air-film area to the total surface area. To maintain a constant air-film coverage ratio for all dimple designs, the ratio d/l was maintained equal to 0.2 for all surface dimple designs. Therefore, air-films always covered 80% of the total surface in all dimple surface designs. The dimple depth was set to be half of its length l. To minimize the three-dimensional effect, the number of dimples in the span-wise direction was set large. The dimple array streamwise span was varied in different designs. The dimensions of all dimple surface designs are shown in Table 2.1.
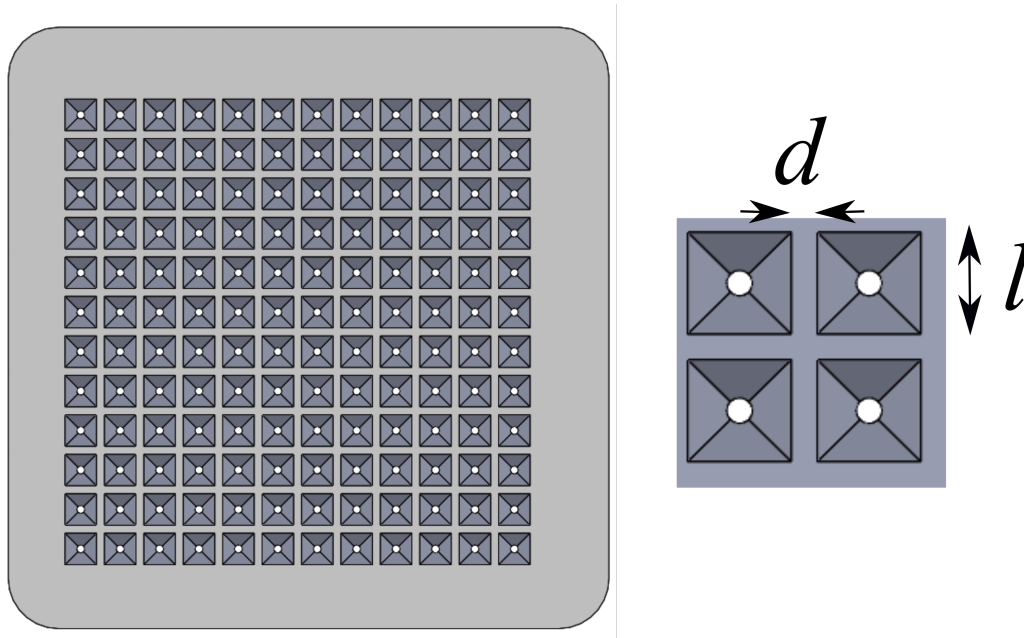
Figure 2.2: Schematic of dimple surface showing the dimensions of dimple array

To be compatible with the varied dimple surface dimensions, two different sized air-chambers were manufactured. One air-film cartridge model is shown in figure 2.3. The air-chamber had valves attached to its back wall which further connected it to an air-supply source and pressure controller. To adjust the air-chamber pressure, the valve for air-supply is first opened and air is pumped into water through surface

Air-pocket dimple	l (mm)	d (mm)	Dimple number (x × y)	Air-film array dimension (mm)	Air-film coverage ratio (%)
Design 1	8	2	3 × 12	30 × 120	80%
Design 2	4	1	10 × 24	50 × 120	80%
Design 3	8	2	5 × 12	50 × 120	80%
Design 4	8	2	12 × 12	120 × 120	80%

Table 2.1: Surface dimple dimensions

dimples. This operation pre-set the air-chamber pressure at a high level. The current pressure control is realized through a large-sized syringe which can add or remove air from the air-chamber. With the air-supply valve turned off, the pressure controller valve is turned on to adjust air-chamber pressure until the desired air-film configuration is obtained. During the experiment, both valves are kept off to maintain constant static air-chamber pressure. No air-bubbles are injected into TBL during experiments.

To dynamically modulate air-films, speakers (Peerless 2-inch Full Range Woofer) were installed in the air-chamber as pressure source for dynamic modulation. The number of installed speakers varied depending on the air-chamber dimensions. Two speakers were installed in the chamber compatible with dimple surface **Design 1**, **2** and **3** and four were installed in the chamber for **Design 4** (the one shown in figure 2.3). After installing speakers, the air-chamber and dimple surface were locked together through screws and tapped holes. To seal the air-film cartridge, an O-ring was installed at the interface between air-chamber and dimple surface and grease was used to enhance air-tightness. This design allows an easy switch of different dimple surfaces.
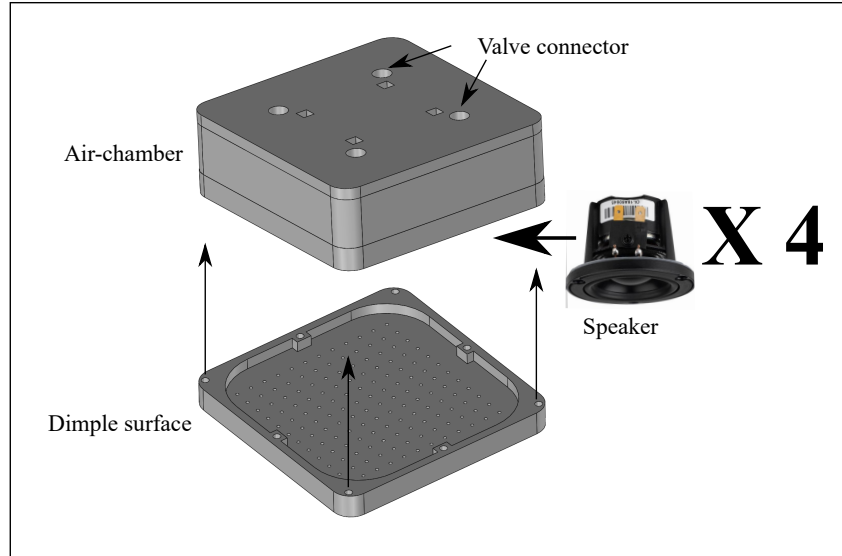
Figure 2.3: Air-film cartridge model with the **Design 4** dimple surface listed in Table 2.1. Speakers were used as pressure source. The valve connectors on the air-chamber connect to the air-supply and air-chamber pressure control unit.

2.3   Flat Plate for TBL Generation

To generate a zero-pressure-gradient TBL, a 170 cm long, 50 cm wide and 3 cm thick acrylic flat plate was designed and manufactured. The excellent light-passing property of acrylic material minimized the laser reflection at the flat plate surface. The assembled flat plate and air-film cartridge bottom view and side cross-sectional view are shown in figure 2.4. The coordinate system is also shown in the same figure, with the gravitational acceleration along the positive wall-normal (y) direction. The flat plate leading to trailing edge length was along the positive streamwise (x) direction and width along the transverse (z) direction following the right-hand rule. The dimpled surface was set facing downward so that the air-films were sustained beneath the flat plate bottom surface. With this orientation, the air-film dynamic oscillation was not disturbed by free surface waves and the buoyancy force enhanced the air-films' stability. The plate was suspended by truss structures from above the water tunnel and immersed at 0.15 m below the free surface. The water depth beneath the flat plate bottom surface was 0.3 m. Because the tunnel test section is wider than the flat plate, to ensure a uniform two-dimensional flow, the flat plate was sandwiched by two side walls of the same length as itself (shown in figure 2.4). The two side walls had sharp wedge-shaped leading edges to reduce potential leading-edge flow separation. The side walls were tightly locked to the flat plate (and the supporting structures) to reduce vibrations during experiments.

Because of its large size, the flat plate was manufactured in separated leading, middle and trailing parts that can be assembled to form a complete plate. The leading part has a 1:8 elliptical leading edge. Based on previous studies (Bobba, 2004), this design generates well-conditioned boundary layer at the leading edge. The turbulent transition was tripped at the plate leading edge bottom surface by a 4 mm wide and 2 mm thick tape across the flat plate transverse span. A central opening area in the middle part was created to fit the air-film cartridge. The air-film cartridge center was located at 75 cm downstream of the leading edge. According to (Bobba, 2004), TBL is fully developed with such developing distance.

For the convenience of assembling the flat plate, all flat plate parts had 2.5 cm wide (along the z direction) and 0.5 cm thick (along the y direction) side-sleeves. The sleeve upper surface coincides with the flat plate upper surface, which leaves 2.5 cm by 2.5 cm vacant region beneath the sleeves. Two parallel T-slotted frames that were 2 m long, 2.5 cm wide and 2.5 cm thick were used as supporting rails which fitted in the vacant region beneath side-sleeves. Therefore, all parts can rest on the supporting rails during the assembly process. To remove any potential 'steps' on the plate bottom surface, i.e., at the connecting edges of neighbor parts, spring washers were used to allow fine adjustments of the relative wall-normal position of any two neighboring parts. A 10 cm sharp-edged flap was mounted on the trailing edge of assembled plate. The flap angle relative to the flat plate was adjusted to set the leading edge stagnation point on the upper surface side, which was confirmed by dye visualization.

The air-retaining cartridge (highlighted in red color in figure 2.4) was fixed on a cartridge holder that can precisely fit into the central opening area of the flat plate. To align the dimpled surface with the flat plate bottom surface, the cartridge holder's vertical (wall-normal) position relative to the flat plate was adjusted by set screws along the four edges of cartridge holder. After fine adjustment, the holder was locked to the flat plate to avoid any potential relative movements during experiments.
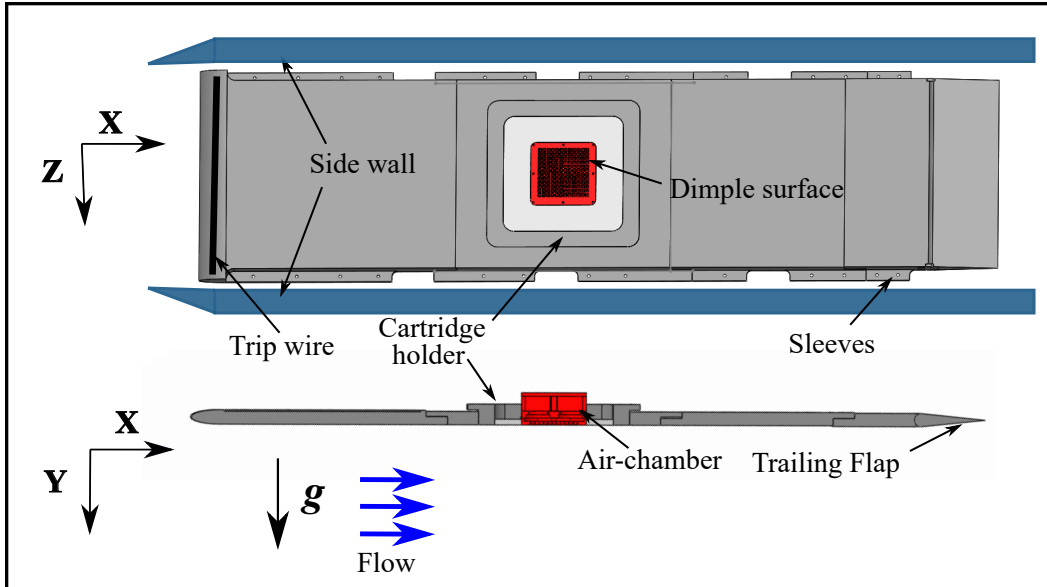
Figure 2.4: Bottom surface view and side cross-sectional view of assembled flat plate and air-film cartridge. Coordinate system and gravitational acceleration direction are also shown. The air-film cartridge is highlighted in red color.

2.4 Pressure Modulation

The modulation signal was generated using a National Instruments LabVIEW program. The signal was sent out by a NI-USB 6211 data acquisition (DAQ) card and amplified by a power amplifier before being fed into the speakers. The modulation function profile was selected to be in sinusoidal and saw-tooth shape, which are shown in figure 2.5. While the sinusoidal function is infinitely smooth, the sawtooth modulation function induces an abrupt pressure change in air-chamber. The modulation output power was set at two levels, i.e, 0.14 W and 0.56 W, which could influence the amplitude of the air-film oscillation. The modulation function had a sinusoidal shape and was at low output power setting unless specifically notified.

The pressure modulation signal frequency f was selected to allow oscillating air-films to interact with turbulent eddies. Two intrinsic frequencies that are respectively associated with the TBL inner and outer layer exist. Using the definition introduced in Chapter 1, the two intrinsic frequencies are expressed as $\frac{u_\tau}{\delta_\nu}$ and $\frac{U_\infty}{\delta}$. The modulation frequency was selected within the range defined by the two intrinsic frequencies. The intrinsic frequencies varied with TBL Reynolds number and are listed in Table 2.2. Modulation frequencies at 5 Hz, 20 Hz, 50 Hz and 100 Hz were selectively studied.

The effect of pressure modulation can be potentially influenced by air resonance
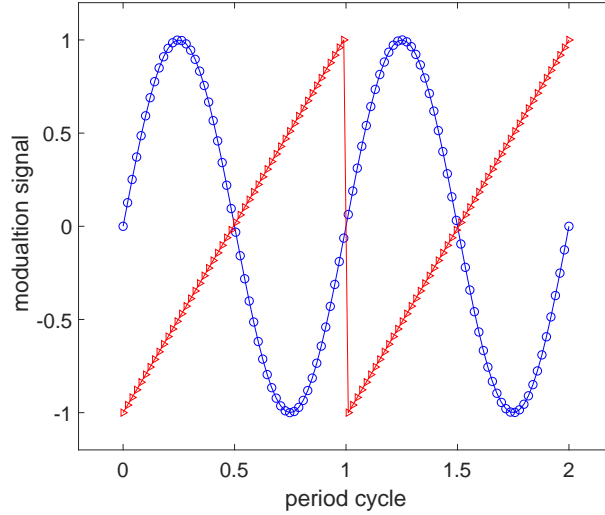
Figure 2.5: Sinusoidal and saw-tooth modulation function in two modulation cycles. Symbols: circle, sinusoidal signal, triangle, saw-tooth signal.

oscillation inside the surface dimple cavities, which is also known as 'Helmholtz resonance'. The Helmholtz resonance frequency depends on the surface dimple dimension and is expressed in equation 2.1:

$$f_H = \frac{1}{2\pi}\sqrt{\frac{\gamma_0 A_0^2 P_0}{m_0 V_0}} \tag{2.1}$$

where γ_0 is gas specific heat (equal to 1.4 for air), A_0 is dimple cross-sectional area. m_0, V_0, P_0 represent the air mass, volume and static pressure inside each dimple cavity. With the current 4 mm and 8 mm sized surface dimple, f_H is approximately 17000 Hz and 8500 Hz, respectively. Because the air oscillation resonance frequency is much larger than the selected modulation frequencies, the effect of resonance oscillation is expected to be insignificant.

2.5 Wall-Normal DPIV

Time-resolved 2D2C (two-dimensional velocity field with two in-plane components of velocity) DPIV (Digital Particle Image Velocimetry) was used to quantitatively map the flow field in the x-y plane. The flow was seeded with 13 um diameter silver-coated particles (Potters Industries LLC) that were neutrally-buoyant in water. The water flow was illuminated by a Coherent Verdi V6 continuous laser that has a maximum power of 6 W. The laser beam passed through a 300 mm focal length convex lens followed by a 20 mm focal length cylindrical lens to form an approximately 1 mm thick laser sheet. A high-speed camera (IDT camera Y7 model) was used to record particle images. The camera can take images at a recording speed up to 9000 frames per second with a full resolution of 1980×1080 pixels. The combination of continuous illumination and high-speed recording technique enables the investigation of TBL dynamic behavior at high-frequencies.

The DPIV cross-correlation was processed using commercial software PIVview (PIVTEC GmbH). The interrogation window dimension was set to be 128 by 48 pixel along the x- and y-directions, which ensured at least eight particles were included in each interrogation window all the time. The time interval between two cross-correlating images was selected such that the particle displacements were smaller than one-third of the window size along both directions. The vector fields were calculated using a multi-pass interrogation method. The neighboring windows overlapped 50% and 75% along the x- and y-directions. With such settings the DPIV cross-correlation is expected to produce reliable results(Raffel et al., 2018).

The DPIV experimental setup is depicted in the schematic diagram shown in figure 2.6. The laser head together with the optic lenses and camera were mounted on an optical table. The optical table could slide along the streamwise direction and measure flow fields at multiple streamwise locations. The horizontal laser beam was spread into a laser sheet and bent 90° up by a 45° flat mirror, which illuminated the bottom surface of flat plate. To diagnose the TBL variation in the transverse direction, the flat mirror was mounted on a transverse track and its transverse position can be easily adjusted.

The DPIV calibration was done using a calibration target with 0.5 mm diameter calibration marks that are equally spaced at 5 mm apart. The calibration target was mounted on a freely stand holder.To calibrate, the calibration target was put into the tunnel test section through the central opening area of flat plate and carefully aligned with the laser plane. To reduce calibration error, the average result of three
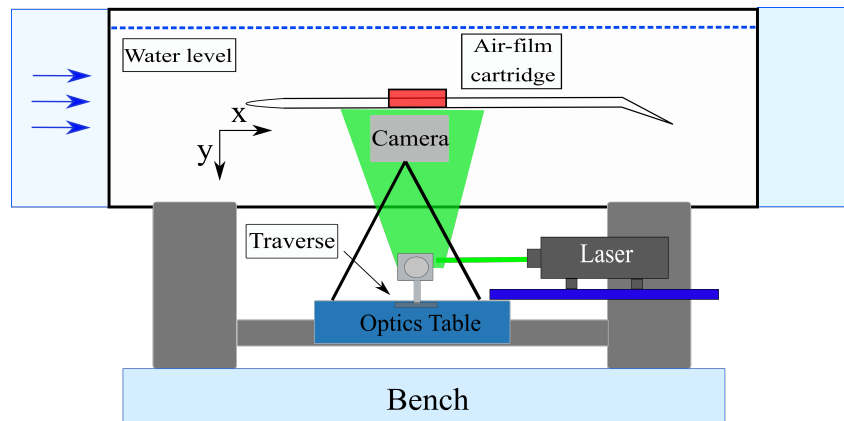
Figure 2.6: Schematic of wall-normal DPIV setup

calibration images were used for the calibration.

2.6 Measurement Synchronization

Because of the size limitation of camera field of view (FOV), not all the flow field of interest can be filmed within a single measurement, especially when the air-film array streamwise span is large. To address this concern, multiple DPIV measurements were carried out to cover all the regions of interest and a large FOV was assembled at the end. With pressure modulation, the assembled dynamic flow field can be obtained with synchronized DPIV measurements. To synchronize, all the measurement recordings were started at the same phase of pressure modulation. A timing diagram illustrating this process is given in figure 2.7. The DAQ card NI-USB 6211 internal sample clock continuously ran, which drove the pressure modulation and camera recording trigger signal at predetermined timings. To ensure a quasi-steady state flow field for all individual measurements, air-films were modulated for sufficient amount of time before particle images were recorded. As shown in figure 2.7, the air-films were first modulated for 40 seconds to allow the periodically perturbed flow field to fully develop. This time period was equivalent to at least 200 modulation cycles for the interested modulation frequencies. Because all the selected modulation frequencies were integers, 40 seconds cover an integer number of modulation cycles. After 40 seconds, the camera was triggered to record while the pressure modulation continued. Therefore, the camera recordings always started immediately after a complete modulation cycle. In this way the individual DPIV measurements were synchronized.

The internal sample clock of DAQ card runs at 20 MHz, which is much higher than the interested modulation frequency. The high-frequency internal sample clock

ensures the potential signal drifting to be trivial. The potential signal drifting is bound to be smaller than the period of internal sample clock, which is at most 0.001% of the interested modulation periods.
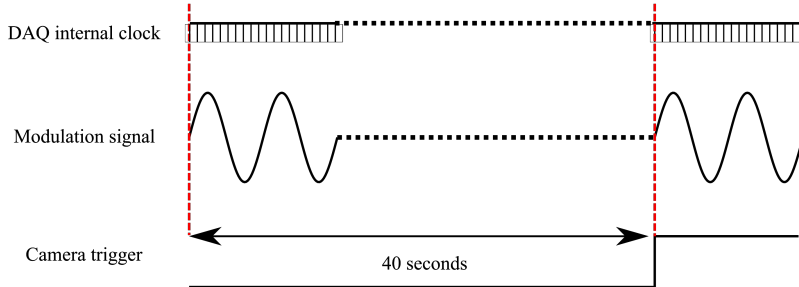
Figure 2.7: Timing diagram showing the synchronization of modulation signal and camera recording. Air-films were modulated for an integer number of cycles (in 40 seconds) before camera recording was triggered. Therefore the camera recording always started immediately after the completion of one modulation cycle.

For the convenience of analyzing the flow dynamic behavior under modulation, the camera frame rates were selected to be a multiple of the modulation frequency, ranging from 800 frames per second to 2000 frames per second. This gives an integer number of sample images in each modulation cycle which allows the flow field to be phase-averaged (details to be provided in section 2.7). To ensure enough data for phase-averaging, raw PIV image sequences equivalent to 200 to 1000 modulation cycles were recorded, depending on the modulation signal. The phase-averaged flow fields provided an alternative approach for synchronization. For example, the flow fields in two neighbouring FOVs can be synchronized by synchronizing the periodic flow motion at connecting edge of the two FOVs. This approach was used to verify the flow field synchronization. A photo for the DPIV and pressure modulation setup is shown in figure 2.8.

2.7 Triple-decomposition and Phase-average

The periodically modulated air-film injects a deterministic perturbation into TBL, the response to which can be extracted through phase-averaging the flow field measurements. The details about triple-decomposition and phase-average are given in this section.

A typical instantaneous turbulent flow quantity $f(x, y, t)$ can be Reynolds decomposed into its time mean $\overline{f(x, y)}$ and a corresponding randomly fluctuating $f'(x, y, t)$ i.e.,
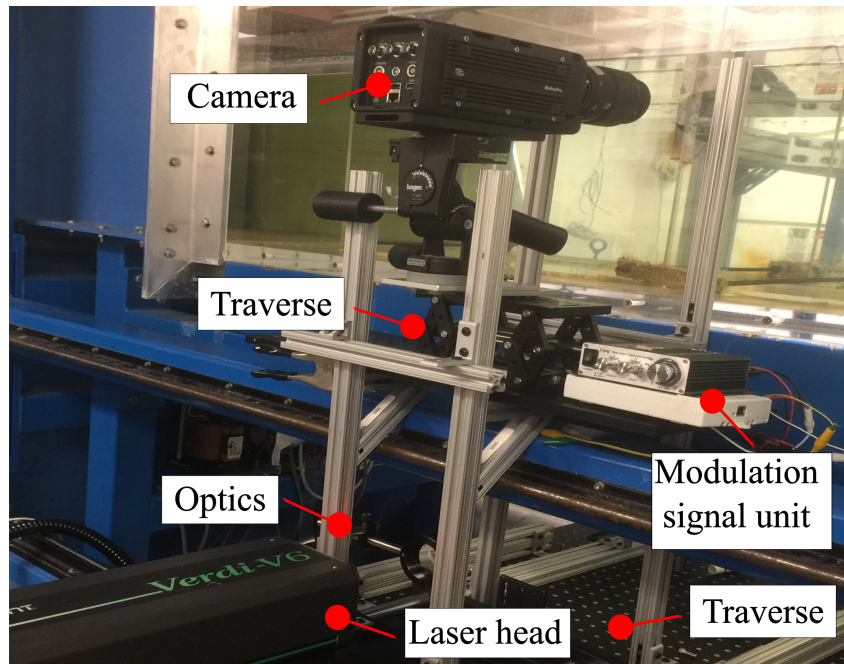
Figure 2.8: Photo of DPIV and pressure modulation experimental setup

$$f(x, y, t) = \overline{f(x, y)} + f'(x, y, t) \tag{2.2}$$

However, for a flow field that has a deterministic periodic component, such as the flow field in the near-region of modulated air-films, phase-averaged quantities can be obtained by only taking the average of flow measurements at the same phase with respect to the modulation signal. Therefore, in the presence of periodically modulated air-film, the flow quantity $f(x, y, t)$ can be conveniently decomposed into three parts: its time mean $\overline{f(x, y)}$, purely oscillatory fluctuation $\widetilde{f(x, y, t)}$ and random fluctuation $f'(x, y, t)$ with respect to the previous two, which is shown in equation 2.3

$$f(x, y, t) = \overline{f(x, y)} + \widetilde{f(x, y, t)} + f'(x, y, t) \tag{2.3}$$

The phase-averaged $f(x, y, t)$, denoted as $\langle f(x, y, t) \rangle$, is obtained by rejecting the random fluctuations $f'(x, y, t)$ in equation 2.3. Because $f(x, y, t)$ has a time-varying component with periodicity T, $\langle f(x, y, t) \rangle$ is expressed as in equation 2.4:

$$\langle f(x, y, t) \rangle = \overline{f(x, y)} + \widetilde{f(x, y, \phi_i)}, \phi_i \in [0, T] \tag{2.4}$$

Therefore, $\langle f(x, y, t) \rangle$ includes both the time mean $\overline{f(x, y)}$ and the periodic oscillatory motion $\widetilde{f(x, y, \phi_i)}$. The periodic oscillatory motion $\widetilde{f(x, y, \phi_i)}$ can be further extracted by subtracting the time mean $\overline{f(x, y)}$ from $\langle f(x, y, t) \rangle$. A few useful identities associated with triple-decomposition exist. For example, the time mean of $\widetilde{f}$ and f' as well as the phase-average of f' are all zero, i.e., $\overline{f} = \overline{f'} = \widetilde{f'} = 0$. Based on these identities, in the presence of two triply-decomposed independent variables f and g, the following equations automatically hold:

$$\langle \widetilde{f}g \rangle = \widetilde{f}\langle g \rangle, \quad (\overline{f}g) = \overline{f}\langle g \rangle, \quad \overline{\langle \widetilde{f}g' \rangle} = \overline{\widetilde{f}g'} = 0 \tag{2.5}$$

A. K. M. F. Hussain and W. C. Reynolds (1970) and W. Reynolds and A. Hussain (1972) presented a classical turbulent shear flow study using the technique of triple-decomposition and phase-average.

2.8 Baseline TBL

To generate a zero-pressure-gradient TBL, the flat plate central opening area is filled with a flat acrylic plate. After the flat surface was inserted, the two flat plate bottom surfaces were aligned by adjusting the two plates relative vertical position using set screws. The water tunnel free stream velocity U_∞ was set at 0.43 m/s, 0.59 m/s and 0.82 m/s. This velocity range was selected to fully extend the water tunnel's pumping capability while ensuring turbulence was sustained. The trailing flap angle was adjusted to eliminate the pressure gradient in TBL. The TBL free stream acceleration factor K ($\frac{dU_\infty}{dx} \frac{\nu}{U_\infty^2}$) was approximately 1×10^{-7}, which is considered zero-pressure-gradient according to De Graaff and Eaton (2000).

These three tested TBLs will be named **TBL 1**, **TBL 2** and **TBL 3** throughout this thesis, which corresponds to Reynolds numbers (Re_θ) equal to 1200, 1800 and 2200. The baseline TBL friction velocity ($u_{\tau 0}$) was estimated using the Clauser chart method mentioned in Chapter 1. The Clauser chart method uses an iterative fitting process to determine the location of log layer region. The final portion of the velocity profile used for determining $u_{\tau 0}$ was between 40 y_0^+ to 0.2 δ_0, well within the range of log layer defined by (Pope, 2001).

The DPIV measurement was conducted at 70 cm, 75 cm and 80 cm downstream of the leading elliptic edge to diagnose if TBL was fully developed. The wall-normal laser plane was set along the flat plate streamwise central line or at 7 cm off the central line to inspect TBL transverse uniformity.The mean flow velocity and Reynolds stress profiles are all similar at various streamwise and span-wise

locations, which indicates TBL is fully developed and transversely uniform at the measurement locations. The mean flow properties for baseline TBL are summarized in Table 2.2. The intrinsic TBL frequencies are also shown, which set the ranges for pressure modulation frequencies.

TBL	U_∞ (m/s)	δ_0 (mm)	$u_{\tau 0}$ (m/s)	δ_{v0} (um)	$\frac{U_\infty}{u_{\tau 0}}$	Re_θ	Re_τ	$\frac{U_\infty}{\delta_0}$ (Hz)	$\frac{u_{\tau 0}}{\delta_{v0}}$ (Hz)
TBL 1	0.44	23.5	0.02	46	22	1200	520	17	433
TBL 2	0.59	24.4	0.025	37	23.6	1800	660	23	680
TBL 3	0.82	25.4	0.034	27	24.1	2200	920	33	1260

Table 2.2: Baseline TBL mean flow properties

The mean flow properties of baseline TBL were normalized by TBL outer scale and compared with literature hot-wire measurement result at $Re_\theta = 1430$ (De Graaff and Eaton, 2000). Figure 2.9 shows the mean streamwise velocity $\overline{U}$, Reynolds normal stress $(\overline{u'^2})$ and $(\overline{v'^2})$ as well as Reynolds shear stress $(-\overline{u'v'})$ at 75 cm downstream of the plate leading edge. The mean streamwise velocity agrees well with the hot-wire results. The Reynolds stresses show discrepancy when compared with the literature result, probably due to the difference in Reynolds number and measurement techniques. The Reynolds stress profile peak locations generally agree with the hot-wire measurement.
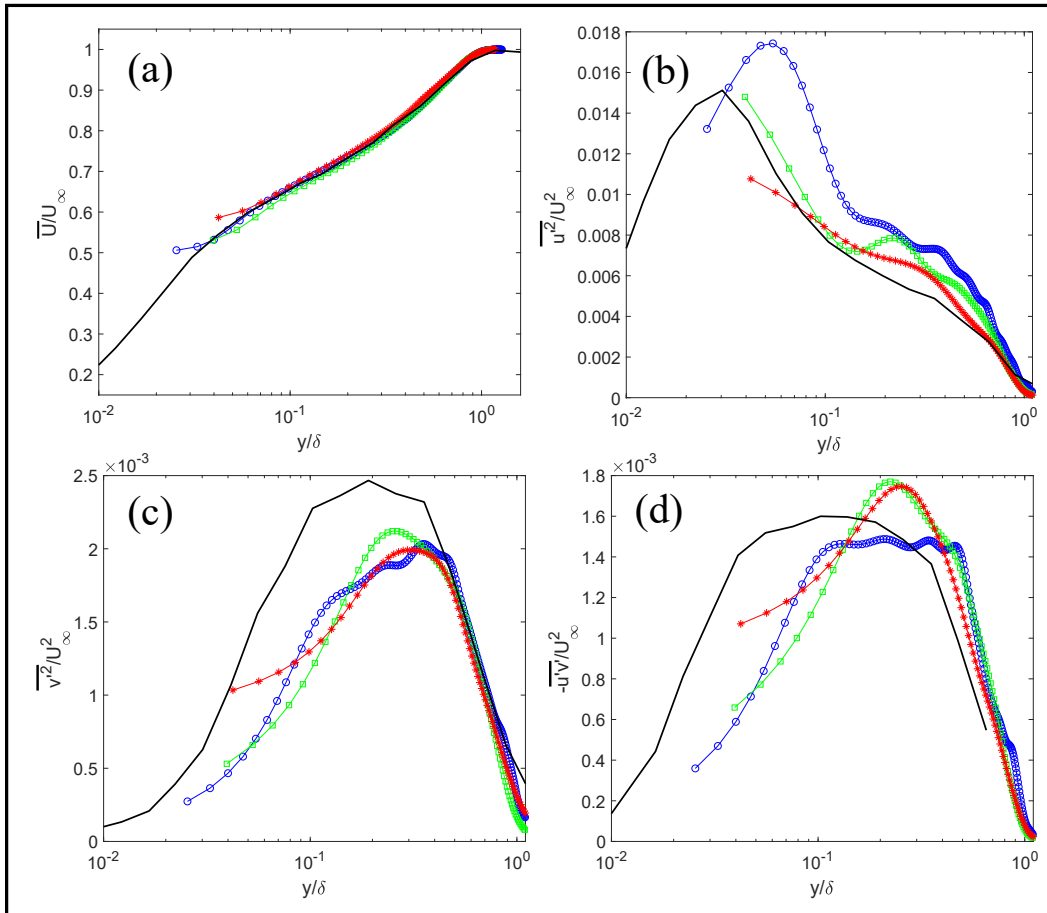
Figure 2.9: Baseline TBL mean flow velocity and Reynolds stress profiles non-dimensionalized by TBL outer scale: (a) $\overline{U}$, (b) $\overline{u'^2}$, (c) $\overline{v'^2}$, (d) $-\overline{u'v'}$. Symbols: circle, $Re_\theta = 1200$; square, $Re_\theta = 1800$; star, $Re_\theta = 2200$; Solid line, De Graaff and Eaton (2000) $Re_\theta = 1430$

C h a p t e r   3

AIR-FILM SUSTAINABILITY AND CONTROLLABILITY

The capability of air-film cartridge to sustain and modulate air-films is critical for its potential usability in manipulating turbulence, which essentially depends on whether the air-film remain wall-attached under external perturbations such as turbulent fluctuations. The air-film control mainly includes the control of its static and dynamic radius of curvature through controlling the air-chamber's static pressure and dynamic pressure respectively. In this chapter, the air-film sustainability and controllability in both still water and TBLs are studied.

3.1   Air-film in Still Water

The air-film sustainability and controllability were first studied without the water tunnel running. In this study, **Design 1** dimple surface was immersed in water, over which three 8 mm sized air-films formed along the x-direction. The air-film behavior was captured by a high-speed camera. In still water, air-film sustainability was high and could last several days without much loss due to air diffusion. The air-film was easy to control as well. The air-films pinned at the edges of dimples and their concavity configuration was easily adjusted to be flat or bulged out into still water by adding or removing air from the air-chamber. Because of the same-sized surface dimple, all the air-films had an identical static configuration.

To test the air-film dynamic controllability, the air-films were selectively modulated by a 50 Hz sinusoidal function. All air-films were periodically expanding and contracting in-phase following the pressure modulation. This process is depicted by tracking the air-film interface height as shown in figure 3.1. The air-film minimum and maximum bulging height were 1.5 mm and 1.9 mm respectively. Interestingly, the temporal variation of air-film interface height was found to be asymmetric, even under the effect of a symmetric modulation function. The air-film expansion phase took a longer time than the contraction phase. The average speed of air-film expansion and contraction were estimated to be 30 mm/s and 60 mm/s respectively.

The flow field induced by dynamically modulated air-films can be revealed by particle trajectories in the near-region of air-films (shown in figure 3.2), which are generated by overlaying particle images over 30 modulation cycles (0.6 seconds)
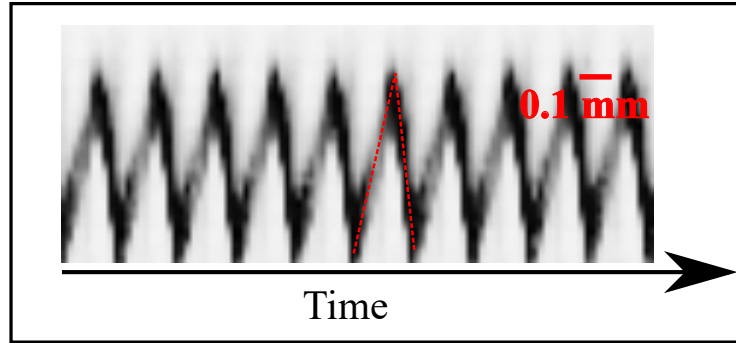
Figure 3.1: Tracked air-film interface temporal variation in still water under 50 Hz sinusoidal modulation. The air-film expansion and contraction phases are non-symmetric.

together. A vortical region was present over the central air-film, with its center located approximately 10 mm away from the wall. The vortical motion center is marked by a '+' sign and particle movement directions are shown by the arrows.
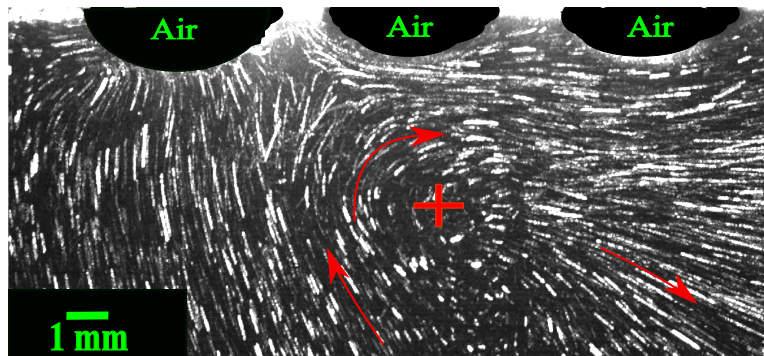
Figure 3.2: Particle trajectories in the vicinity of 50 Hz modulated air-films (formed over **Design 1** dimple surface) in still water. The particle trajectories are generated by overlaying particle images over 30 modulation cycles (0.6 seconds) together. The red arrow shows the particle movement direction.

Corresponding to the vortical motion, the mean transverse vorticity field ($\overline{\omega_z}$) over 500 modulation cycles (measured with DPIV) is shown in figure 3.3. The FOV is flipped upside-down when compared with that in figure 3.2 so that the wall is located at y = 0 mm. The air-films are between 4 mm and 32 mm along the bottom edge of FOV, as highlighted by the green half-ovals. Alternating-signed $\overline{\omega_z}$ is observed over the air-films. Positive $\overline{\omega_z}$ resides over the central region while negative $\overline{\omega_z}$ is observable near the edge regions. If the air-films are sustained in TBL, it is reasonable to deduce that the TBL vortical structures could be modified by the

patterned transverse vorticity.
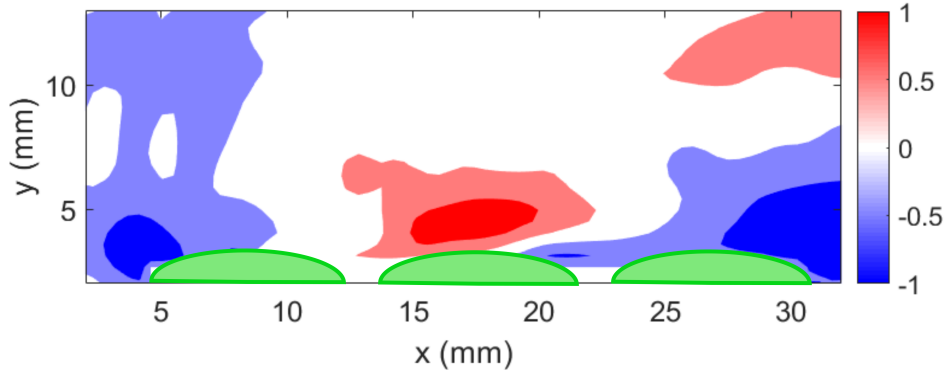
Figure 3.3: Mean vorticity ($\overline{\omega_z}$) contour (s^{-1}) in the vicinity region of 50 Hz modulated air-films showing alternating-signed vorticity pattern. Air-films are located between 4 mm and 32 mm along the figure bottom edge.

The physical mechanism of the transverse vorticity generation is worth discussing. In viscous flow, Lighthill (1963) visualized the solid boundary as a vorticity source and proposed the concept of *'vorticity flux'* for the vorticity production process. Gharib and Weigand (1996) derived an expression for the vorticity flux of surface-parallel vorticity (equivalent to transverse vorticity here) in a two-dimensional curvilinear coordinate system which is shown in equation 3.1.

$$\nu \frac{d\omega}{dr} = -\frac{du_s}{dt} - u_s \frac{du_s}{ds} - \frac{1}{\rho} \frac{dp}{ds} - g \cos(\Theta) \tag{3.1}$$

where (s, r) represents the local surface-tangential and surface-normal coordinates, ω and u_s are the surface-parallel vorticity and velocity components, respectively. p is the pressure at the surface, g is the gravitational acceleration and Θ is the angle between the surface and the gravitational acceleration. As shown in equation 3.1, vorticity flux can be generated by unsteady motions in the vicinity region of air-films. The detailed mechanism for the vorticity production process requires future in-depth studies.

3.2 Air-film in TBL

To examine the potential air-film depletion by turbulent fluctuations or shear stresses, both 8 mm and 4 mm sized air-films were first passively sustained in TBL with various Reynolds numbers. The passive air-films showed oscillation due to the near-wall turbulent fluctuations. In general, air-films remained attached to their dimple

cavities as long as their protrusion heights and oscillation amplitude was kept under certain limits. When the air-films' protruding height was too large for a given TBL, the air-films were severely distorted and eventually detached the dimples. The 4 mm sized air-film was more resistant to distortion and thus more stable than 8 mm sized air-films. The competing effect between distortion forces from TBL and air-film surface tension effect is critical for air-film sustainability.

The dynamics of air-film oscillation varied substantially depending on whether the air-film was passively sustained or actively modulated. Noticeably, the air-film oscillation amplitude depended on air-film concavity configuration.To qualitatively compare the air-film dynamics, the 8 mm air-film interface temporal oscillation in **TBL 1** ($Re_\theta = 1200$) was tracked and shown in figure 3.4. The air-films were either passively maintained flat or bulged, or actively modulated by 50 Hz sinusoidal function. The oscillating air-film interface was occasionally invisible due to not enough scattered light. For better visualization, the air-film interfaces are highlighted by red lines. The passive flat and bulged air-films both oscillated at random frequencies. However, the bulged air-films had larger oscillation amplitude. With 50 Hz modulation, the air-film interface demonstrated a dominant regularized 50 Hz oscillation. The oscillation period and magnitude may slightly vary in time, probably due to the effect of turbulent flow. The asymmetry in air-film expansion/contraction shown in figure 3.1 was still visible. These qualitative observations provide a crude idea about the unsteady and multi-frequency nature of air-film oscillation. By increasing the modulation output power, air-film oscillation amplitude was enhanced. However, the air-films tended to be more unstable and could break and generate scattered air-bubbles when the modulation power was too large.
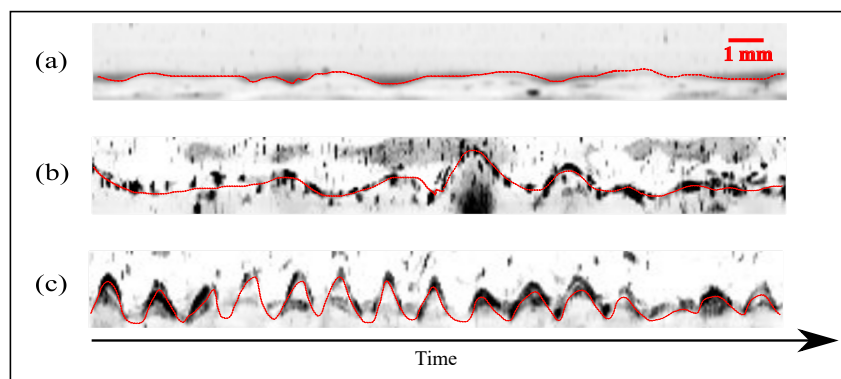
Figure 3.4: Tracked air-film interface oscillation over 0.3 seconds with unmodulated (a) flat air-film, (b) bulged air-film and (c) 50 Hz modulated bulged air-film. With 50 Hz modulation, the air-film interface demonstrates a regularized 50 Hz oscillation.

In the presence of 50 Hz modulated air-films, the TBL flow motion is greatly modified. Figure 3.5 depicts the particle trajectories in the presence of 50 Hz modulated air-films in **TBL 1** ($Re_\theta = 1200$). The particle trajectory visualization is generated by overlaying particle images over 0.01s (equivalent to half modulation cycle), which shows that particles near the modulated air-films did not flow parallel to the free stream. Instead, the flow field demonstrated strong wall-normal motions. The air-film interface curvature was locally distorted by the coupled air-film/TBL interaction. In the near-region of passive flat air-films which barely oscillate, such motions were not visible. The modified TBL may be related to the vorticity generated by oscillating air-films interacting with TBL vorticity field, which will be discussed in Chapter 5.
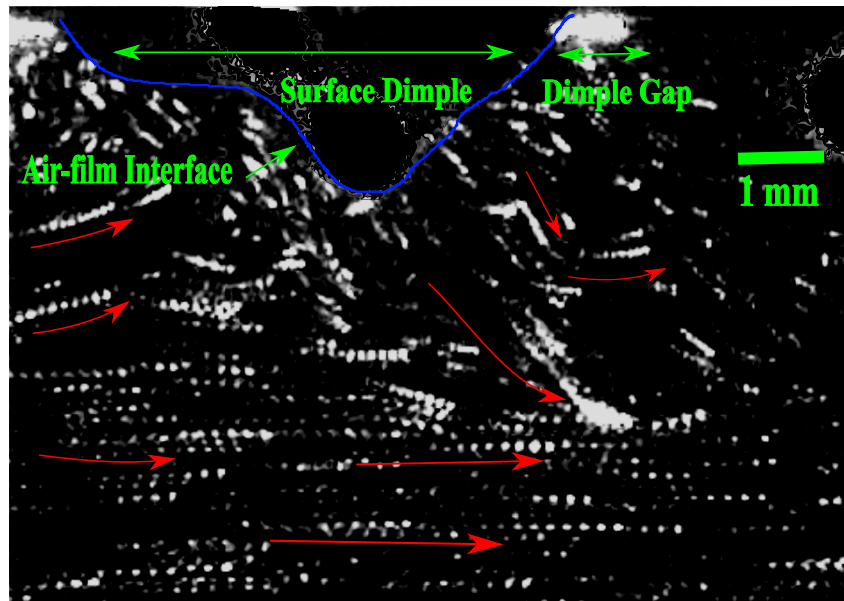
Figure 3.5: Particle trajectories in TBL ($Re_\theta = 1200$) near 50 Hz modulated air-films. The flow is from left to right and the air-film interface is highlighted by the blue curve. Particle trajectories are generated by overlaying particle images in 0.01 s (equivalent to half a modulation cycle)

Table 3.1 lists the air-film maximum height (h) and oscillation amplitude (A) with various modulation frequencies. The modulation function was sinusoidal and modulation output power was constant. No air-film depletion was observed in the listed cases. The air-film maximum height and oscillation amplitude are expressed in both real length unit (mm) and the baseline TBL inner length scale ($\delta_{\nu 0}$). It is found that the air-film maximum height in many cases was larger than 30 TBL inner units ($\delta_{\nu 0}$), which means the air-films could directly influence the TBL log region. The maximum air-film height was below 3 mm for all cases, which is around 1% of the

total water depth. The ratio of total air-film volume to the surrounding water volume is around 0.3%. Therefore, the potential blocking effect of air-film on bulk flow is insignificant.

Test case	Re_θ	Dimple size (mm)	Air-film con-cav-ity	f (Hz)	$\frac{f\nu}{u_{\tau 0}^2}$	h (mm)	h ($\delta_{\nu 0}$)	A (mm)	A ($\delta_{\nu 0}$)
1	1200	8	bulge	50	0.113	2.6	61	1.2	27
2	1200	8	bulge	20	0.045	2.7	59	0.8	17
3	1200	8	flat	50	0.113	1.7	30	1.3	12
4	1800	8	bulge	20	0.045	1.8	49	0.7	20
5	2200	8	bulge	50	0.113	2.8	105	1.0	38
6	2200	4	bulge	50	0.113	1.7	66	1.0	38

Table 3.1: Air-film maximum height (h) and oscillation magnitude (A) in TBL under various control conditions

The controllability of air-film depended on the TBL Reynolds number and air-film size. In high Reynolds number TBL, the air-film concavity configuration was harder to be maintained because of increased turbulent fluctuations. The dynamic modulation was less effective in higher Reynolds number TBL and the modulated air-film oscillation contained multiple random frequencies like the passive oscillation cases. The controllability of 4 mm air-film was better than 8 mm air-film, both statically and dynamically. These observations indicate that for the purpose of effective air-film control, the air-film size may need to be adjusted according to TBL Reynolds number.

In summary, the dynamics of wall-attached air-film interacting with both still water and TBLs are analyzed in this chapter. With pressure modulation, the air-films' oscillation followed the dynamic modulation frequency. In still water, modulated air-films generated patterned transverse vorticity in their near-regions. In TBLs with various Reynolds numbers, both 4 mm and 8 mm sized air-films remained wall-attached as long as their protrusion heights were limited. Passive air-films showed natural oscillations in TBL which depended on the air-film protrusion height. In the presence of 50 Hz modulated air-films, TBL flow motion is significantly modified. More quantitative studies of modifications in TBL will be presented in Chapter 4 and the physical mechanisms will be discussed in Chapter 5. .

C h a p t e r   4

UNSTEADY TBL IN THE PRESENCE OF AIR-FILM

The air-film oscillation brings about modifications to TBL, as was qualitatively shown by the particle trajectories in Chapter 3. This chapter selectively presents the **TBL 1** ($Re_\theta = 1200$) velocity and stress profiles in the presence of air-films formed over **Design 1** dimple surface, i.e, three 8 mm air-films exist along the streamwise direction. Table 4.1 lists the air-film array dimensions in the unit of baseline TBL inner unit (δ_{v0}) and outer unit (δ_0). Because the measurement field of view (FOV) was not large enough to cover all regions of interest, multiple measurements were stitched together to form a larger FOV. Expressed in baseline TBL inner scale (δ_{v0}) and marked by x_0^+ and y_0^+, the assembled FOV had a dimension of 3900 x_0^+ by 650 y_0^+, in which the air-films were located between 900 x_0^+ and 1500 x_0^+.

Length unit	Air-film size (l)	Air-film array x-span	Air-film array z-span
δ_{v0}	177	600	2440
δ_0	0.34	1.14	4.56

Table 4.1: Dimensions of the tested air-film (formed over **Design 1** dimple surface)

The air-films were maintained passively flat or bulged outward into TBL, or bulged outward and modulated by a 50 Hz sinusoidal function. The air-film interface temporal oscillation for these three cases was shown in figure 3.5, in which it can be seen that the air-films always protrude into TBL or remain flat but never sag into the surface dimples. The air-film maximum height (h) and oscillation amplitude (A) for the three test cases are summarized in Table 4.2. With 50 Hz modulation, the air-film maximum height (normalized by δ_{v0}) temporal variation in one modulation cycle is shown in figure 4.1. The air-film maximum height profile is non-sinusoidal and its initial contraction is drastic. As was presented in Chapter 2, with 50 Hz modulation the TBL dynamic ior can be extracted through phase-averaging the flow field. Because of the advantage of phase-average in revealing the flow dynamic behavior, the results in this chapter will be primarily based on the 50 Hz modulated bulged air-film case. To facilitate understanding, the results of two passive air-film cases will also be shown.

Air-film concavity	f (Hz)	h (mm)	h ($\delta_{\nu 0}$)	A (mm)	A ($\delta_{\nu 0}$)
flat	-	0.5	11	0.2	6
bulge	-	3.0	68	0.4	9
bulge	50	2.6	61	1.5	33

Table 4.2: The air-film maximum height (h) and oscillation amplitude (A) when it is passive flat, passive bulged or bulged and under 50 Hz modulation.
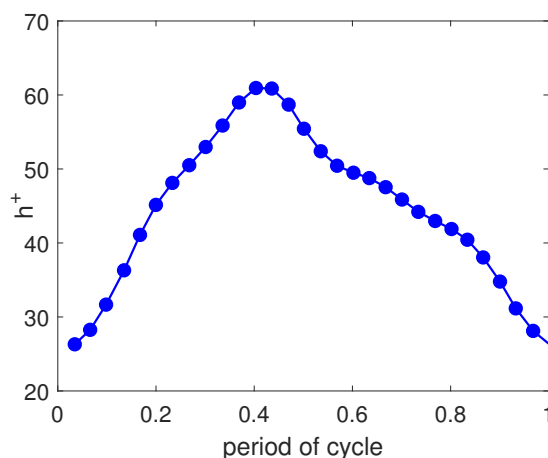
Figure 4.1: Non-dimensional air-film maximum height (h) over one modulation cycle (50 Hz)

4.1 Time-averaged Velocity Field

The time-averaged streamwise velocity ($\overline{U}$) measured in the air-film covered region is first analyzed. Figure 4.2 compares the velocity profiles (non-dimensionalized by TBL outer scale) in the presence of flat, bulged and 50 Hz modulated bulged air-films measured at 1400 x_0^+. The profiles of baseline TBL and literature hot-wire measurement at $Re_\theta = 1430$ are also shown. In the presence of 50 Hz modulated air-films, the near-wall velocity reduces while the slope of log region increases when compared with the baseline TBL. With unmodulated bulged air-film, the velocity profile exhibits similar but less obvious behavior. With unmodulated flat air-film, the velocity profile is no different from the baseline case.

The streamwise variation of ($\overline{U}$) profile in the presence of 50 Hz modulated air-film is investigated. Figure 4.3 shows the mean velocity profile versus wall normal distance (non-dimensionalized by TBL outer scale) at five streamwise locations, which are shown on the top axis. In regions close to the air-films, the near-wall velocity reduces and then gradually restores the baseline TBL downstream of air-films. Interestingly, the canonical log region seems to re-develop in the downstream
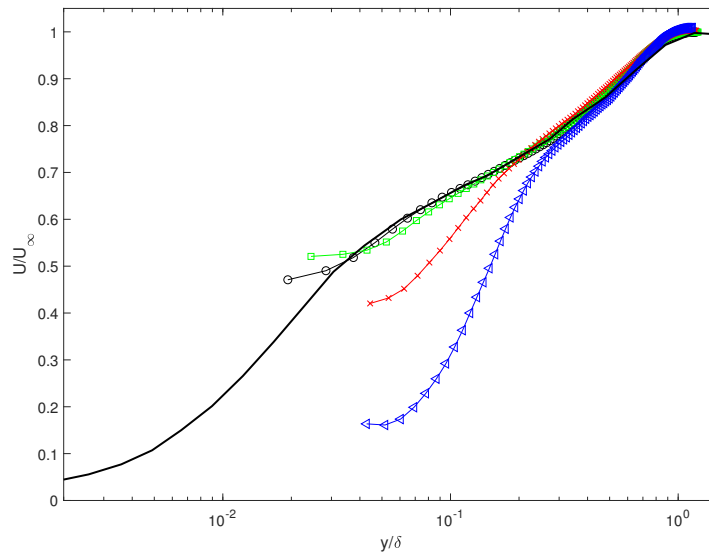
Figure 4.2: Mean streamwise velocity ($\overline{U}$) profiles at 1400 x_0^+. Air-films are located between 900 x_0^+ and 1500 x_0^+. Symbols: triangle, 50Hz modulated bulged air-film; cross, bulged air-film; square, flat air-film; circle, baseline TBL; solid line, $Re_\theta = 1430$ (De Graaff and Eaton, 2000)

of air-films.
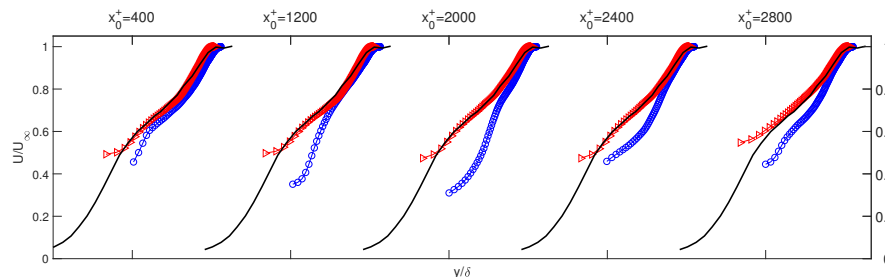
Figure 4.3: Mean streamwise velocity ($\overline{U}$) profiles streamwise variation. The streamwise locations are shown along the top axis. Air-films are located between 900 x_0^+ and 1500 x_0^+. Symbols: circle, bulged air-film with 50 Hz modulation; Triangle, baseline TBL; Solid line is from (De Graaff and Eaton, 2000)

The mean wall-normal velocities ($\overline{V}$) in the vicinity of air-films is also studied. In canonical flat plate TBL, $\overline{V}$ is hard to be physically measured due to its small magnitude. However, in the presence of dynamically modulated air-films, $\overline{V}$ is found much enhanced. The contour plots for $\overline{V}$ in the presence of various conditioned air-films are shown in figure 4.4, where the bulged air-films are highlighted by green half-ovals along the bottom edges of FOV. To avoid potential data discontinuity at the connecting edges of FOVs, the data in those regions is discarded. With 50 Hz

modulation (shown in figure 4.4 (a)), positive $\overline{V}$ is observed at the leading edge of air-films. However, negative $\overline{V}$ dominates the region downstream of air-films. The opposite-signed $\overline{V}$ resembles the flow field generated by a blowing and suction process at the wall. A similar behavior is also found in the vicinity of passive bulged air-films (shown in figure 4.4 (b)). However, such a phenomenon is not visible over flat air-films shown in figure 4.4 (c). The baseline flat plate TBL (shown in figure 4.4 (d)) has trivial $\overline{V}$, with a magnitude around 20 times smaller than that shown in figure 4.4 (a) and (b).
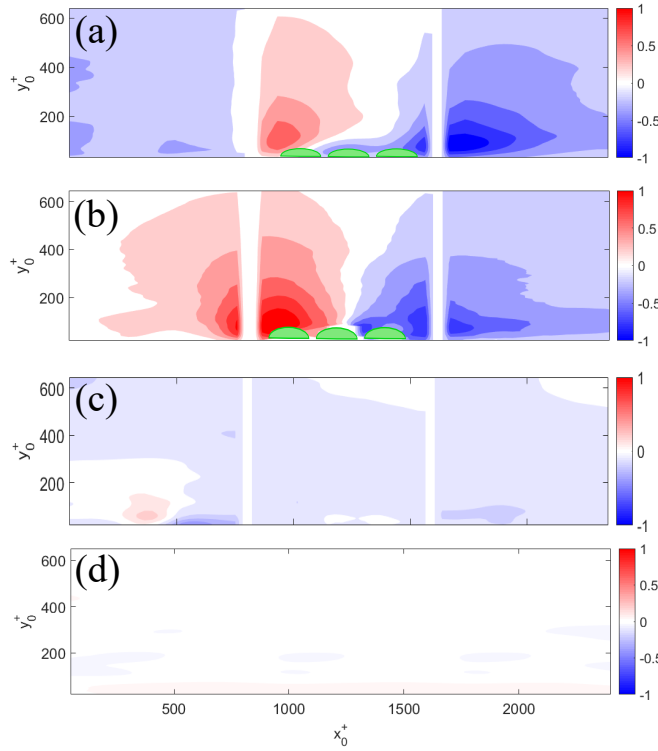
Figure 4.4: Mean wall-normal velocity ($\frac{\overline{V}}{u_{\tau 0}}$) contour over (a) 50 Hz modulated bulged air-film (b) passive bulged air-film (c) passive flat air-film and (d) baseline TBL. Air-films are located between 900 x_0^+ and 1500 x_0^+. Bulged air-films are represented by green half-ovals along the figure bottom edges.

4.2 Phase-averaged Velocity Field

With 50 Hz modulation, the phase-averaged velocity ($\overline{U} + \widetilde{U}$) profiles at 800 x_0^++ and 1550 x_0^+ (near the leading and trailing edges of air-films, respectively) are selectively examined, which periodically oscillate over time. Figure 4.5 shows the two $\overline{U} + \widetilde{U}$ profiles which mark the velocity oscillation range. The mean velocity profile ($\overline{U}$) is also shown. The baseline TBL velocity profile is also shown. It is found that $\overline{U} + \widetilde{U}$ profile periodically oscillates within 5% of the local mean velocity. At $1.3\delta_0$

away from the wall, the velocity oscillation range is approximately 2% of the mean streamwise velocity. The velocity oscillation amplitude is stronger at the trailing edge than at the leading edge of air-films. In addition, at the trailing edge of air-film the mean velocity $(\overline{U})$ substantially reduces in the near-wall region.
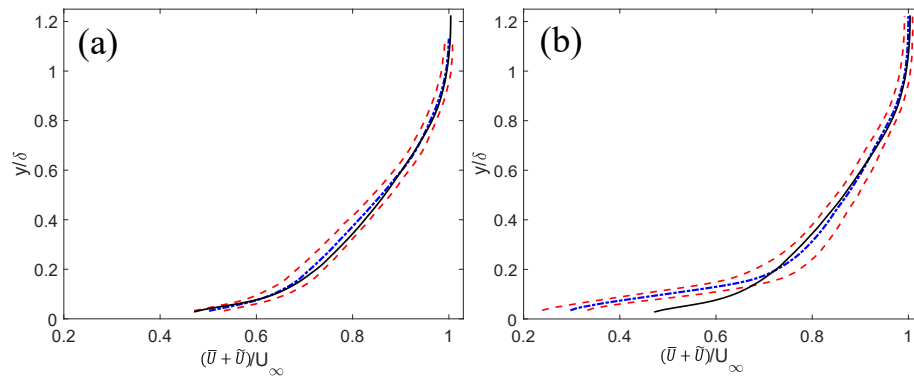
Figure 4.5: Phase-averaged streamwise velocity profile $(\overline{U}+\widetilde{U})$ showing the velocity profile oscillation range at the (a) leading edge (800 x_0^+) and (b) trailing edge (1550 x_0^+) of air-films. symbols: red dashed line, $\overline{U}+\widetilde{U}$ at two selected temporal phases that shows the velocity oscillation range; blue dotted-dash line, $\overline{U}$; black solid line, baseline TBL $\overline{U}$.

After subtracting the mean velocity profile $(\overline{U})$, the purely oscillatory $\widetilde{U}$ (non-dimensionalised by $u_{\tau 0}$) shown in figure 4.6 behaves like a Stokes boundary layer generated by a flat plate oscillating along the streamwise direction (C. Batchelor and G. Batchelor, 1967). $\widetilde{U}$ mainly exists in the near-wall region with a maximum oscillation amplitude approximately two $u_{\tau 0}$. The oscillatory motion behaves differently at leading and trailing edges of air-films. At the leading edge of air-films, $\widetilde{U}$ at different wall-normal distances oscillates in phase, i.e., at any instant the entire $\widetilde{U}$ profile resides on either the positive or negative side of the zero-mean. However, at the trailing edge of air-films, $\widetilde{U}$ at different heights may cross from the positive to the negative side, depicting an out-of-phase oscillation. At the leading edge, the largest oscillation amplitude is observed at the wall. However, at the trailing edge it is observed at approximately 30 y_0^+.
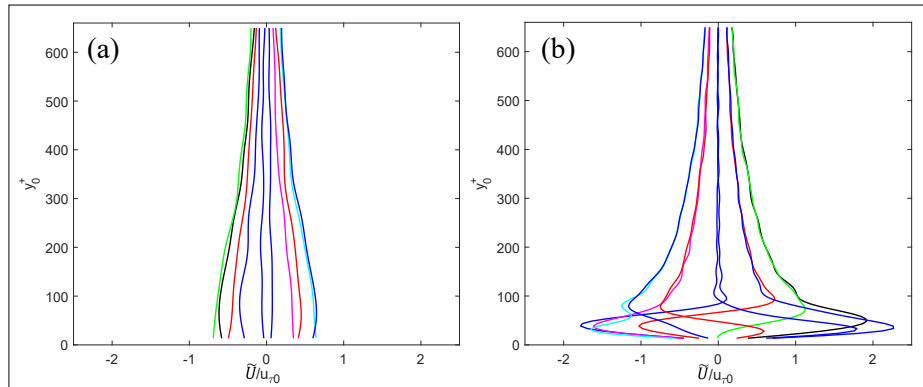
Figure 4.6: Streamwise oscillatory velocity ($\widetilde{U}$) profiles at the (a) leading edge (800 x_0^+) and (b) trailing edge (1550 x_0^+) of air-films resemble a Stokes boundary layer generated by a streamwise oscillating flat plate.

More details about the oscillatory motion can be seen in the phase snapshot contours of $\widetilde{U}$ and $\widetilde{V}$ shown in figure 4.7 and figure 4.8 respectively. The synchronized air-film maximum height (h) temporal variation is shown in the plots along the right edges of contours. Both $\widetilde{U}$ and $\widetilde{V}$ oscillate at a similar amplitude (approximately 2 $u_{\tau 0}$). However, their behaviors are very different. $\widetilde{U}$ amplitude is large at the leading and trailing edges of air-films. In contrast, $\widetilde{V}$ mainly exists in the region above air-films. $\widetilde{U}$ at the leading and trailing edges of air-films are always out of phase but $\widetilde{V}$ is always in-phase at all streamwise locations.

The oscillatory $\widetilde{U}$ and $\widetilde{V}$ closely follows the air-film expansion and contraction. During the air-film expansion phase, $\widetilde{U}$ is negative and positive at the leading and trailing edges of air-films respectively, mainly due to the 'push' effect generated by the air-films. Meanwhile, $\widetilde{V}$ is positive and gradually decays to zero when the air-film stops expanding. The opposite behaviors are observed when air-films contract.
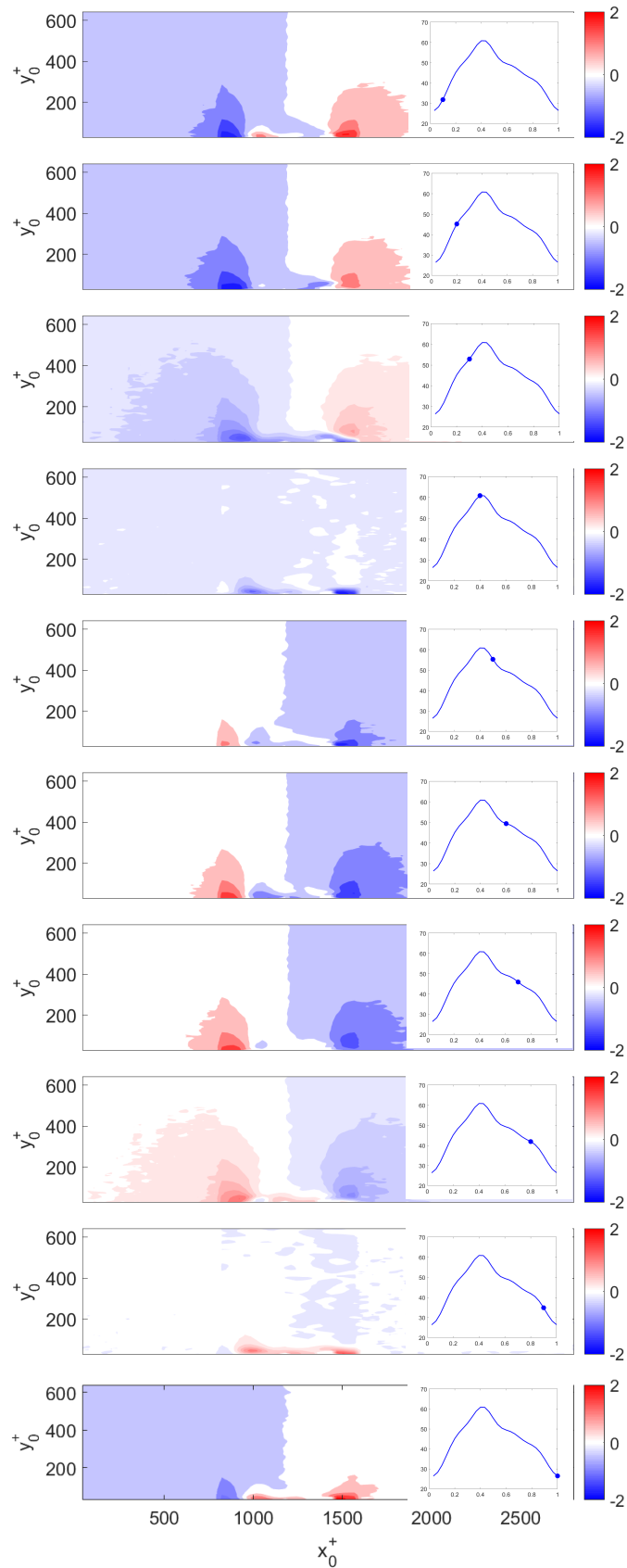
Figure 4.7: Phase snapshots for $\frac{\widetilde{U}}{u_{\tau 0}}$ synchronized with the air-film maximum height (h) periodic change in one modulation cycle. Air-films are located between 900 x_0^+ and 1500 x_0^+.
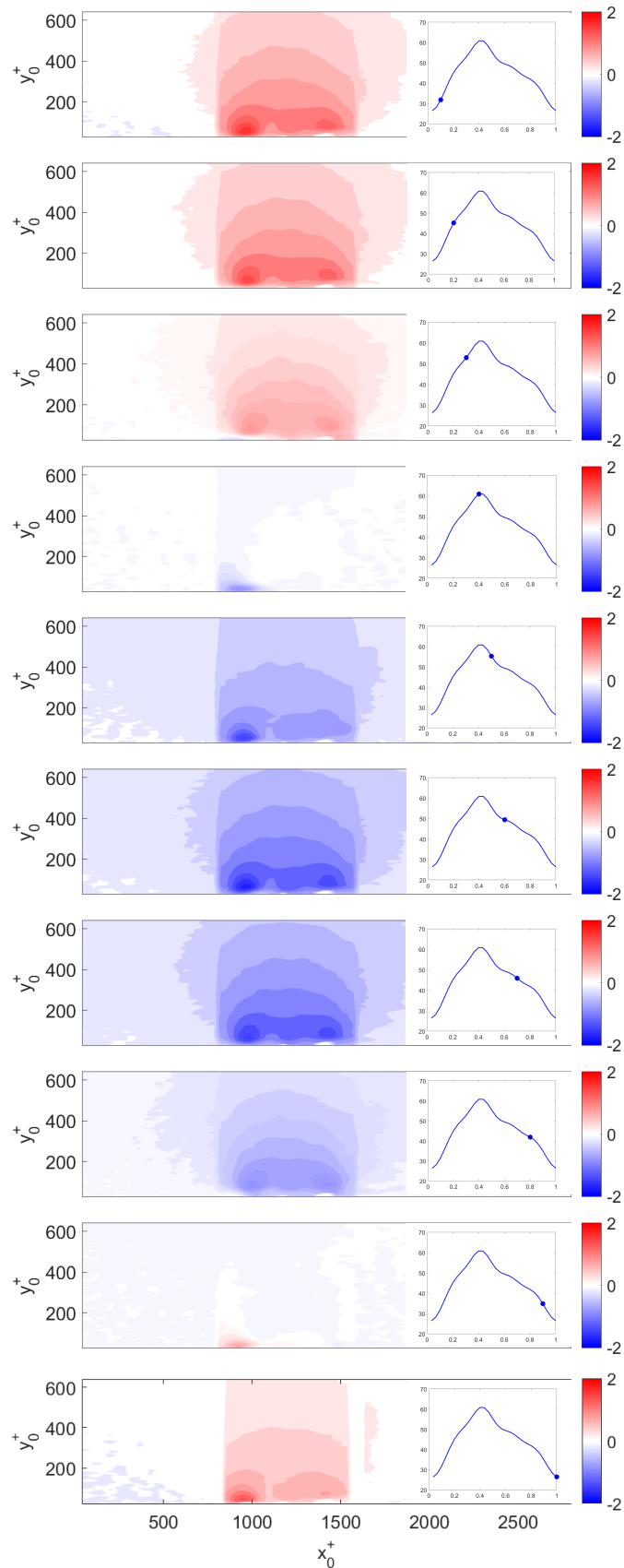
Figure 4.8: Phase snapshots for $\frac{\widetilde{v}}{u_{\tau 0}}$ synchronized with the air-film maximum height (h) periodic change in one modulation cycle. Air-films are located between 900 x_0^+ and 1500 x_0^+.

The correlation between $\widetilde{U}$ and $\widetilde{V}$ is worth analyzed. Figure 4.9 shows the phase snapshots for the non-dimensional $\widetilde{U}\widetilde{V}$. It is found that $\widetilde{U}\widetilde{V}$ is always negative at the leading edge but positive at the trailing edge of air-films, which points to a negative and positive correlation for $\widetilde{U}$ and $\widetilde{V}$ at the leading and trailing edges of air-films respectively. The periodically varying $\widetilde{U}\widetilde{V}$ is an organized shear motion, which can transfer streamwise momentum along the wall-normal direction. Further details about the momentum transfer process will be presented in Section 4.3.
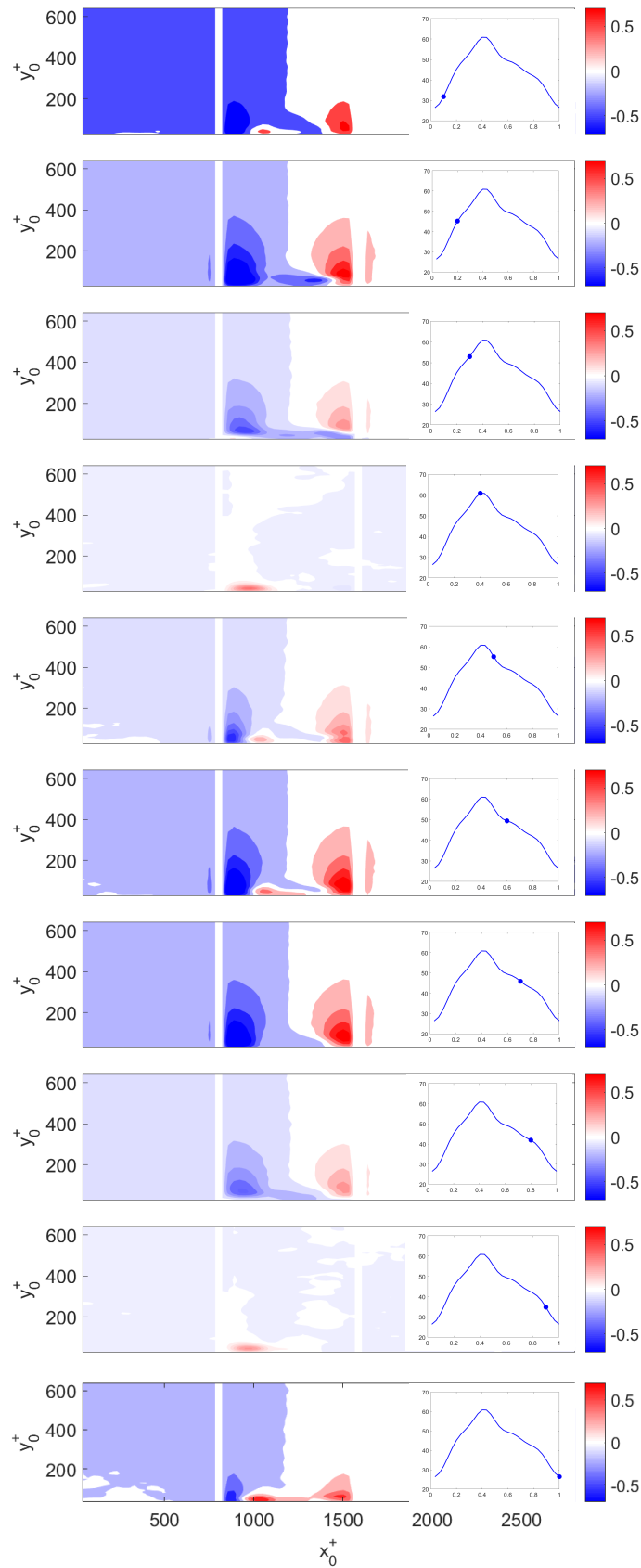
Figure 4.9: Phase snapshots for $\frac{\widetilde{U}\widetilde{V}}{u_{\tau 0 2}}$ synchronized with the air-film maximum height (h) periodic change in one modulation cycle. Air-films are located between 900 x_0^+ and 1500 x_0^+.

4.3 Zero-Shear-Stress Layer

In canonical flat plate zero-pressure-gradient TBL, the mean momentum is transferred toward the wall by the Reynolds shear stress $(-\overline{u'v'})$ and viscous shear stress $(\nu \frac{d\overline{U}}{dy})$. In most regions away from the wall, momentum is mainly transferred by Reynolds shear stress except in the near-wall region, where viscous shear stress takes over the responsibility of momentum transfer. In the presence of periodic modulation, besides the commonly observed Reynolds shear stress $(-\overline{u'v'})$, other shear motions such as $\widetilde{U}\widetilde{V}$ also can transfer TBL momentum. The total shear stress (τ_{total}) can be expressed in equation 4.1,

$$\tau_{\text{total}} = -\left(\overline{U} + \widetilde{U} + u'\right)\left(\overline{V} + \widetilde{V} + v'\right) \tag{4.1}$$

Expanding equation 4.1 and using the phase-average properties shown in equation 2.5, The time-average of the following cross products are identically zero:

$$\overline{\overline{U}v'} = \overline{\overline{V}u'} = \overline{\overline{U}\widetilde{V}} = \overline{\overline{V}\widetilde{U}} = \overline{\widetilde{U}v'} = \overline{\widetilde{V}u'} = 0 \tag{4.2}$$

Therefore, the time-averaged total shear stress is expressed as:

$$\overline{\tau}_{total} = -\left(\overline{UV} + \overline{\widetilde{U}\widetilde{V}} + \overline{u'v'}\right) \tag{4.3}$$

The three shear stress components will be referred to as Reynolds shear stress, wave shear stress and mean motion shear stress respectively.In an alternative way, the sum of all three shear stresses $(\overline{UV} + \overline{\widetilde{U}\widetilde{V}} + \overline{u'v'})$ is equivalent to the total flux of streamwise momentum transported in the wall-normal direction.

Figure 4.10 (a) - (d) shows the contour plots of $-\overline{u'v'}$, $-\overline{\widetilde{U}\widetilde{V}}$, $-\overline{UV}$ and the total shear stress (all non-dimensionalized by $u_{\tau 0}^2$) in the vicinity region of 50 Hz modulated air-films. Because $-\overline{UV}$ is of a larger magnitude than the other two shear stress components, the colour bar scale for $-\overline{u'v'}$ and $-\overline{\widetilde{U}\widetilde{V}}$ is set one order of magnitude smaller than $-\overline{UV}$ and total shear stress. The baseline TBL Reynolds shear stress $(-\overline{u'v'})$ and mean motion shear stress $(-\overline{UV})$ are plotted in the same scales as in figure 4.10 and shown in figure 4.11. When compared with the baseline case, Reynolds shear stress $(-\overline{u'v'})$ is slightly suppressed in the near-region above air-films (i.e., at approximately 75 y_0^+ over the air-films in figure 4.10 (a)) but greatly enhanced downstream of the air-films. In farther downstream region that is not shown here, the increased Reynolds shear stress extends for a distance of approximately three

boundary layer thicknesses (δ_0) before it relaxes to the baseline case. More details about $-\overline{u'v'}$ is presented in Section 4.4.

The wave shear stress ($-\overline{\widetilde{U}\widetilde{V}}$) comes from the correlated oscillatory $\widetilde{U}$ and $\widetilde{V}$ shown in section 4.2 and only exist in the near-region of air-film leading and trailing edges. Because of the opposite correlation at the leading and trailing edges of air-films, $-\overline{\widetilde{U}\widetilde{V}}$ shows opposite signs at the two locations. The magnitude of $-\overline{\widetilde{U}\widetilde{V}}$ is comparable to that of the local Reynolds shear stress ($-\overline{u'v'}$). $-\overline{UV}$ for the baseline TBL (shown in figure 4.11 (b)) is trivial when compared with figure 4.10 (c). The total shear stress is dominated by $-\overline{UV}$, which resembles the wall normal velocity ($\overline{V}$) shown in figure 4.4. In the region above air-films, the total shear stress is negative away from the wall but is positive in the near-wall region. The dividing line for oppositely signed shear stress is marked by black dotted lines shown in figure 4.10 (d).
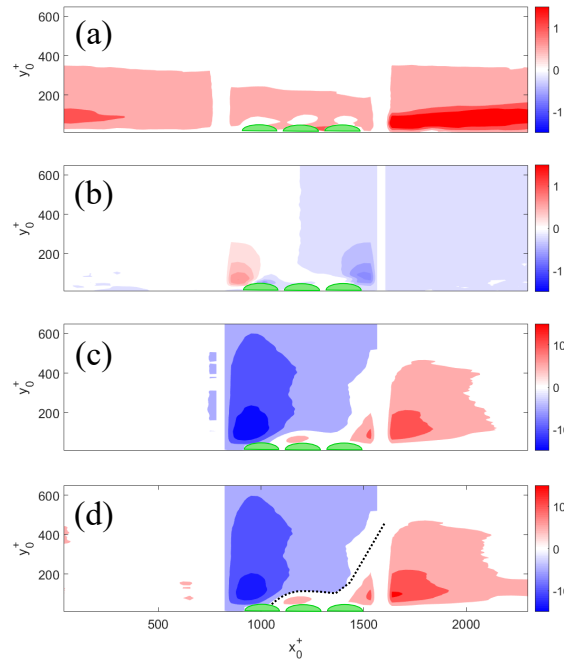
Figure 4.10: Contour plot for (a) Reynolds shear stress ($-\overline{u'v'}$) (b) time-averaged wave shear stress ($-\overline{\widetilde{U}\widetilde{V}}$) (c) mean motion shear stress ($-\overline{UV}$) and (d) the sum of all shear stresses in the presence of 50 Hz modulated air-films. The color bar scale of (c) and (d) is an order-of-magnitude larger than that of (a) and (b). Air-films are represented by green half-ovals along the bottom edge of figures.The dividing line for positive and negative total shear stress is marked by the black dotted line in (d). Note the scale difference in the contours.

(a) $-\overline{u'v'}$

(b) $-\overline{UV}$
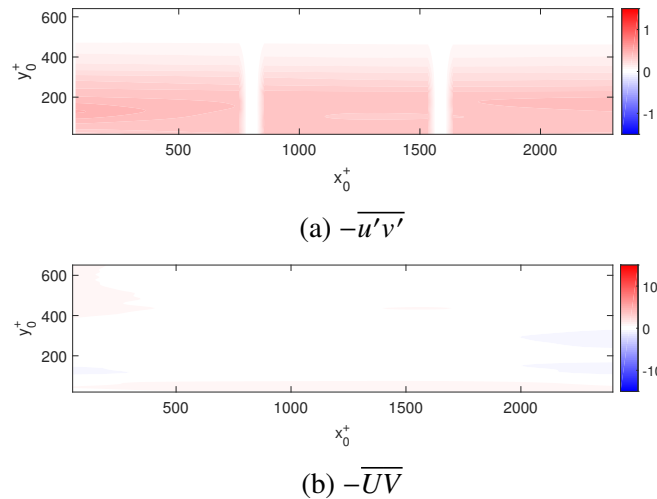
Figure 4.11: Baseline TBL (a) Reynolds shear stress ($-\overline{u'v'}$) and (b) mean motion shear stress ($-\overline{UV}$) contour. The color bar scale is set the same as that in figure 4.10. The baseline $-\overline{UV}$ is trivial when compared to the case shown in figure 4.10.

It is interesting to note that $-\overline{\widetilde{U}\widetilde{V}}$ and $-\overline{UV}$ are only present in the vicinity region of air-films. It is known that positive shear stress (mainly $-\overline{u'v'}$ in canonical TBL) transfers turbulent momentum toward the wall. With this definition, negative shear stress acts as an agent for transferring momentum away from the wall. In the region where shear stress switches sign, a layer of zero-shear-stress exists, as is manifested by the black dotted-line in figure 4.10 (d). To more clearly see the zero-shear-stress layer, the non-dimensional shear stress profiles in the air-film covered region (offset by 15 units from each other) are given in figure 4.12, with their streamwise locations shown along the top axis. To ensure data accuracy, shear stresses in regions that are close to air-films is excluded from the plot. The zero-shear-stress layer is located at where the total shear stress profile crosses the zero-value line, as is highlighted by the blue dotted line in figure 4.12. The zero-shear-stress layer starts to grow near the leading edge of air-films and reaches a plateau at approximately 100 y_0^+ away from the wall. Over the trailing air-film, the zero-shear-stress layer rapidly bends away from the wall.
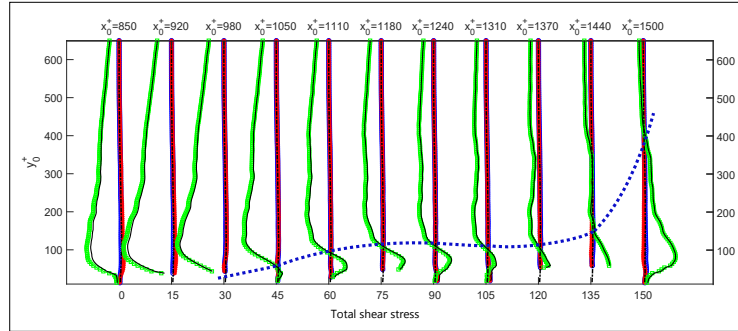
Figure 4.12: In the presence of 50 Hz modulated air-films, the total shear stress profiles show the existence of a zero-shear-stress layer (highlighted by blue dotted line). The profiles are offset by 15 units from each other with their streamwise locations shown on the top axis. Air-films are located between 900 x_0^+ and 1500 x_0^+. Symbols: blue circle, $-\overline{u'v'}$; red star, $-\overline{\widetilde{U}\widetilde{V}}$; green square, $-\overline{UV}$; black solid line, total shear stress; black dashed line, baseline TBL $-\overline{u'v'}$.

With unmodulated passive bulged and flat air-films, $-\overline{\widetilde{U}\widetilde{V}}$ does not exist. Therefore the total shear stresses for the two passive cases is $-(\overline{u'v'} + \overline{UV})$ and are shown in figure 4.13. With bulged air-films, negative and positive shear stress are found at the leading and trailing edges of air-films, respectively. Its zero-shear-stress layer is like a radial ray emitting from the central air-film. Zero-shear-stress layer is not visible with flat air-films.
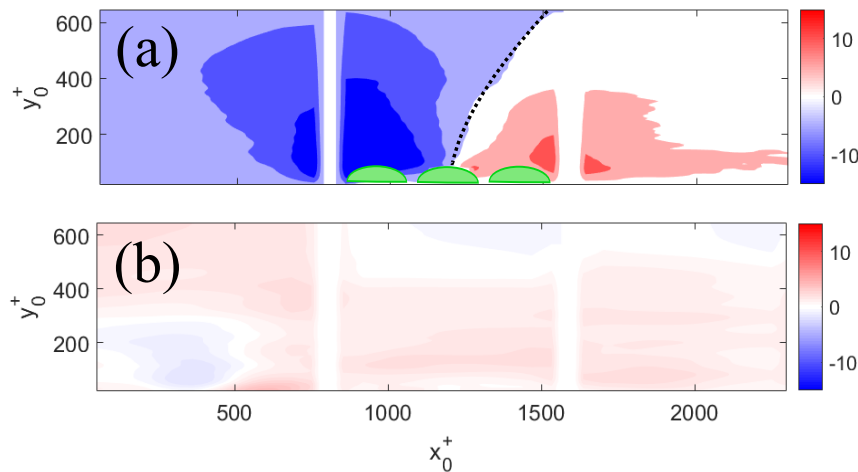
Figure 4.13: Total shear stress for unmodulated (a) bulged and (b) flat air-film. Air-films are located between 900 x_0^+ and 1500 x_0^+. Zero-shear-stress layer is observed over bulged air-films (marked by black dotted line) but not over flat air-films.

4.4 Reynolds Stress and 'Inactive' Turbulence

In the presence of 50 Hz modulated air-films, theReynolds shear stress ($-\overline{u'v'}$) and normal stresses ($\overline{u'^2}$) and ($\overline{v'^2}$) non-dimensionalized by $u_{\tau 0}^2$ are plotted with respect to log-scaled wall-distance in figure 4.14, with the profiles' streamwise locations shown on the top axis. Both the Reynolds shear and normal stresses are generally larger than the baseline case. Over the air-films (at 1050 x_0^+), both $\overline{u'^2}$ and $\overline{v'^2}$ drastically increase in the near-region of air-films. However, $-\overline{u'v'}$ is no different from the baseline case. It is even slightly suppressed at approximately 70 y_0^+. In the downstream of air-films, all quantities develop new peaks near the wall. In the farther downstream region, the new peaks are shifted away from the wall and their peak magnitudes decay, showing a relaxation process.
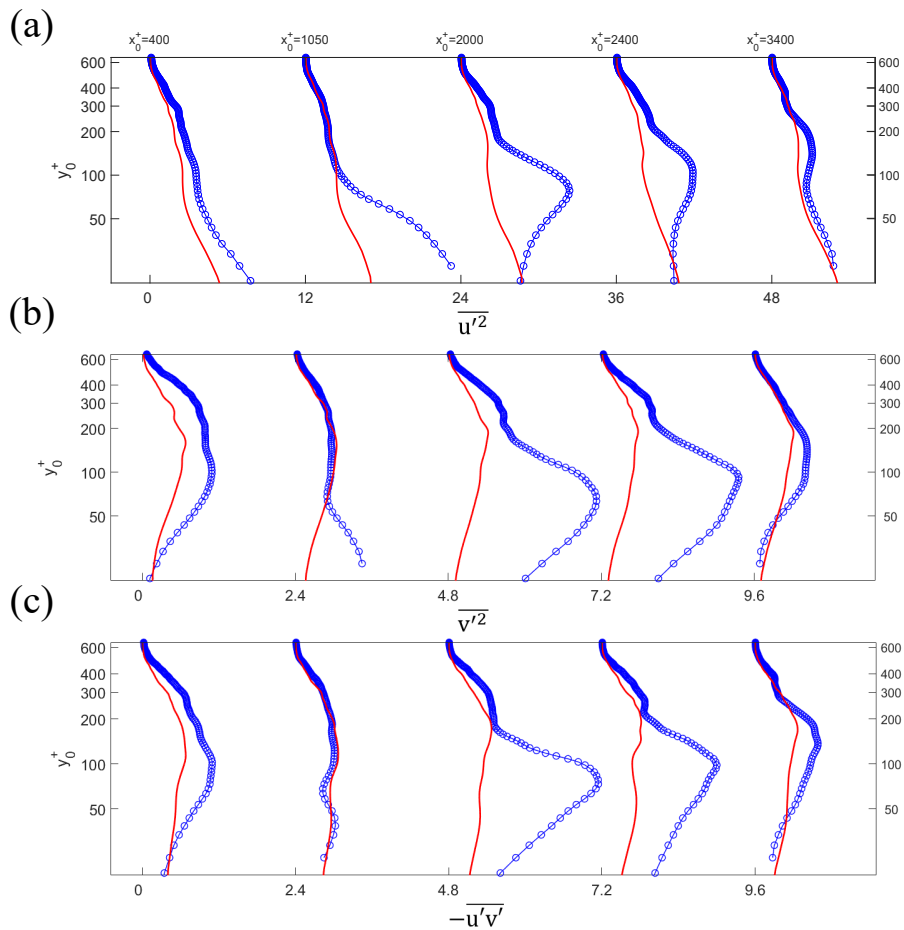
Figure 4.14: Non-dimensional Reynolds stress (a) $\overline{u'^2}$, (b) $\overline{v'^2}$ and (c) $-\overline{u'v'}$ profiles at various streamwise locations (shown on the top axis). Air-films are located between 900 x_0^+ and 1500 x_0^+. Symbols: blue circle line, air-film with 50 Hz modulation; red solid line, baseline TBL

AA Townsend (1961) proposed that the turbulent motion in the near-wall region consists of *'active'* and 'inactive' parts, among which only the *'active'* part produces Reynolds shear stress. The TBL structure parameter a_1 which is defined as the ratio of Reynolds shear stress to twice the turbulent kinetic energy ($k = \frac{1}{2}\left(\overline{u'^2} + \overline{v'^2} + \overline{w'^2}\right)$), i.e, $a_1 = \frac{-\overline{u'v'}}{2k}$, is a good measure of 'inactive' turbulent motion. The a_1 parameter can be regarded as the efficiency of turbulent eddies in producing Reynolds shear stress for a given amount of turbulent kinetic energy. Therefore, a reduced a_1 parameter indicates that the Reynolds shear stress production efficiency is low and 'inactive' turbulence is dominant at the point of observation (Bradshaw, 1967a). While the spanwise normal stress $\overline{w'^2}$ is not directly measured with 2-D DPIV, it can be roughly estimated through the relation ($\overline{w'^2} = \frac{1}{2}\left(\overline{u'^2} + \overline{v'^2}\right)$), as was suggested by Bradshaw (1967a) and Cutler and Johnston (1989).

The TBL a_1 parameter in the presence of different conditioned air-films as well as in the baseline case are plotted in figure 4.15 (a) – (d). The a_1 value for the baseline TBL is approximately 0.15, which is normally found in a zero-pressure-gradient TBL (Skaare and Krogstad, 1994). With 50 Hz modulation, the a_1 parameter reduces in the vicinity of air-films and gradually recovers to the baseline case in farther downstream region. Reduced a_1 also exists in near-region of passive bulged air-films but is not visible with passive flat air-films.
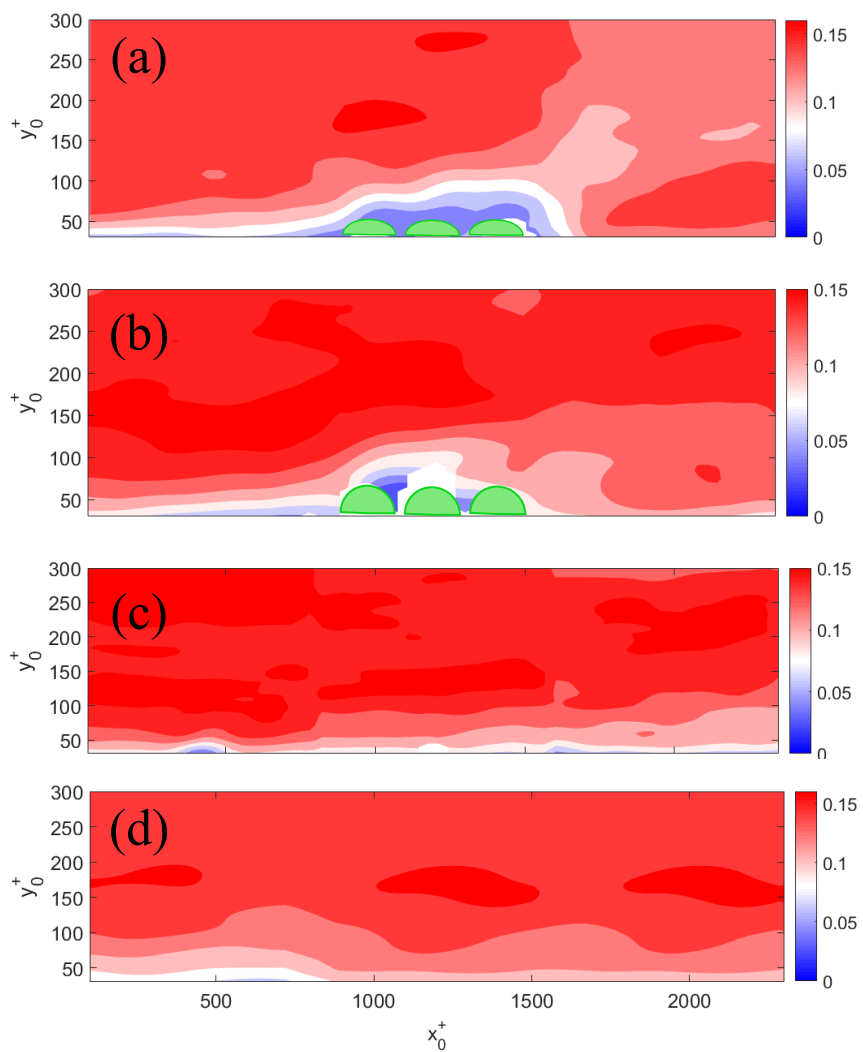
Figure 4.15: Structure parameter (a_1) contour for (a) 50 Hz modulated bulged air-film (b) bulged air-film and (c) flat air-film and (d) baseline TBL. Air-films are located between 900 x_0^+ and 1500 x_0^+. Bulged air-films are represented by green half-ovals.

4.5   Viscous Shear Stress

The TBL viscous shear stress is only significant in regions close to the wall, like in the viscous sub-layer (Tennekes, John Leask Lumley, J. Lumley, et al., 1972). Figure 4.16 (a) depicts the non-dimensional viscous shear stress ($\frac{\nu}{u_{\tau 0}^2}\frac{d\overline{U}}{dy}$) profiles at various streamwise locations in the presence of 50 Hz modulated air-films. The viscous shear stress for baseline case is also shown. When compared to the baseline case, the near-wall viscous shear stress slightly increases in the upstream of air-films but substantially reduces over and just downstream of air-films in the near-wall region. Meanwhile, the peak location of viscous shear stress is shifted away from the wall. The viscous shear stress gradually relaxes toward the baseline case in the downstream region. The detailed relaxation process in the region between 1500 x_0^+ and 2000 x_0^+ is shown in figure 4.16 (b).
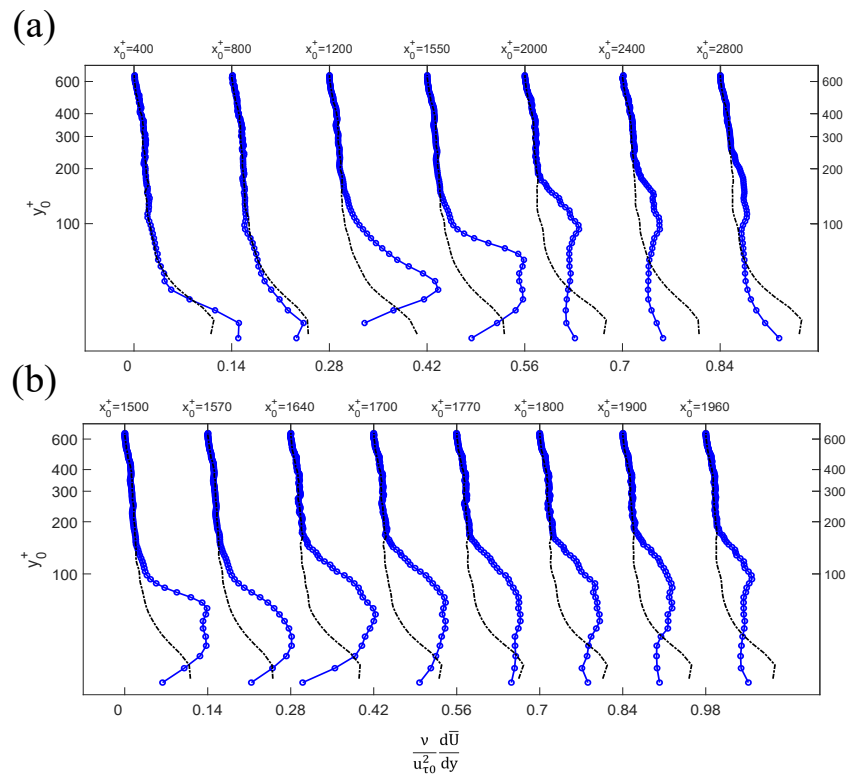
Figure 4.16: Non-dimensional viscous shear stress ($\frac{\nu}{u_{\tau 0}^2}\frac{d\overline{U}}{dy}$) at various streamwise locations (shown on the top axis). Air-films are located between 900 x_0^+ and 1500 x_0^+. Symbols: circle, 50 Hz modulated air-films; dashed line, baseline TBL

The viscous shear stress profiles in the presence of passive bulged and flat air-films are shown in figure 4.17. Similar to the modulated air-film case, with passive bulged air-film the viscous shear stresses have their peak locations shifted away from the

wall over the air-films and relaxes back in downstream of air-films. With flat air-films, the viscous shear stress is slightly suppressed in the near-wall region but shows no peak location shift.
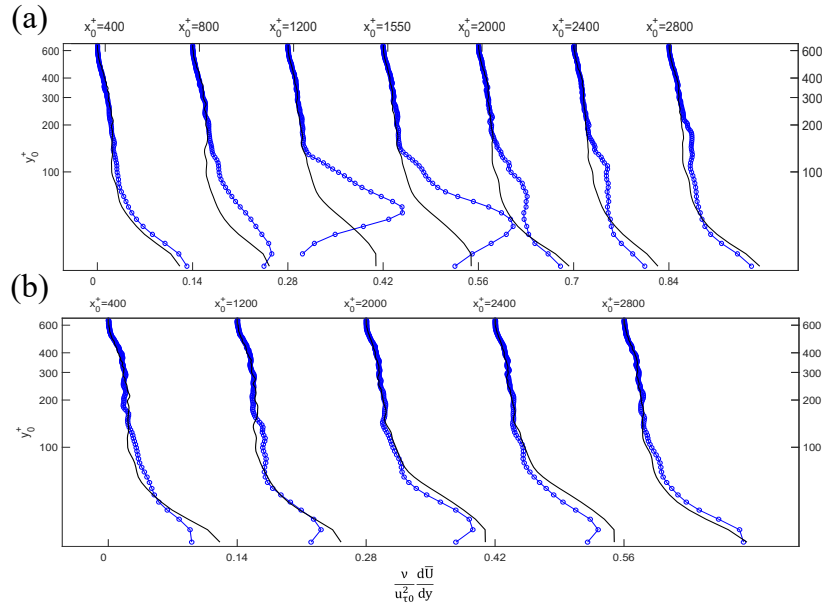
Figure 4.17: Viscous shear stress profiles for passive (a) bulged and (b) flat air-films at various streamwise locations (shown on top axis). Air-films are located between 900 x_0^+ and 1500 x_0^+. Symbols: circle, air-films; dashed line, baseline TBL

In summary, this chapter presents several modifications brought to TBL by the presence of air-films. With 50 Hz modulated bulged air-film, the streamwise velocity reduces in the near-wall region and wall-normal velocity demonstrates a blowing and suction ior. The phase-averaged streamwise velocity demonstrates a Stokes-type oscillatory motion in the near-wall region. Oscillatory motion is also found in phase-averaged wall-normal velocity. Together with Reynolds shear stress ($-\overline{u'v'}$), non-trivial $-\widetilde{\overline{UV}}$ and $-\overline{UV}$ are observed, which transfers streamwise momentum along the wall-normal direction. A layer of zero-shear-stress is found at approximately 100 y_0^+ above the 50 Hz modulated air-films. The turbulence in the near-region of oscillating air-films demonstrates strong 'inactive' motions. The viscous shear stress substantially reduces in the vicinity of air-films with its peak location shifted away from the wall. Downstream of the air-films, the reduced near-wall viscous shear stress relaxes toward the baseline TBL. The above-mentioned phenomena are generally observable at a less significant degree with passive bulged air-films. However, the phenomena are absent with passive flat air-films. The results demonstrate the significance of air-film oscillation in modifying TBL, which is enhanced by

dynamic modulation. Potential physical mechanisms for the aforementioned TBL modifications will be discussed in Chapter 5.

Chapter 5

PHYSICAL MECHANISMS AND MOMENTUM TRANSFER IN TBL

The results shown in Chapter 4 demonstrate the TBL structural changes in the presence of oscillating air-films, which may alter the TBL momentum transfer process. Therefore, understanding these changes as well as the physical mechanisms behind the changes can facilitate the understanding of wall-shear stress generation in the presence of air-films. This chapter discusses the potential mechanism for the observations presented in Chapter 4 from a modified vorticity field point of view. The TBL momentum transfer and wall-shear stress generation are discussed as well.

5.1 Phase-averaged Acceleration and Vorticity Field

To better understand the oscillatory velocity field shown in figure 4.7 and figure 4.8, the dynamic acceleration field field in the vicinity of 50 Hz modulated air-films is examined. The phase-averaged TBL acceleration field $(\frac{D(\widetilde{U})}{Dt}, \frac{D(\widetilde{U})}{Dt})$ is shown in equations 5.1, where $\langle \cdot \rangle$ denotes the phase-averaged quantity. The detailed derivation is shown in Appendix A.

$$\frac{D(\widetilde{U})}{Dt} = \frac{\partial(\widetilde{U})}{\partial t} + (\overline{U} + \widetilde{U})\frac{\partial(\overline{U} + \widetilde{U})}{\partial x} + (\overline{V} + \widetilde{V})\frac{\partial(\overline{U} + \widetilde{U})}{\partial y} + \frac{\partial \langle u'^2 \rangle}{\partial x} + \frac{\partial \langle u'v' \rangle}{dy}$$

$$\frac{D(\widetilde{V})}{Dt} = \frac{\partial(\widetilde{V})}{\partial t} + (\overline{U} + \widetilde{U})\frac{\partial(\overline{V} + \widetilde{V})}{\partial x} + (\overline{V} + \widetilde{V})\frac{\partial(\overline{V} + \widetilde{V})}{\partial y} + \frac{\partial \langle v'^2 \rangle}{\partial y} + \frac{\partial \langle u'v' \rangle}{\partial x}$$

$$(5.1)$$

Figure 5.1 (a) and (b) depict the phase snapshots of phase-averaged streamwise and wall-normal acceleration, respectively. The synchronized air-film maximum height temporal variation is also shown. In figure 5.1 (a), the streamwise acceleration at the leading and trailing edges of air-films are always of similar oscillation amplitude but opposite direction, i.e., positive acceleration at the leading edge happens together with negative acceleration at the trailing edge. In contrast, the wall-normal acceleration (shown in figure 5.1 (b)) is always in phase and only exists in the region above air-films. The wall-normal acceleration field is of similar amplitude to the streamwise acceleration field. The acceleration field shows similar trend as the oscillatory velocity field shown in figure 4.7 and figure 4.8.
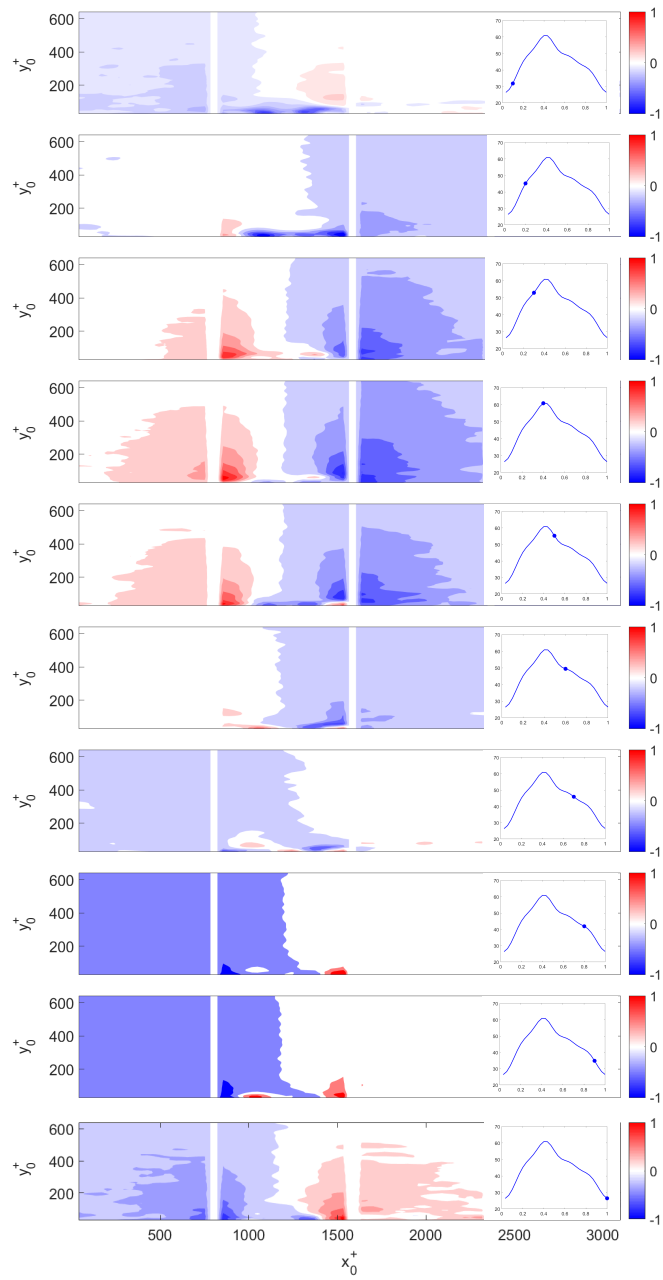
(a) $(\frac{\nu}{u_{\tau 0}^3} \frac{D(\widetilde{U})}{Dt})$

$$(b)\ \left(\frac{\nu}{u_{\tau 0}^3}\frac{D(\widetilde{V})}{Dt}\right)$$
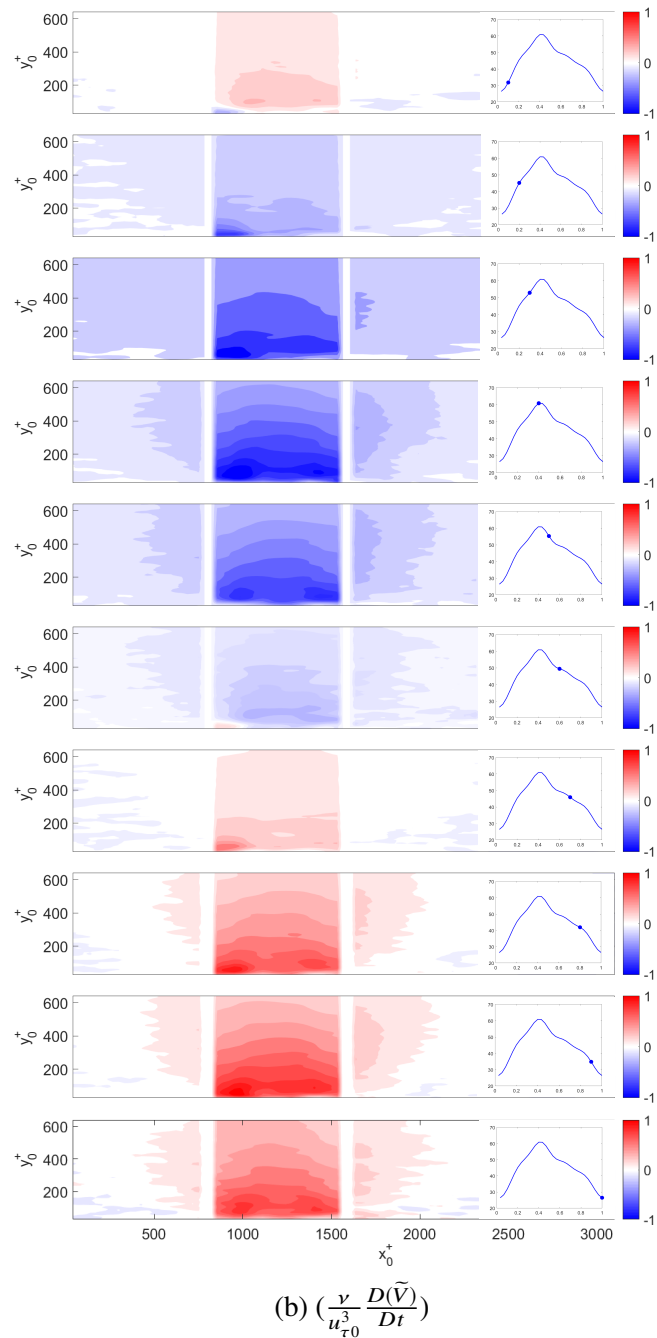
Figure 5.1: Phase-averaged acceleration (a) $\frac{D(\widetilde{U})}{Dt}$ and (b) $\frac{D(\widetilde{V})}{Dt}$ (non-dimensionalized by baseline TBL inner scale $\frac{\nu}{u_{\tau 0}^3}$) during one modulation cycle. Air-films are located between $900\ x_0^+$ and $1500\ x_0^+$.

In Chapter 3, we demonstrated that in still water patterned transverse vorticity ($\overline{\omega_z}$) is generated in the vicinity of air-films. Figure 5.2 shows the phase snapshots of oscillatory transverse vorticity ($\widetilde{\omega_z}$) in the near-wall region, where $\widetilde{\omega_z} = \frac{d\widetilde{V}}{dx} - \frac{d\widetilde{U}}{dy}$. It is found that $\widetilde{\omega_z}$ over the air-film region changes sign periodically following the air-film oscillation phases. Both positive and negative vorticity always emerges in the near-wall region and grows over time. It appears that during each cycle the existing vorticity travels outward as if is being *'pushed'* away from the wall.
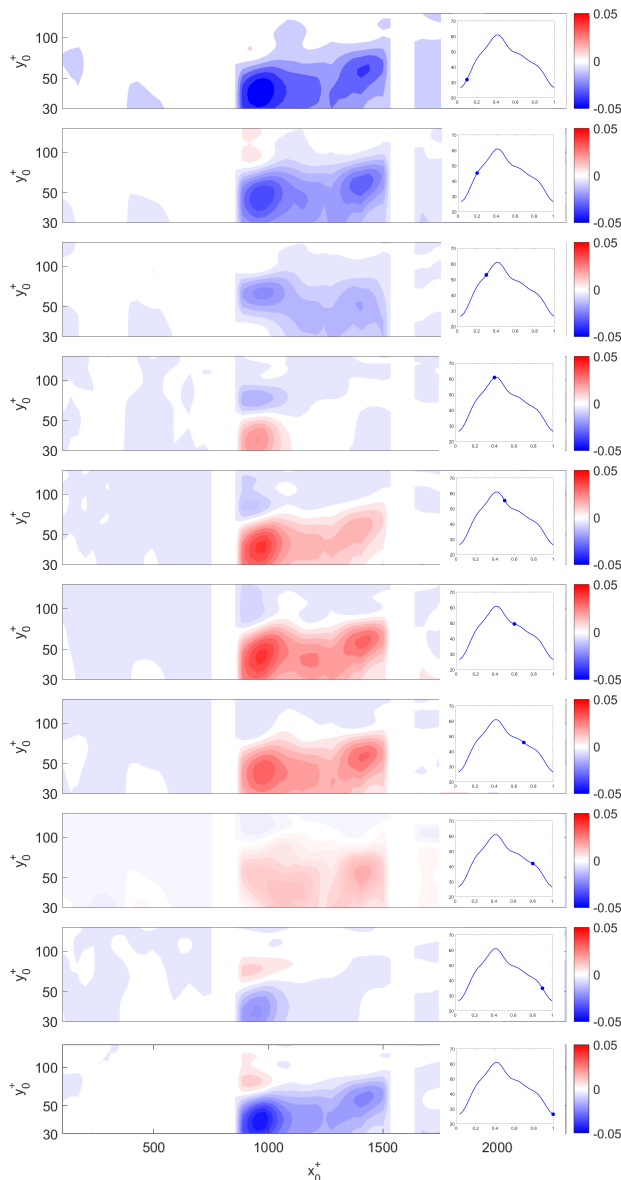
Figure 5.2: Phase snapshots of oscillatory transverse vorticity ($\frac{\nu\widetilde{\omega_z}}{u_{\tau 0}^2}$) in the presence of 50 Hz modulated air-films during one modulation cycle. Air-films are located between 900 x_0^+ and 1500 x_0^+.

The mean transverse vorticity ($\overline{\omega_z} = \frac{d\overline{V}}{dx} - \frac{d\overline{U}}{dy}$) in the vicinity of modulated air-films is greatly modified with respect to the baseline case, as shown in figure 5.3. $\overline{\omega_z}$ is elevated in the upstream of the air-films and is *'pushed'* outward from the wall over the air-films. The displaced transverse vorticity form vortex structures of high vorticity concentration over the air-films. This observation is consistent with the viscous shear stress ($\nu\frac{d\overline{U}}{dy}$) shown in figure 4.16, in which the viscous shear stress peak location is moved away from the wall over the air-film region. As the main constituting component of $\overline{\omega_z}$, the peak location of $\frac{d\overline{U}}{dy}$ also marks the location of high concentration $\overline{\omega_z}$. Downstream of air-films, the thickened vorticity layer relaxes back to the baseline case.
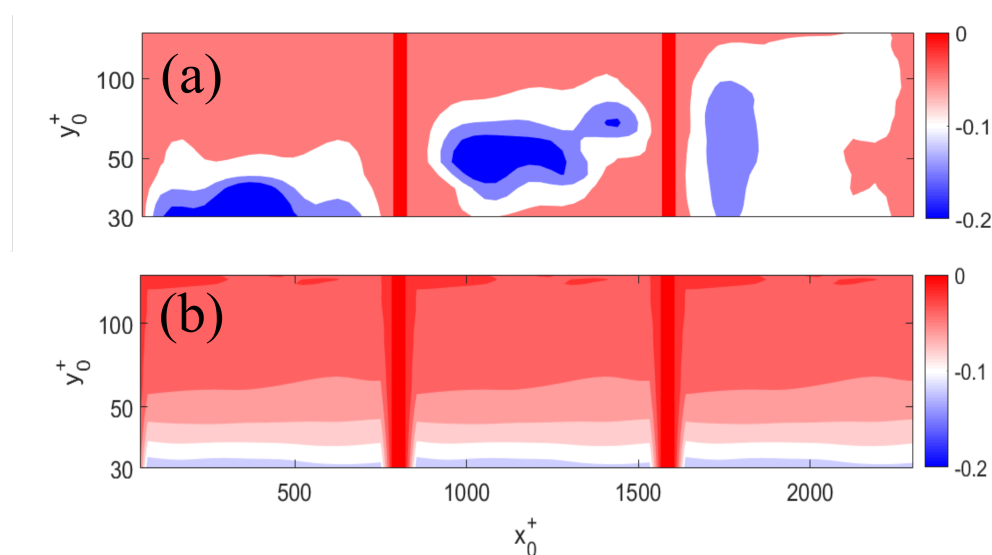
Figure 5.3: Mean transverse vorticity ($\frac{\nu\overline{\omega_z}}{u_{\tau 0}^2}$) in the presence of (a) 50 Hz modulated air-films and (b) baseline TBL. $\overline{\omega_z}$ is *'pushed away'* from the wall over the air-films and relaxes back in the downstream of air-films. Air-films are located between 900 x_0^+ and 1500 x_0^+. Note the color bar scale is from -0.2 to 0.

With unmodulated bulged air-films (shown in figure 5.4 (a)), high concentration of transverse vorticity is *'pushed away'* from the wall over the air-film region. However, with unmodulated flat air-film (shown in figure 5.4 (b)), no obvious transverse vorticity *'lift up'* is observed. These observations indicate that oscillating air-films cause the TBL high-shear region to be pushed away from the wall.
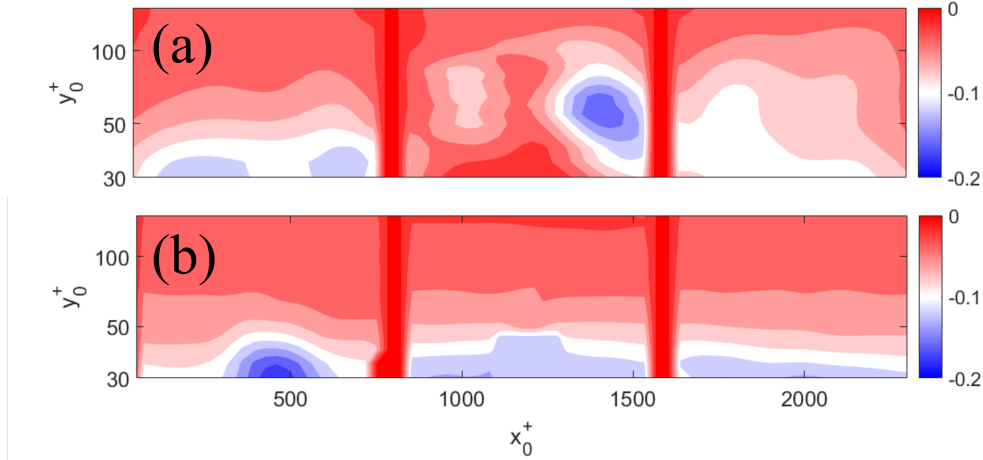
Figure 5.4: Mean transverse vorticity ($\frac{\overline{v\omega_z}}{u_{\tau 0}^2}$) in the presence of passive (a) bulged air-film and (b) flat air-film. Air-films are located between 900 x_0^+ and 1500 x_0^+. $\overline{\omega_z}$ is *'pushed away'* from the wall over bulged air-films but not over flat air-films. Note the color bar scale is from -0.2 to 0.

5.2 Discussion

In this chapter we demonstrate that unsteady acceleration and alternating signed transverse vorticity are induced in the vicinity of air-films. The above-mentioned dynamics results in the near-wall vortical structures to move away from the wall. With such understandings, in this section we discuss the potential physical mechanisms behind the observations shown in Chapter 4 and the corresponding effects on the TBL momentum transfer process.

Zero-Shear-Stress Layer, 'Inactive' Turbulence and Reduced Viscous Shear Stress

Two contributors for the zero-shear-stress layer (shown in figure 4.10) are $-\overline{\widetilde{U}\widetilde{V}}$ and $-\overline{UV}$, which can be explained with the modified near-wall vorticity field. It is known that vorticity can induce velocity field in its surrounding regions by the Biot-Savart law. Logically, any periodic appearance and disappearance of concentrated $\widetilde{\omega_z}$ field (shown in figure 5.2) can be expected to induce $\widetilde{U}\widetilde{V}$ motion. Through comparing the phase snapshots of $-\widetilde{U}\widetilde{V}$ (shown in figure 4.9) and that of $\widetilde{\omega_z}$, a strong correlation between $\widetilde{\omega_z}$ field and $-\widetilde{U}\widetilde{V}$ can be seen. Similarly, $-\overline{UV}$ can be correlated to the high-vorticity-concentration vortex structures formed by the displaced transverse vorticity ($\overline{\omega_z}$) residing over the air-films (shown in figure 5.3).

The 'inactive' turbulence can be generated by lifted $\overline{\omega_z}$ as well. AA Townsend (1961) noted that *'the inactive motion is a meandering or swirling motion made up*

from attached eddies of large size'. Indeed, the lifted transverse vorticity behaves like stationary eddies and could be the underlying mechanism for the generation of 'inactive' turbulence. From another perspective, the 'inactive' turbulence can be a result of interrupted near-wall vortical structures of TBL. Jiménez and Pinelli (1999) showed that the TBL near-wall vorticial structures are critical for the self-sustaining feature of turbulence. Having its near-wall vortical structures interrupted, the turbulence could lose its reproduction ability and act like 'inactive' turbulence. The TBL near-wall vortical structures are possibly suppressed in the process of transverse vorticity being *'pushed away'.* More results on the suppressed turbulent eddies are presented in Chapter 7.

The viscous shear stress ($\nu\frac{d\overline{U}}{dy}$) shown in figure 4.16 has its peak location shifted away from the wall and substantially reduces in the near-wall region, which is a direct reflection of *'lifted'* transverse vorticity. The peak location of viscous shear stress matches well with the peak location of transverse vorticity. In addition, in the downstream of air-films the gradually increasing near-wall viscous shear stress corresponds to the vorticity relaxation process. The increase of transverse vorticity in the near-wall region can be a result of the enhanced positive Reynolds shear stress ($-\overline{u'v'}$) and mean motion shear stress ($-\overline{UV}$) downstream of air-films (shown in figure 4.10). The enhanced shear stresses transfers large amount of TBL x-momentum toward the wall, which contributes to the increase of near-wall vorticity and viscous shear stress seen in the relaxation process.

Momentum Transfer Process

With the observations such as zero-shear-stress layer, 'inactive' turbulence and reduced viscous shear stress, the momentum transfer process in the air-film region is greatly modified. Unlike the case of canonical flat plate TBL in which Reynolds shear stress is positive and transfers momentum toward the wall, this momentum transfer process reverses in the region with negative total shear stress (shown in figure 4.10).

The zero-shear-stress layer shown in figure 4.12 acts like a barrier that separates the momentum exchange processes on its two sides. Alternatively, the zero-shear-stress layer is a zero-momentum flux layer, i.e., the x-momentum flux across the zero-shear-layer is zero. As a result, the region below zero-shear-stress layer is *'shielded'* from the flow of fast momentum above it. In addition, according to Bradshaw (1967a), the 'inactive' turbulence does not transfer momentum toward

the wall. Indeed, previous work found the wall-skin friction significantly drops when 'inactive' turbulence is strong (Stratford, 1959; Bradshaw, 1967b; Skaare and Krogstad, 1994). Further, the reduced viscous shear stress in the near-wall region also directly implies reduced wall-shear stress. These observations all point to the conclusion that momentum transfer toward the wall is suppressed and wall skin friction is expected to reduce.

Chapter 6

VORTICITY GENERATION BY OSCILLATING AIR-FILMS

In Chapter 4 and 5 we demonstrated that time-varying transverse vorticity is generated by oscillating air-films, which modifies the TBL near-wall vortical structures. The magnitude of vorticity generated by oscillating air-films can be controlled by controlling the air-film static concavity configurations plus the amplitude of its oscillations. In this chapter, we demonstrate a case in which strong vorticity is generated by keeping the air-film's initial configuration flat (or its initial protrusion height small) while maintaining all other conditions exactly the same as those in Chapter 4 and 5. For example, 8 mm sized air-films were sustained in TBL with Re_θ equal to 1200 and modulated by a 50 Hz signal (with fixed output power). The air-film maximum height (h) was oscillating within 0.85 - 2.4 mm (equivalent to $22 - 48$ y_0^+), which is of a similar oscillation amplitude but smaller mean protrusion height when compared with the case shown in Chapter 4.

The strong vorticity generation is reflected by the enhanced Stokes-type oscillatory motion ($\widetilde{U}$) and phase-averaged transverse vorticity ($\widetilde{\omega_z}$) when compared with that presented in Chapter 4 and 5. The velocity profiles for $\overline{U} + \widetilde{U}$ and $\widetilde{U}$ at the leading edge of air-films are shown in figure 6.1 (a) and (b), respectively. The maximum value of $\widetilde{U}$ is 4 $u_{\tau 0}$, which is two times larger than that shown in figure 4.6. The phase-averaged transverse vorticity ($\widetilde{\omega_z}$) together with the air-film maximum height (h) for each phase is shown in figure 6.2. When compared with the case shown in figure 5.2, the magnitude of $\widetilde{\omega_z}$ here is four times larger. Corresponding to the strong time-varying $\widetilde{\omega_z}$, the center of mean transverse vorticity ($\overline{\omega_z}$) shown in figure 6.3 resides farther away from the wall when compared with that in figure 5.3. In the current case, the maximum value of $\widetilde{\omega_z}$ is comparable with that of $\overline{\omega_z}$.

Figure 6.4 shows the profiles of transverse vorticity ($\overline{\omega_z}$) and Reynolds shear stress ($-\overline{u'v'}$) in the vicinity region of air-films. Figure 6.4 (a) shows that the peak of transverse vorticity is shifted away from the wall, which implies the maximum viscous shear stress does not reside on the wall anymore. In figure 6.4 (b), the maximum of $-\overline{u'v'}$ is elevated at approximately 90 y_0^+, which may be related to the outward shift of $\overline{\omega_z}$. Another interesting observation is that the distribution of Reynolds shear stress shows suppression in region below 50 y_0^+ when compared
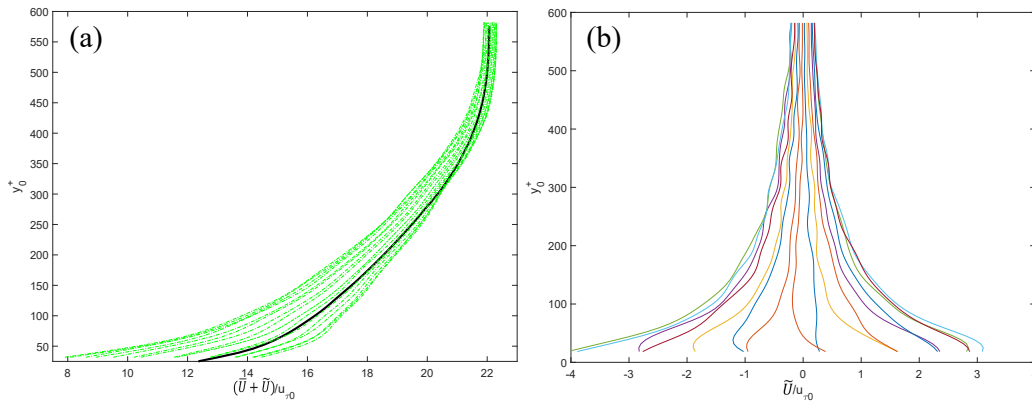
Figure 6.1: Phase-averaged velocity (a) $\overline{U} + \widetilde{U}$ and (b) $\widetilde{U}$ showing a stronger oscillatory motion than that shown in figure 4.5 and 4.6. Symbols for figure 6.1 (a): green dashed line: $\overline{U} + \widetilde{U}$ at various phases, black solid line: Baseline TBL $\overline{U}$
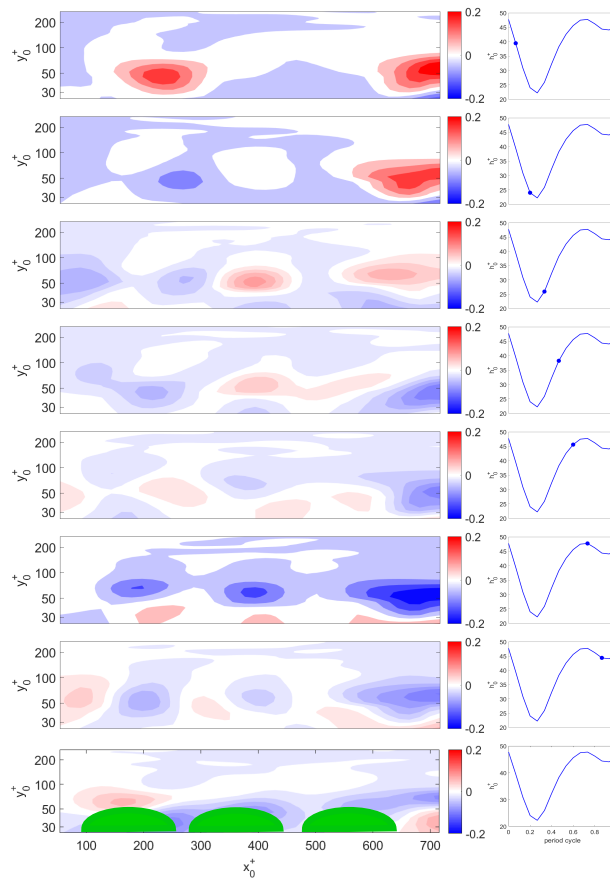
Figure 6.2: (a) Phase snapshots $\widetilde{\omega_z}$ demonstrates larger oscillation amplitude than that in figure 5.2. The air-films are located between 90 x_0^+ and 640 x_0^+ with a maximum height of 48 y_0^+, as highlighted by the green half-ovals along the bottom edge of figure.
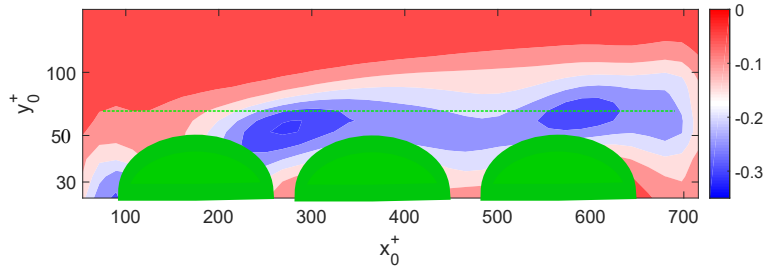
Figure 6.3: Mean transverse vorticity ($\overline{\omega_z}$) in the vicinity of air-films demonstrates a similar magnitude as $\widetilde{\omega_z}$ shown in figure 6.2. The green dotted line is at wall distance of 65 y_0^+ (well above the maximum air-film height) is useful for the content of figure 6.6

with the baseline case. The Reynolds shear stress seems to follow the behavior trend of mean transverse vorticity.
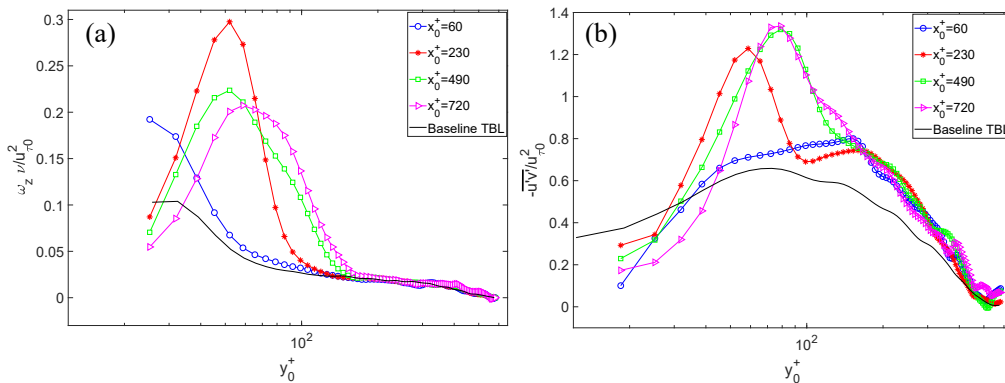
Figure 6.4: (a) Mean transverse vorticity ($\overline{\omega_z}$) and (b) Reynolds shear stress ($-\overline{u'v'}$) profiles in the vicinity of air-films. The air-films are located between 90 x_0^+ and 640 x_0^+.

As was discussed in Chapter 4, TBL in the vicinity of oscillating air-film is dominated by 'inactive' turbulence. 'Inactive' turbulent motion can be reflected by suppressed structure parameter a_1 which is defined as the ratio of Reynolds shear stress over twice the turbulent kinetic energy ($a_1 = \frac{-\overline{u'v'}}{2k}$, where k is turbulent kinetic energy). Figure 6.5 compares the structure parameter a_1 in the presence of modulated air-films with the baseline case, which is greatly reduced in the vicinity of air-film and also in TBL outer layer. The reduced a_1 parameter confirms the dominance of 'inactive' turbulent motions near the wall. Bradshaw (1967a) noted that 'inactive' turbulence *'does not produce Reynolds shear stress'*. The dominance of 'inactive' turbulence is in line with the reduced near-wall Reynolds shear stress shown in figure 6.4 (b).
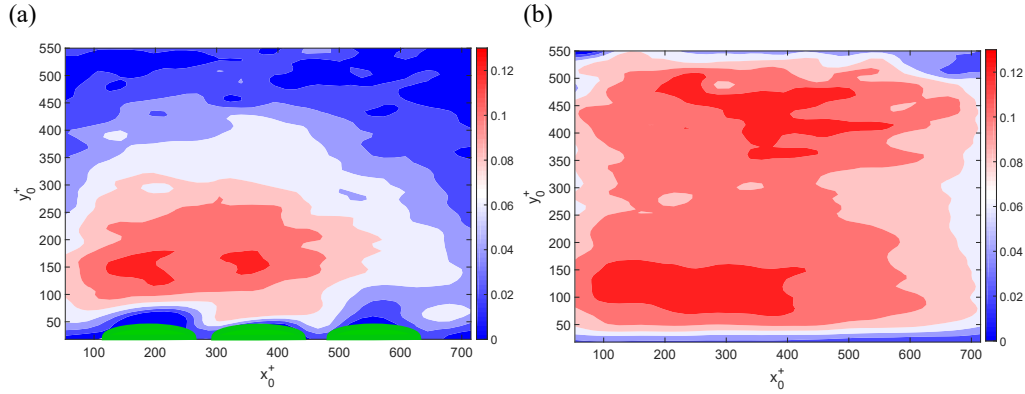
Figure 6.5: Contour plot of TBL structure parameter (a_1) over (a) 50 Hz modulated air-film and (b) flat plate. The air-films are highlighted by the green half-ovals along the bottom edge of figure (a).

Strong velocity gradients, such as $\frac{d\overline{U}}{dx}$, is observed in the vicinity region of air-films, which could be induced by the modified vorticity field. Figure 6.6 plots the local acceleration factor K_l ($K_l = \frac{d\overline{U}}{dx}\frac{\nu}{U^2}$) at 3 mm (equivalent to 65 y_0^+) away from the wall, i.e., along the green dotted line shown in figure 6.3. The leading and trailing edges of air-films are marked by the hexagon and pentagon respectively. K_l is positive over most of the air-film region. Near the trailing edge of air-films, K_l has a positive peak followed by a negative trough in the downstream of air-films. In the presence of oscillating air-films, the magnitude of K_l at 65 y_0^+ is approximately $O(10^3)$ larger than that of the baseline case. The TBL shape factor (H^*) defined as the ratio of boundary layer displacement thickness (δ^*) over its momentum thickness (θ), i.e., ($H^* = \frac{\delta^*}{\theta}$), is also plotted in figure 6.6. H^* increases starting from the leading edge of air-films and decreases after the trailing edge of air-films.

The shape factor of a boundary layer (H^*) has a typical value of 2.59 for laminar boundary layer and 1.3-1.4 for TBL. In addition, it is known that with positive $\frac{d\overline{U}}{dx}$ the TBL can go through a reverse-transition, or re-laminarization process (Launder, 1964; Narayanan and Ramjee, 1969; Warnack and Fernholz, 1998; Bourassa and Thomas, 2009; Schraub and Stephen Jay Kline, 1965; Stephen J Kline et al., 1967). Reviews on this topic can be found in Narasimha and Sreenivasan (1979) and Sreenivasan (1982). Stephen J Kline et al. (1967) found a criterion for TBL reverse-transition onset, which requires that the free stream acceleration factor ($K = \frac{dU_\infty}{dx}\frac{\nu}{U_\infty^2}$) larger than $+3.7 \times 10^{-6}$. Interestingly, the positive K_l over air-film region is significantly larger (approximately $O(10^4)$) than the re-laminarization onset criterion proposed by Stephen J Kline et al. (1967), although the two acceleration factors
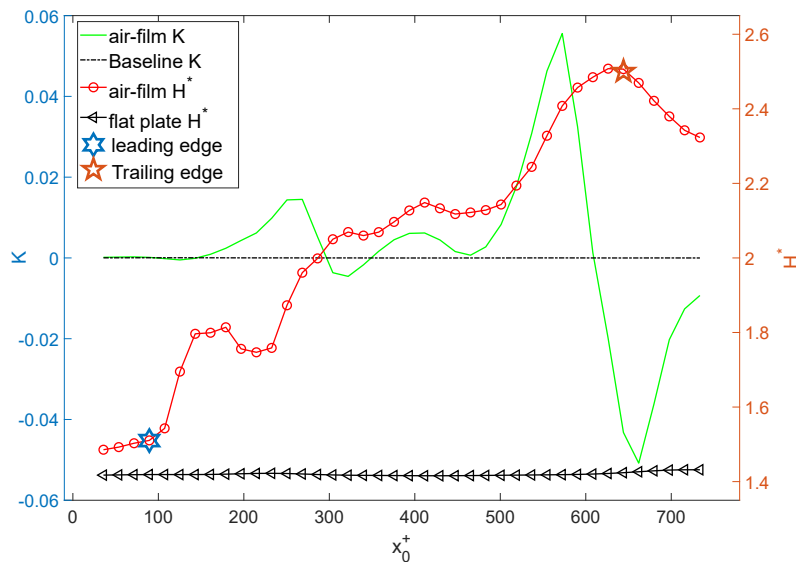
Figure 6.6: Near-wall acceleration factor (K_l) at 65 y_0^+ (along the green dotted line in figure 6.3) and TBL shape factor (H^*) over the air-film region. The air-films are located between 90 x_0^+ and 640 x_0^+. Symbols are shown in the plot.

are not at the same wall-normal location and cannot be directly compared. The positive acceleration factor (K_l) and elevated shape factor (H^*) seems pointing to a re-laminarization process. The take-home message here is that positive velocity gradient ($\frac{d\overline{U}}{dx}$) exists in the near-region of air-films, which is critical for understanding the re-laminarization mechanism to be prsented in Chapter 7. A rigorous analysis based on the energy exchange process will be given.

C h a p t e r   7

A RE-LAMINARIZATION MECHANISM IN THE NEAR-REGION OF AIR-FILMS

In the case demonstrated in Chapter 6, a re-laminarization process seems to exist. In this chapter, the detailed re-laminarization process of the same case is presented by analyzing the kinetic energy exchange in TBL.

It is known that turbulent kinetic energy in canonical flat plate TBL is supplied through the turbulent kinetic energy production (TKP) term, which extracts energy from the mean flow motion and transfers it to the turbulent motions. In the turbulent kinetic energy equation (given in Appendix B), TKP is expressed as the product of Reynolds stresses and mean velocity gradients, i.e., in tensorial form, TKP = $-\overline{u_i' u_j'} \frac{\partial \overline{U_i}}{\partial x_j}$, where i and j can represent any direction in the three-dimensional space. The sign of TKP is usually positive which demonstrates that energy is transferred from mean flow motion to turbulent motions. In contrast, negative TKP means energy is transferred from the turbulent motion toward mean motion. Analysis and discussion of negative TKP can be found in (Hinze, 1975).

In the presence of periodic perturbations, the TBL energy exchange process is more complicated. In such scenarios, the TBL total kinetic energy in tensorial form is expressed as $K_{total} = \frac{1}{2}(\overline{U_i}\,\overline{U_i} + \widetilde{U_i}\,\widetilde{U_i} + \overline{u_i' u_i'})$, with each energy term corresponding to the mean motion, oscillatory motion and turbulent motion respectively. Energy exchange can happen between any two of the three flow quantities through the generalized kinetic energy production terms (details given in Appendix B). To distinguish the three energy exchange routes, the generalized kinetic energy production terms will be referred as KP_{MT}, KP_{MO} and KP_{OT}, where 'M' represents mean motion, 'O' represents oscillatory motion and 'T' represents turbulent motion. With this definition, 'KP_{MT}' here is identical to TKP when periodic perturbations are absent. The tensorial notations of generalized kinetic energy production terms are given in figure 7.1, where $\langle \cdot \rangle$ denotes phase-averaged quantity. The derivation of generalized kinetic energy production terms can be found in W. Reynolds and A. Hussain (1972). The energy transfer directions are determined by the signs of kinetic energy production terms. In figure 7.1, the arrow directions mark the energy transfer directions with positive kinetic energy production terms. If the kinetic energy production

terms are negative, energy is transferred in the opposite arrow directions. In the same function role of TKP in canonical TBL, the three generalized kinetic energy production terms are only responsible for redistributing energy within TBL and do not generate or dissipate energy.
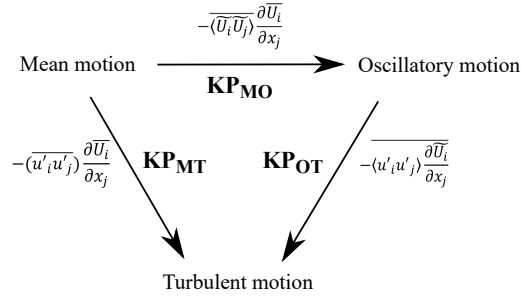
Figure 7.1: Energy exchange routes between the mean, oscillatory and turbulent motion are labeled as KP_{MT}, KP_{MO} and KP_{OT}. The arrow direction marks the energy transfer direction.

7.1 Negative Turbulent Kinetic Energy Production (KP_{MT}) in the Near-Wall Region

The energy exchange rate between mean motion and turbulent motion (KP_{MT}) is first analyzed. KP_{MT} has a tensorial form of $-\overline{u'_i u'_j}\frac{\partial \overline{U_i}}{\partial x_j}$. Because all the air-films were modulated in phase and the air-film array transverse span is large, the mean flow field can be assumed transversely homogeneous. Therefore, the KP_{MT} components only involve Reynolds stresses and velocity gradients in the x-y plane, which are listed as follows below:

$$-\overline{u'v'}\frac{d\overline{U}}{dy}, -\overline{u'v'}\frac{d\overline{V}}{dx}, -\overline{u'^2}\frac{d\overline{U}}{dx}, -\overline{v'^2}\frac{d\overline{V}}{dy} \tag{7.1}$$

In canonical zero-pressure-gradient TBL, only the first component is non-trivial and always positive. However, in the presence of velocity gradient such as positive $\frac{d\overline{U}}{dx}$ (shown in figure 6.6), the third component $-\overline{u'^2}\frac{d\overline{U}}{dx}$ is negative, which could result in negative KP_{MT}.

The KP_{MT} calculated from DPIV measurements confirms the existence of negative KP_{MT}. Figure 7.2 (a) and (b) plot the KP_{MT} profiles (non-dimensionalized by $u_{\tau 0}^4/\nu$) at the leading edge (at 70 x_0^+) and trailing edge (at 680 x_0^+) of air-films, respectively. As was shown in figure 6.6, positive and negative $\frac{d\overline{U}}{dx}$ exist at these two locations respectively. The baseline TKP profile is also shown. Negative KP_{MT} is observed

in the near-wall region at the leading edge of air-films (shown in figure 7.2 (a)). Closely inspecting all four KP_{MT} components, $-\overline{u'^2}\frac{d\overline{U}}{dx}$ is found negatively large in the near-wall region, which is the major reason for the generation of negative KP_{MT} in the near-wall region. On the other hand, KP_{MT} at the trailing edge of air-film (shown in figure 7.2 (b)) is non-negative near the wall. The $-\overline{u'^2}\frac{d\overline{U}}{dx}$ term is positive near the wall. However, negative $-\overline{u'^2}\frac{d\overline{U}}{dx}$ still exists in regions farther away from the wall ($\sim 100 y_0^+$) and results in negative KP_{MT} there.

Besides the $-\overline{u'^2}\frac{d\overline{U}}{dx}$ term, the $-\overline{u'v'}\frac{d\overline{U}}{dy}$ term which is normally found in zero-pressure-gradient TBL still matters. When compared to the baseline case, $-\overline{u'v'}\frac{d\overline{U}}{dy}$ increases near the air-film leading edge (shown in figure 7.2 (a)). At the trailing edge (shown in figure 7.2 (b)), it reduces near the wall but increases in region further away from the wall. $-\overline{u'v'}\frac{d\overline{V}}{dx}$ and $-\overline{v'^2}\frac{d\overline{V}}{dy}$ are of smaller magnitude than the other two terms. It is noted that the baseline case TKP peak location is slightly off from its normally expected position at approximately 15 y_0^+ (Pope, 2001). The discrepancy could be a result of inaccurate scaling factor (y_0^+) used. The scaling factor was calculated based on the friction velocity ($u_{\tau 0}$) estimated using the Charted Clauser method (Clauser, 1954), which is not highly accurate.
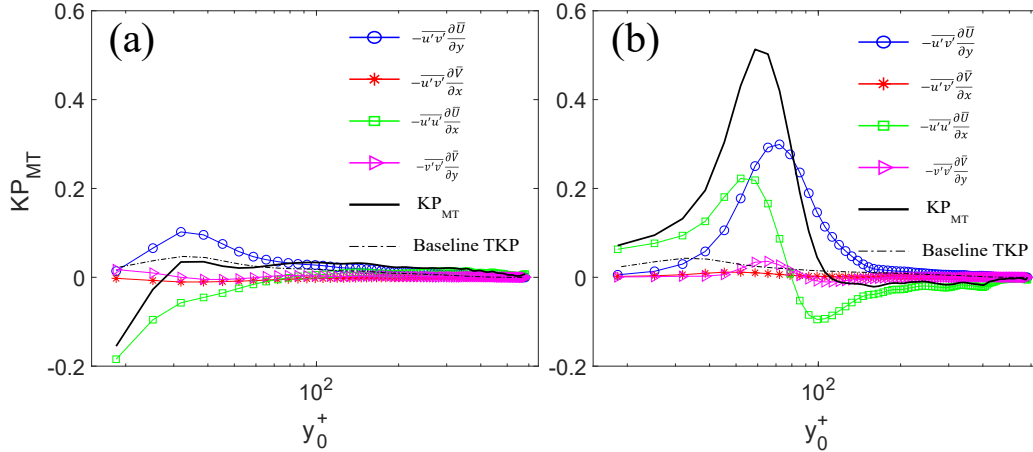
Figure 7.2: Components of KP_{MT} at (a) leading edge (70 x_0^+) and (b) trailing edge (680 x_0^+) of air-films. All quantities are non-dimensionalized by the baseline TBL inner scale ($u_{\tau 0}^4/\nu$)

To have an idea about the mean KP_{MT} in the air-film region, the wall-normal average of KP_{MT} in the near-wall region (between 31 y_0^+ and 65 y_0^+) and across the full TBL thickness (between 31 y_0^+ and 550 y_0^+) are plotted in figure 7.3 (a) and (b) respectively. The streamwise average value of wall-normal mean KP_{MT} is also plotted in figure 7.3, the sign of which reflects the net energy transfer direction. To

ensure the result accuracy, regions that are close to the air-films are excluded from the calculation. In figure 7.3 (a), the near-wall mean KP_{MT} is negative or positive depending on streamwise locations. However, its streamwise average is negative with a magnitude three times that of the baseline TKP case. This observation indicates that in the near-wall region a significant amount of turbulent energy is transferred toward the mean flow motion. The wall-normal average of KP_{MT} across the full TBL thickness (shown in figure 7.3 (b)) has a similar shape as the near-wall mean KP_{MT} but with a much-reduced magnitude. This is because most of energy exchange between mean motion and turbulent motion happens in the near-wall region (Tennekes, John Leask Lumley, J. Lumley, et al., 1972). In this case, the streamwise average of wall-normal mean KP_{MT} is positive, with a magnitude approximately half of the baseline TKP magnitude. This indicates the net energy supply for turbulence in the whole TBL reduces in the presence of oscillating air-films.
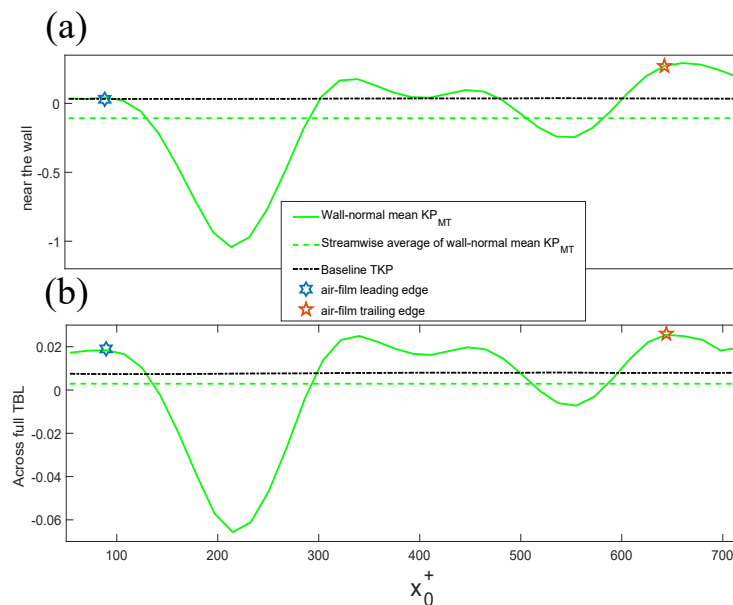
Figure 7.3: Wall-normal mean KP_{MT} in (a) near-wall region (between 31 y_0^+ and 65 y_0^+) and (b) across the full TBL thickness (between 31 y_0^+ and 550 y_0^+). Symbols are shown in figure.

In the previous studies on TBL re-laminarization under the effect of favorable pressure gradient, negative TKP was not observed although $-\overline{u'^2}\frac{d\overline{U}}{dx}$ was also found (Bourassa and Thomas, 2009; Warnack and Fernholz, 1998). The reason is because other TKP components balanced the total TKP to be a reduced but still positive value. The re-laminarization process still happened in those cases because the turbulent energy gradually dissipates. As was reported by Warnack and Fernholz

(1998), TKP *'does not show a switch off of turbulent energy production'*. In the presence of oscillating air-films, however, negative KP_{MT} is generated by a much stronger velocity gradient which only exists in the vicinity of air-films. With negative KP_{MT}, energy is no longer supplied to turbulence by mean flow motion. Instead, energy is continuously transferred away from turbulence to mean flow motion.

7.2 Complete Energy Exchange in TBL

KP_{MT} is only part of the complete energy exchange process that happens in TBL under forced perturbation. Energy exchange also happens through the other two energy transfer routes (KP_{MO} and KP_{OT}). Therefore, the negative KP_{MT} should be analyzed in the frame of complete energy exchange between all flow quantities. Taken from figure 7.1, the definition of KP_{MO} and KP_{OT} are shown in equation 7.2:

$$KP_{MO} = -\widetilde{U}_i\widetilde{U}_j\frac{\partial\overline{U}_i}{\partial x_j}, KP_{OT} = -\overline{\left\langle u'_i u'_j\right\rangle}\frac{\partial\widetilde{U}_i}{\partial x_j} \tag{7.2}$$

The contour plots of mean kinetic energy production terms in the near-wall region are shown in figure 7.4 (a) –(c), with air-films represented by green half-ovals. KP_{MT} shown in figure 7.4 (a) is mainly negative in the vicinity region of air-films, such as at 230 x_0^+. KP_{MO} shown in figure 7.4 (b) depicts the non-trivial energy transfer between mean motion and oscillatory motion in both directions. Energy is transferred from mean motion to the oscillatory motion at the leading/trailing edges of air-films but in the opposite direction over the air-films. KP_{OT} shown in figure 7.4 (c) is relatively small compared with the other two kinetic energy production terms.
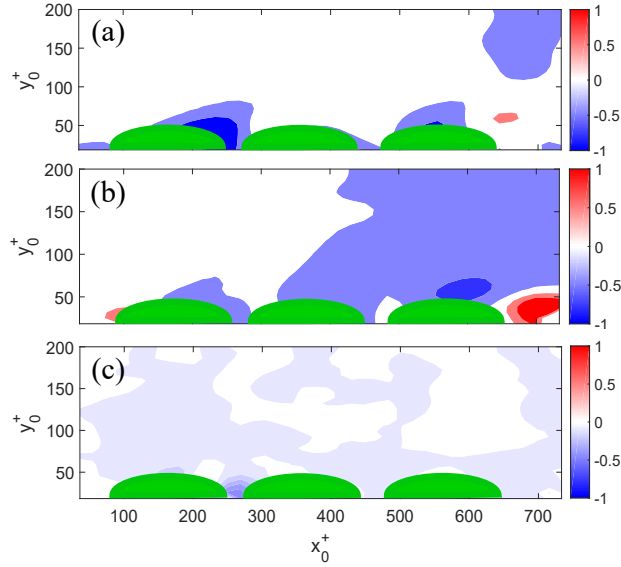
Figure 7.4: Contour for the generalized kinetic energy production terms (a) KP_{MT} (b) KP_{MO} and (c) KP_{OT} in the near-wall region. Air-films are located between 90 x_0^+ and 640 x_0^+

The profiles of kinetic energy production terms are compared at the leading (shown in figure 7.5 (a)-(c)) and trailing edges (shown in figure 7.5 (d)-(e)) of air-films. The baseline TKP is also shown. The key components for KP_{MO} (shown in figure 7.5 (b) and (e)) are found to be $-\widetilde{U}\widetilde{V}\frac{\partial \overline{U}}{\partial y}$ and $-\widetilde{U}\widetilde{U}\frac{\partial \overline{U}}{\partial x}$, which are of the same signs as those of KP_{MT} ($-\overline{u'^2}\frac{d\overline{U}}{dx}$ and $-\overline{u'v'}\frac{d\overline{U}}{dy}$) at both leading and trailing edges of air-films. This is probably because both kinetic energy production terms depend on the same velocity gradients. KP_{OT} (shown in figure 7.5 (c) and (f)) is much smaller than the baseline TKP.
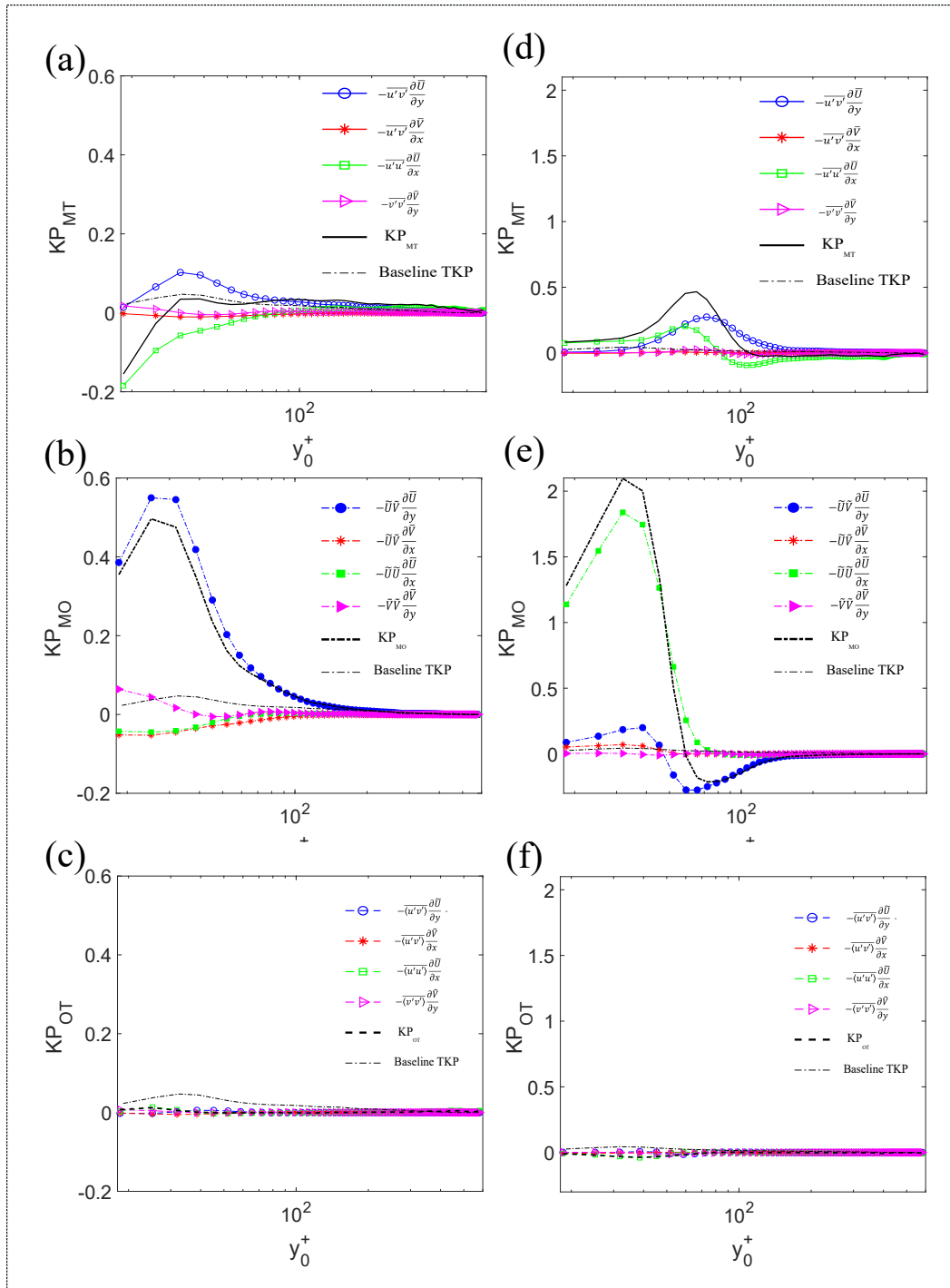
Figure 7.5: Energy exchange routes KP_{MT} ((a) and (d)), KP_{MO} ((b) and (e)) and KP_{OT}((c) and (f)), at the leading edge ((a) -(c)) and trailing edge ((d) - (f)) of air-films. The symbol notations are shown in the plots.

Repeating the analysis shown in figure 7.3, the wall-normal mean of three kinetic energy production terms in the near-wall region (between 31 y_0^+ and 65 y_0^+) and across the full TBL thickness (between 31 y_0^+ and 550 y_0^+) are plotted in figure 7.6 (a) and (b) respectively. The relative significance of three kinetic energy production terms at all streamwise locations can be seen. Table 7.1 lists the streamwise average of the wall-normal mean kinetic energy production terms in the near-wall region and across the full TBL thickness. In the near-wall region, energy is transferred from turbulence to both the mean motion and oscillatory motion. At the same time, energy is transferred from mean motion to oscillatory motion. Based on the information shown in Table 7.1, the near-wall energy transfer is schematically shown figure 7.7. Because turbulent energy is transferred to both mean motion and oscillatory motion in the near-wall region, the turbulence there is confirmed to loss energy, which points to a re-laminarization process.
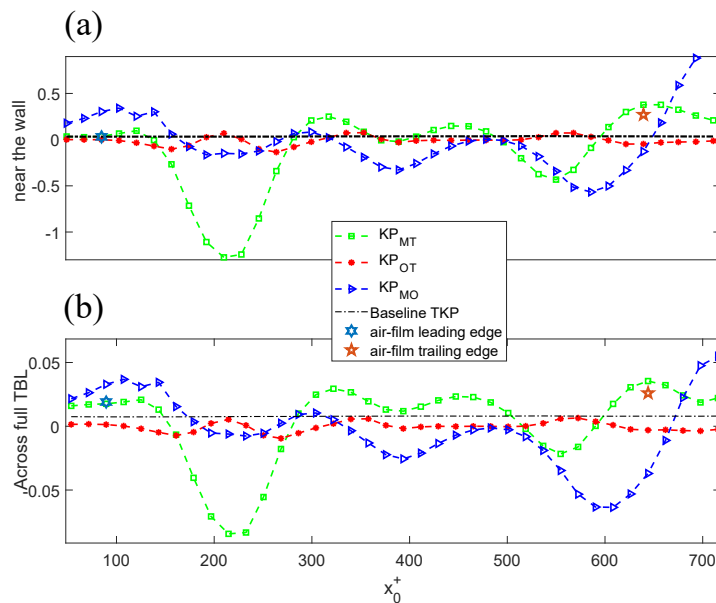
Figure 7.6: Wall-normal mean kinetic energy production terms in (a) near-wall region (between 31 y_0^+ and 65 y_0^+) and (b) across full TBL thickness (between 31 y_0^+ and 550 y_0^+). Symbols are shown in the plot.

energy exchange	KP_{MT}	KP_{MO}	KP_{OT}	Baseline TKP
In near-wall region	-0.089	0.009	-0.011	0.035
Across full TBL thickness	0.004	-0.0025	-0.0004	0.008

Table 7.1: Wall-normal mean energy transfer rate in the near-wall region (between 31 y_0^+ and 65 y_0^+) and across full TBL thickness (between 31 y_0^+ and 550 y_0^+) between the mean motion, oscillatory motion and turbulent motion.
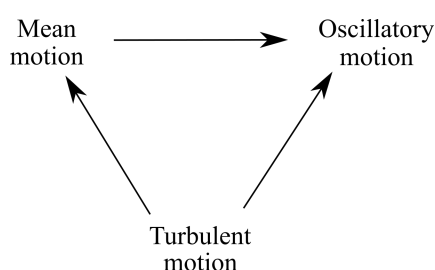
Figure 7.7: The TBL near-wall energy transfer in the presence of 50 Hz modulated air-films. The turbulent kinetic energy is transferred toward both mean motion and oscillatory motion.

7.3 Suppression of TBL Large Eddies and Production of 'Inactive' Turbulence

With the turbulent kinetic energy transferred toward both the mean motion and oscillatory motion in the near-wall region, the near-wall turbulent kinetic energy is expected to reduce. Figure 7.8 (a) shows the profile of streamwise turbulent intensity ($\overline{u'^2}$) at 230 x_0^+, where strong negative turbulent kinetic energy production is observed. Counter-intuitively, the streamwise turbulent intensity increases rather than decreases, when compared with the baseline TBL. What is more, the elevated turbulent intensity mainly happens in the near-wall region where turbulence losses large amount of energy.

To understand these counter-intuitive observations, the turbulent fluctuation spectra of $\overline{u'^2}$ shown in figure 7.8 at 20 y_0^+ and 70 y_0^+ are plotted in figure 7.8 (b) and (c) respectively. At 20 y_0^+, the low-frequency fluctuations significantly reduce when compared with the baseline case. The magnitudes of low-frequency fluctuations are only approximately 1/3 of the baseline case. Meanwhile, fluctuations at several high frequencies, such as 50Hz, 100Hz and 150 Hz, are significantly enhanced. It

is interesting to note that these frequencies are equal to the modulation frequency and its higher-order harmonics. In region farther away from the wall, i.e. at 70 y_0^+, turbulent fluctuations (shown in figure 7.8 (c)) are enhanced at both low and high frequencies.
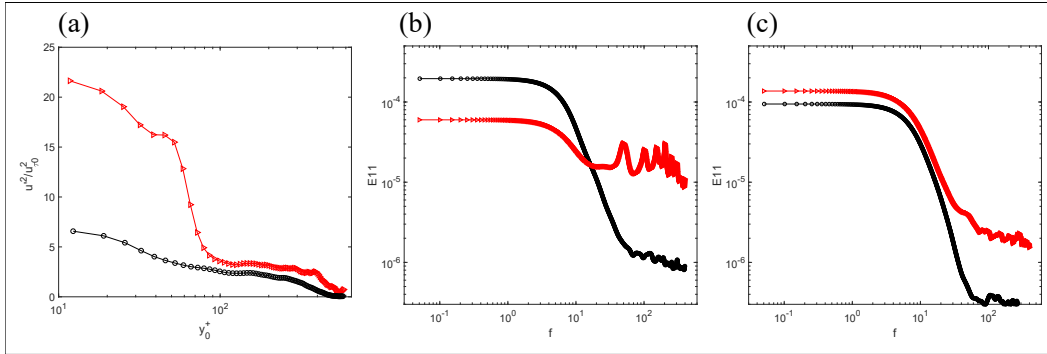
Figure 7.8: (a) Streamwise turbulent intensity ($\overline{u'^2}$) profile at 230 x_0^+ and its fluctuation spectrum at (b) 20 y_0^+ and (c) 70 y_0^+. At 20 y_0^+, the low-frequency fluctuations are suppressed but fluctuation components at the modulation frequency and its higher-order harmonics (i.e., 50Hz, 100Hz, etc) are enhanced. At 70 y_0^+, all fluctuation components are enhanced.

It is known that the low-frequency fluctuations in the spectra are associated with the large eddies in TBL, which are responsible for energy extraction from mean flow motion and energy cascade into smaller eddies (AAR Townsend, 1980). The reduced low-frequency fluctuations in figure 7.8 (b) indicates the large turbulent eddies in the near-wall region are suppressed. Without energy-supplying large eddies, the near-wall turbulence faces challenges to survive. The phenomenon of suppressed low frequency fluctuations was also observed in the spectrum of re-laminarizing TBL (Mukund et al., 2006).

With reduced low-frequency fluctuations, the enhanced streamwise turbulent intensity at 20 y_0^+ must come from the enhanced high-frequency fluctuations. The spectra peaking frequencies (50Hz, 100Hz, etc) point out the source of enhanced turbulent fluctuations to be the periodic air-film oscillation. Because of the deterministic nature, the increased fluctuations are considered 'inactive' turbulence and are considered benign for the wall-shear stress generation. To this end, the dominance of 'inactive' turbulence in the near-wall region shown in figure 6.5 is again seen in the turbulent spectra.

7.4 Discussion

The re-laminarization process we discuss here is not the same as the previously studied re-laminarization process under the effect of favorable pressure gradient, in which the turbulent intensity gradually drops over some developing distance (Warnack and Fernholz, 1998; Bourassa and Thomas, 2009). In the current scenario, the re-laminarization process only happens in the near-wall region where negative turbulent kinetic energy production is observed. The negative turbulent kinetic energy production is expected to supply energy to mean flow motion and oscillatory flow motion. However, the mean flow velocity (shown in figure 6.1) in the near-wall region decreases rather than increases. This could be related to the pressure-strain-rate term ($-\frac{1}{\rho}\left(\overline{PU_i}\right)\delta_{ij}$) on the right-hand side of equation B.1 shown in Appendix B. The pressure-strain-rate term can potentially remove the mean flow kinetic energy through the process of air-films being compressed by TBL. One interesting observation is that the air-films continuously expanded when under large amplitude modulation. Because no air was supplied to the air-pocket during pressure modulation process, it is suspected that the air-pocket temperature increased because of TBL compression work. The air-film expanded under the effect of increased air-pocket temperature. This hypothesis could potentially explain the observation that mean flow velocity does not increase in the presence of kinetic energy supply from turbulent motion. However, it still needs to be verified by future experimental measurements.

In the same region that negative turbulent kinetic energy is produced, both the Reynolds shear stress and viscous shear stress are suppressed (shown in figure 6.4). However, the turbulent intensity is increased due to the strong production of 'inactive' turbulence. These observations seem to be connected with the modified vorticity field shown in figure 6.3, in which the near-wall transverse vorticity is *'lifted up'* over the air-films. AA Townsend (1961) proposed that 'inactive' turbulence is *'a meandering or swirling motion made up from attached eddies of large size which contribute to the Reynolds stress much farther from the wall than the points of observation'* (but not at the observation point). Based on this insightful idea, we propose one potential mechanism for the re-laminarization process here:

With the near-wall transverse vorticity pushed away from the wall, large eddies in the near-wall region are suppressed due to insufficient vorticity source. As a result, *'active'* turbulence in the near-wall region losses energy supply and cannot be sustained. Following Townsend's argument, the near-wall turbulence can be

induced by the vortex structures formed away from the wall (shown in figure 6.3) and thus mainly 'inactive'. The Reynolds shear stress (shown in figure 6.4 (b)) is suppressed near the wall but elevated in regions away from the wall, which agrees well with Townsend's argument that 'inactive' turbulence does not produce Reynolds shear stress at the observation point but could contribute to the Reynolds shear stress farther away from the wall. Bradshaw (1967a) found that the 'inactive' turbulence 'does not transfer momentum'. To that end, the dominance of 'inactive' turbulence in the re-laminarization region is in line with the conclusion of Chapter 5 that momentum transfer toward the wall is suppressed.

Because of the limitation of two-dimensional DPIV, the detailed mechanisms for the re-laminarization process remain unclear and the proposed mechanism based on Townsend's description about 'inactive' turbulence cannot be verified currently. Future in-depth studies such as direct numerical simulations (DNS) may provide a more complete description of the physical process.

7.5 Summary for Chapter 6 and 7

In chapter 6 and 7, we demonstrate that with the generation of strong time-varying transverse vorticity, the near-wall mean transverse vorticity is pushed away from the wall. In the near-wall region, the Reynolds shear stress is suppressed and 'inactive' turbulence is dominant. A strong velocity gradient is induced near the wall and the TBL shape factor increases over the air-films. A negative turbulent kinetic energy production mechanism in the near-wall region is identified. With negative turbulent kinetic energy production, energy is extracted from turbulence and transferred to the mean flow motion as well as the oscillatory motion. Therefore, the near-wall turbulence losses energy and re-laminarization process is confirmed.

The re-laminarization process happens together with the suppression of large turbulent eddies and production of 'inactive' turbulence, which can be connected to the observation that the near-wall vorticity is pushed away from the wall and forms eddy-like structures. One potential physical mechanism based on the viewpoint of AA Townsend (1961) about 'inactive' turbulence is proposed. Future in-depth studies are needed to verify this proposed mechanism.

Because the re-laminarization process mainly happens near the wall, which is the most critical region for wall-shear stress generation, the turbulent skin friction is expected to reduce in the air-film region. The re-laminarization mechanism induced by oscillating air-films has promising potential to be utilized for developing future

turbulent drag reduction techniques.

Chapter 8

POTENTIAL TURBULENT DRAG REDUCTION EFFECT

The analysis shown in Chapter 4 - 7 demonstrates that the momentum transfer toward the wall is suppressed and the near-wall turbulence re-laminarizes in the vicinity region of oscillating air-films. Therefore, the wall skin friction is expected to decrease. However, the exact skin friction coefficient is unknown. Further, even if the wall skin friction reduces, the turbulent drag reduction effect may be compromised by potential form drag on the air-films. Because the oscillating air-films always protrude into the TBL, they may act like dynamic roughness and induce local form drag. For example, the phase snapshot of unsteady streamwise acceleration shown in figure 5.1 (a) is re-plotted in figure 8.1, which demonstrates that a large backward acceleration field is induced in the downstream of air-films in the phase when the air-film still protrudes into TBL. Because of the large air-film protrusion height, the backward acceleration downstream of air-films may contain the contribution of form drag, which can nullify the benefits of reduced skin friction. To address these concerns, this chapter first analyses potential form drag followed by estimating the wall skin friction.
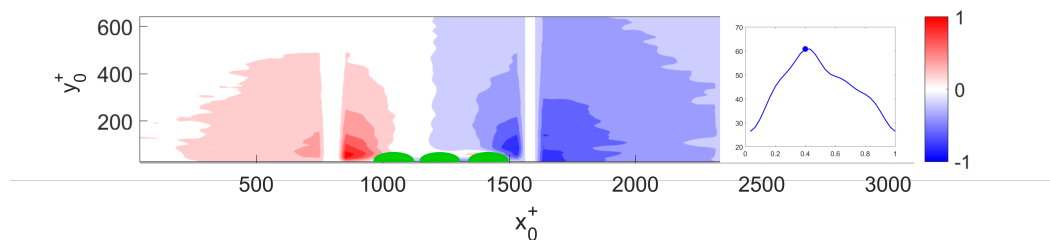
Figure 8.1: The fourth phase snapshot of phase-averaged streamwise acceleration ($\frac{d(\widetilde{U})}{dt}$) shown in figure 5.1 (a) in which backward acceleration downstream of air-films is observed

8.1   Potential Form Drag

The potential form drag generated on air-films can be estimated using the formula $F_D = \Delta P.h$, where ΔP is the pressure drop across the air-film and h is the air-film height. Based on the Bernoulli principle, ΔP can be approximated as $\frac{1}{2}\rho \left(u_0^2(y) - u_s^2(y) \right)$, where $u_0(y)$ is the character velocity far away from the air-films and $u_s(y)$ is the velocity on the downstream side of air-films. Both velocities depend

on the distance from the wall y. To obtain an upper bound of the form drag, we assume the characteristic velocity u_0 to be the free stream velocity (0.438 m/s), $u_s = 0$, and the air-film height (h) to be its maximum (2.6 mm). The combination of these parameters is expected to give the largest F_D ever possible.

Because the form drag on air-films slows down the flow velocity and contributes to the backward acceleration in TBL, we estimate the TBL integrated backward acceleration and compare it with the upper-bound of potential form drag. Such comparison reflects the significance of potential form drag. The integrated backward acceleration is expressed as $I_{\frac{d(\widetilde{U})}{dt}} = \rho \int \frac{d(\widetilde{U})}{dt} dA$, where A is the total x-y plane area in the downstream of air-films. To make a fair comparison, $I_{\frac{d(\widetilde{U})}{dt}}$ in the phase with maximum air-film height is compared with F_D. The ratio of F_D to $\frac{I_{d(\widetilde{U})}}{dt}$ is 0.056 which shows that the observed backward acceleration is much larger than the largest possible form drag. This order-of-magnitude analysis shows that the observed backward acceleration is not generated by form drag. Instead, it is mainly a result of oscillating air-films. Therefore, the effect of potential form drag on air-films is trivial when compared to the effect of air-film oscillation for the current TBL. In this sense, we argue that the potential form drag is not a major factor for the previously mentioned TBL modifications and is not expected to significantly contribute to the drag force on the air-films.

8.2 Estimating the Wall-Skin Friction Reduction

Estimating the wall-skin friction is very challenging for unsteady TBL like the one examined here. We can estimate the turbulent friction coefficient using the Clauser chart method (Clauser, 1954). As was disucssed in Chapter 2, the Clauser chart method determines wall frictional velocity by fitting the velocity profile log region (presented in Chapter 1) to a straight line with a fixed slope equal to $\frac{1}{\kappa}$. As a result, the Clauser chart method can only estimate the frictional velocities for TBL profiles that have a log layer. For velocity profiles that do not have a log layer, i.e., those very close to the air-films, the Clauser chart method does not work. In regions at certain distance away from the air-films, such as the upstream and downstream regions of air-films, the velocity profiles demonstrate log layers. As was mentioned in Chapter 2, the final portion of the velocity profile used for determining $u_{\tau 0}$ was between 40 y_0^+ to 0.2 δ_0, well within the range of log layer defined by Pope (2001). The Clauser chart method has previously generated good approximations of wall friction for TBL with unsteady acceleration (Le, Moin, and J. Kim, 1997). Therefore, we can use the

Clauser chart method to estimate the skin friction coefficient at the upstream and downstream regions of air-films. The wall skin friction coefficient in the presence of flat, bulged and 50 Hz modualted bulged air-film is estimated using the Clauser chart method. The detailed air-film configuration and TBL conditions are given in Chapter 4.

With 50 Hz modulation, the phase-averaged velocity profile $(\overline{U} + \widetilde{U})$ is used to estimate the skin friction (C_f). The skin friction coefficient is expressed as $C_f = 2u_\tau^2/\overline{U_e}^2$, where $\overline{U_e}$ is the velocity at 1.3 δ_0 from the wall. Figure 8.2 shows the temporal change of C_f in a period cycle at four streamwise locations (400 x_0^+, 2000 x_0^+, 2800 x_0^+, 3600 x_0^+). At all four locations, C_f periodically oscillates with a mean value lower than the baseline skin friction coefficient C_{f0}. C_f substantially decreases in the downstream of air-films and gradually relaxes thereafter.
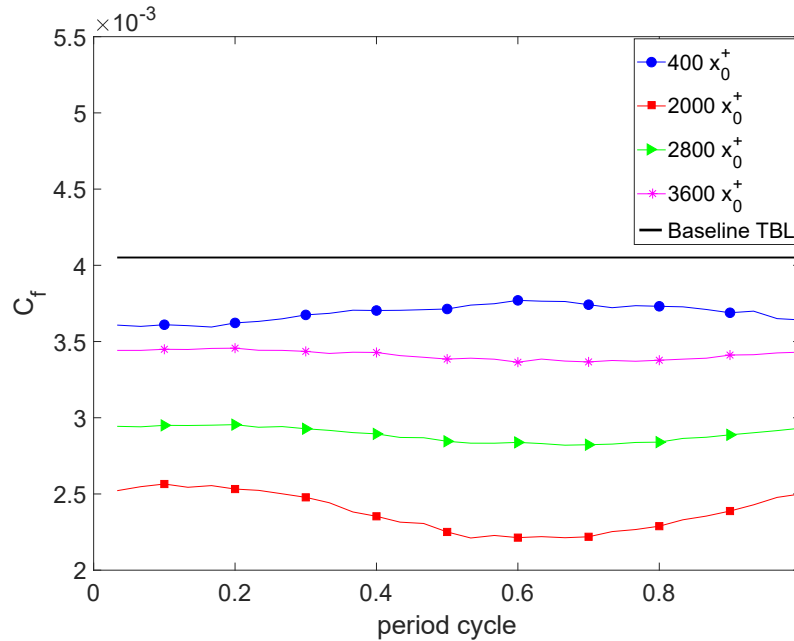
Figure 8.2: Skin friction coefficient (C_f) temporal variation at various streamwise locations in one modulation cycle. Symbols are shown in the plot.

Figure 8.3 shows the skin friction coefficient estimated using the mean velocity profile $(\overline{U})$ and compares it with the average value of C_f estimated using the phase-averaged velocity $(\overline{U}+\widetilde{U})$. The air-film covered area is excluded from the calculation. Figure 8.3 shows that C_f estimated using the two velocity profiles are very similar, indicating the versatility and robustness of the Clauser chart method here. The skin friction reduction, defined as $R_{cf} = \frac{C_{f0}-C_f}{C_0}$, is plotted in figure 8.4. Trivial reduction

in the upstream region and substantial reduction (with a maximum of approximately 40%) downstream of air-films is observed. The skin friction reduction effect gradually disappears farther downstream. The estimated skin friction coefficient is in line with the trend of reduced viscous shear stress shown in figure 4.16.
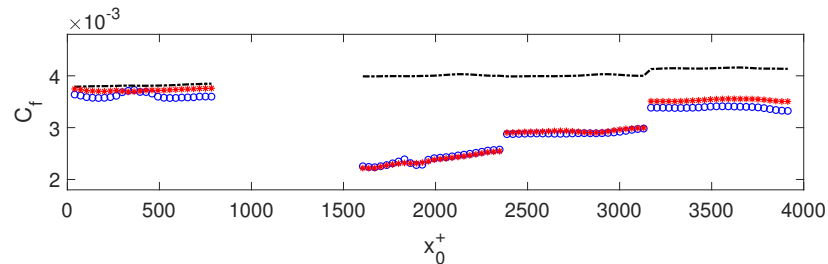
Figure 8.3: Skin friction coefficient (C_f) estimated using time-mean velocity ($\overline{U}$) profile and phase-averaged velocity ($\overline{U} + \widetilde{U}$) profiles. The air-film region (between 900 x_0^+ and 1500 x_0^+) is excluded from the calculation. Symbols: blue circle, the average of C_f estimated using ($\overline{U} + \widetilde{U}$); red triangle, C_f estimated using ($\overline{U}$); Dashed-line, baseline TBL skin friction coefficient (C_{f0})
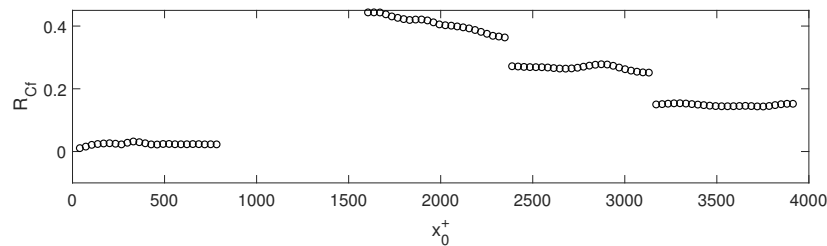
Figure 8.4: Skin friction reduction (R_{cf}) in the vicinity region of 50 Hz modulated bulged air-film. The air-film region (between 900 x_0^+ and 1500 x_0^+) is excluded from the calculation.

The skin friction reduction for the passively maintained bulged and flat air-film cases are given in figure 5. With bulged air-films, there is a slight skin friction increase (approximately 8%) upstream and 14% skin friction decrease downstream. With flat air-films, the friction coefficient is almost identical to the baseline case and no skin friction reduction is observed.

The estimated skin friction reduction effect with differently conditioned air-films is in line with the observation that near-wall vorticity is pushed away from the wall over oscillating air-films and relaxes back toward the wall downstream of air-films. The skin friction estimated using the Clauser chart method agrees well with the reduced viscous shear stress shown in figure 4.16 and figure 4.17.
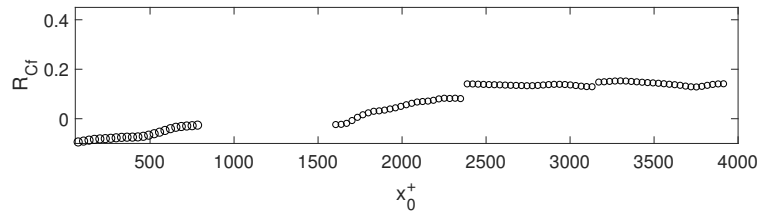
(a) R_{cf} with bulged air-film
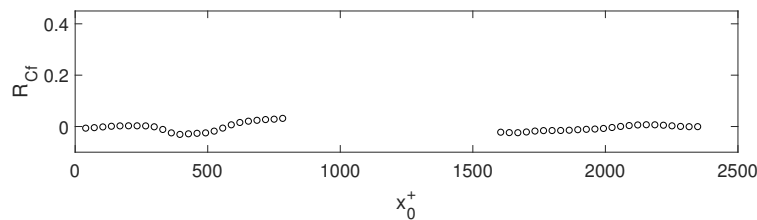
(b) R_{cf} with flat air-film

Figure 8.5: Skin friction reduction (R_{cf}) in the vicinity region of unmodulated (a) bulged air-film and (b) flat air-film. The air-film region (between 900 x_0^+ and 1500 x_0^+) is excluded from the calculation.

In summary, this chapter discusses the potential form drag and skin friction reduction in the presence of oscillating air-films. By an order-of-magnitude analysis, the potential form drag is shown to be insignificant. The wall-skin friction in regions where velocity profiles demonstrate log layers is estimated using the Clauser chart method. Substantial skin friction reduction is observed in downstream of modulated air-films. With passive air-films, the skin friction reduction effect is less obvious. The estimated skin friction is consistent with the results shown in Chapter 4 and 5 such as the reduced near-wall viscous shear stress. Although the skin friction in the air-film covered region cannot be estimated, with the understanding that momentum transfer toward the wall is suppressed and near-wall turbulence re-laminarizes, even larger skin friction reduction is expected.

Chapter 9

PARAMETER STUDY AND NON-DIMENSIONAL ANALYSIS

Chapter 4 and 5 demonstrated that vorticity injected by oscillating air-films modifies the momentum transfer process in TBL. With even stronger vorticity injection, Chapter 7 showed that turbulence in the vicinity of air-film re-laminiarize. It is therefore desirable to dynamically control the near-wall turbulence behaviour, which is the focus of this chapter. However, air-film dynamic oscillation in TBL is a highly non-linear process and can be influenced by a broad spectrum of parameters, such as air-film size and concavity configuration, TBL Reynolds number and dynamic modulation conditions. Because of the limitation of space and time, the effect of a few representative parameters will be selectively studied. Based on the gained understanding, a preliminary non-dimensional analysis is conducted.

9.1 Effect of Dynamic Modulation

The dynamic modulation can be varied by changing the modulation function profile, signal amplitude and frequency. To isolate the effect of dynamic modulation, all other control conditions were maintained the same. In this test, 8 mm sized air-films were sustained over a large dimple surface (**Design 4** dimple surface), i.e., 12 air-films were sustained along the streamwise direction in TBL with Re_θ equal to 1200. In the assembled FOV (with a streamwise span from 0 x_0^+ to 3900 x_0^+), the air-films were between 760 x_0^+ and 3200 x_0^+. The air-film was initially set in bulged configuration with a fixed maximum height of 2 mm, although it may be changed by dynamic modulation. The dynamic modulation output power was set at two levels, with the higher-level output power four times larger than the lower-level output power. The modulation frequencies were selected within the range between 5 Hz and 50 Hz. Both sinusoidal and saw-tooth shaped modulation profiles were tested. The tested parameters and corresponding air-film oscillation information are listed in Table 9.1.

Similar TBL modifications as those shown in Chapter 4 - 7, such as modified mean streamwise velocity, a zero-shear-stress layer, increased TBL shape factor and wave shear stress $-\overline{\widetilde{U}\widetilde{V}}$. The mean streamwise velocity ($\overline{U}$) profiles at different streamwise locations are shown in figure 9.1, which are similar to those shown in figure 4.3. The near-wall velocity reduces over the air-films region and the slope of log region

Test case	Modulation function	f (Hz)	$\frac{f\nu}{u_{\tau 0}^2}$	Power (W)	h (mm)	h (δ_{y0})	A (mm)	A (δ_{y0})
1	none	none	none	2.2	48	0.43	9	
2	sinusoidal	5	0.012	0.13	2.58	57	0.46	10
3	sinusoidal	20	0.046	0.13	2.45	54	0.55	12
4	sinusoidal	20	0.046	0.56	3.13	69	0.47	10
5	saw-tooth	20	0.046	0.56	2.6	58	0.72	16
6	sinusoidal	50	0.115	0.13	2.4	54	0.3	7

Table 9.1: Dynamic modulation conditions

is changed. However, in regions upstream and downstream of the air-films, velocity profile log region can be observed. The total shear stress, i.e, $-\overline{u'v'} - \overline{\widetilde{U}\widetilde{V}} - \overline{UV}$ for modulated air-film cases and $-\overline{u'v'} - \overline{UV}$ for passive air-film cases, are selectively presented in figure 9.2 (a) – (f). The total shear stress contours are all similar to that shown in Chapter 4. For example, in the region over air-films, the total shear stress is negative in the outer part of TBL but is positive near the wall. Downstream of air-films, total shear stress is mainly positive. The zero-shear-stress layers are observed in regions where the shear stresses change sign. As was discussed in Chapter 5, the zero-shear-stress layer interrupts the momentum transfer from the fast TBL outer layer toward the wall.
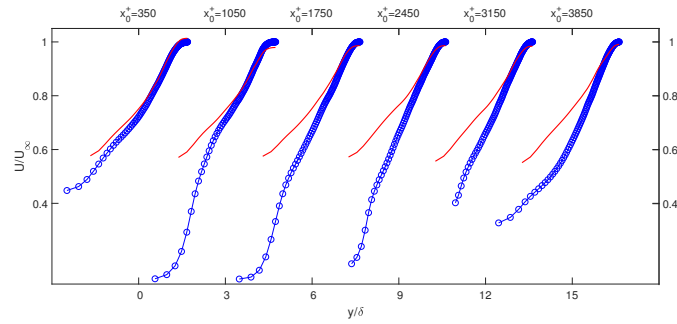
(a) no modulation
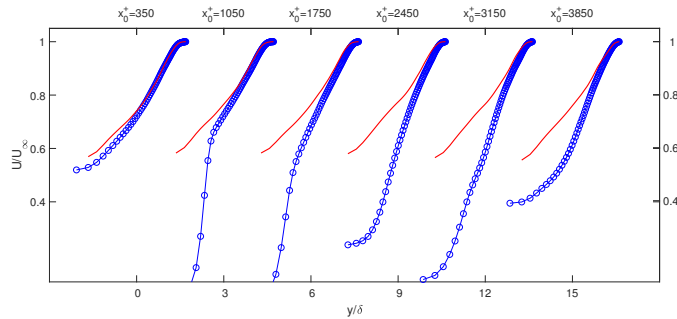
(b) 5 Hz low-power modulation
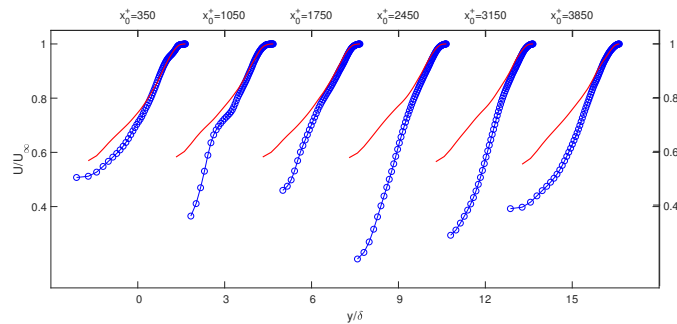
(c) 20 Hz low-power modulation
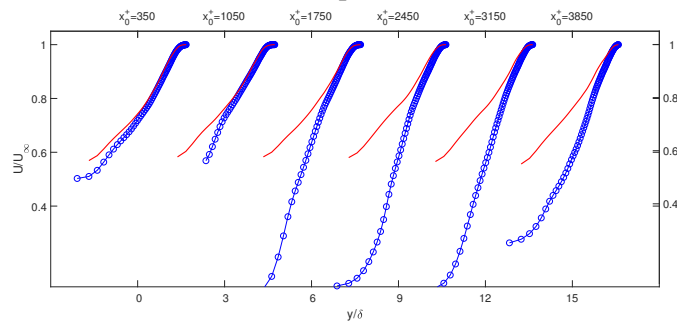
(d) 20 Hz high-power modulation
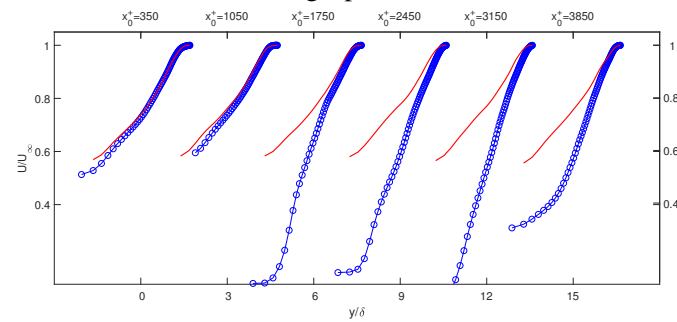
(e) 20 Hz high-power modulation with saw-tooth modulation function
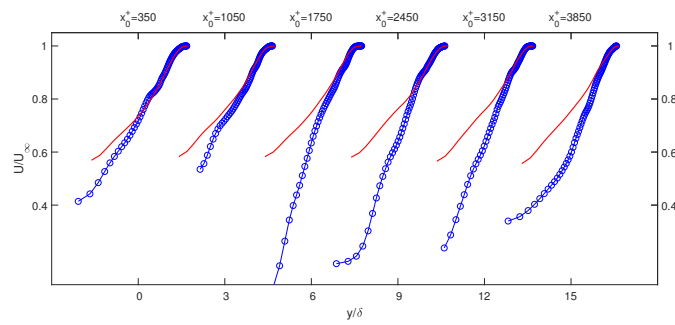
(f) 50 Hz low-power modulation

Figure 9.1: Mean $\overline{U}$ profiles in the vicinity of oscillating air-films under various dynamic modulation conditions. The profile streamwise locations are shown on the top axis. Symbols: blue circle: air-film cases; red solid line: baseline TBL. Air-films are between 760 x_0^+ and 3200 x_0^+.
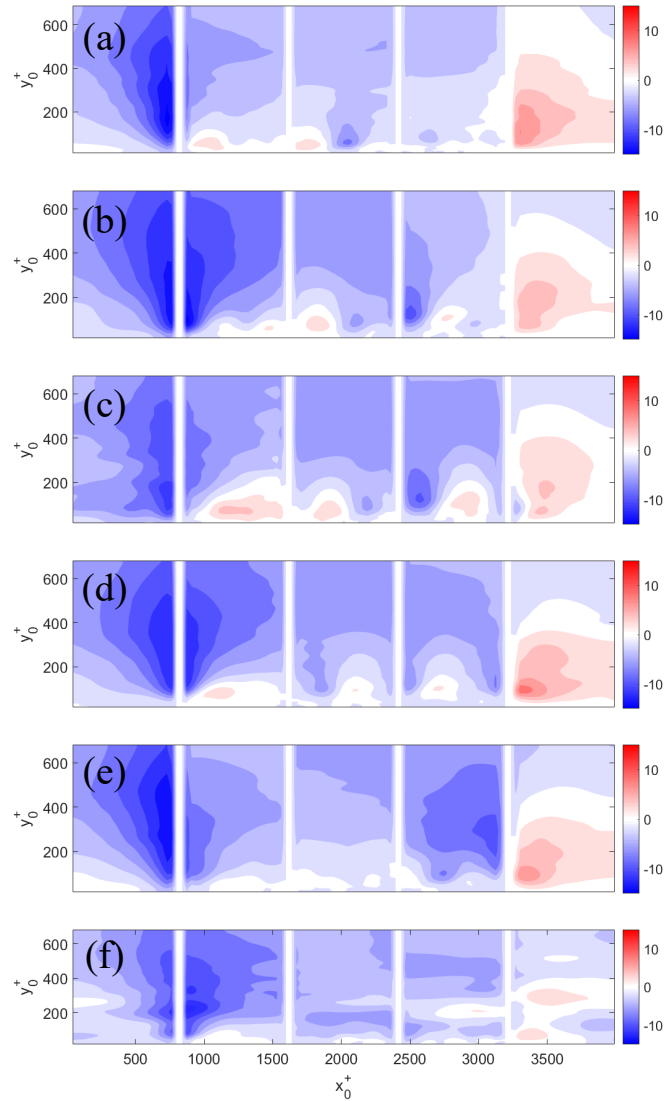
Figure 9.2: Total shear stress contour in the vicinity region of oscillating air-films under various dynamic modulation conditions. The modulation conditions are (a) no modulation (b) 5 Hz low-power modulation (c) 20 Hz low-power modulation (d) 20 Hz high-power modulation (e) 20 Hz high-power modulation with saw-tooth profile and (f) 50 Hz low-power modulation. Air-films are between 760 x_0^+ and 3200 x_0^+.

The TBL shape factors (H^*) for all test cases are given in figure 2.In all cases, H^* increase over the air-films and decrease downstream of air-films. When compared with the case shown in Chapter 7 in which re-laminarization was observed, the shape factors are of lower values. With pressure modulation, the TBL shape factors seem to increase compared with the passive air-film case. With high-power modulation, the TBL shape factors are slightly higher, as is shown by test cases 4 and 5 (20 Hz with high-power modulation).
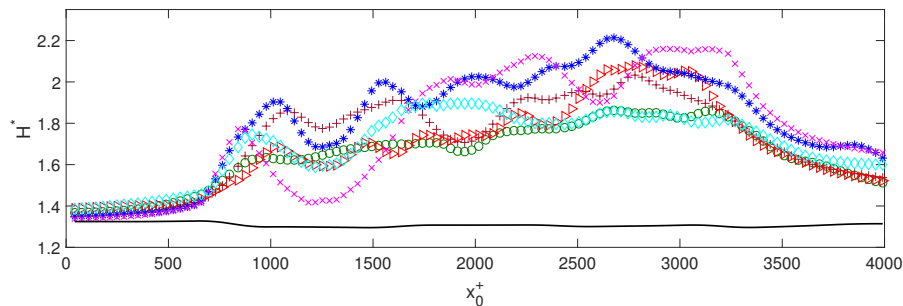
Figure 9.3: TBL shape factor (H^*) over air-film region with various dynamic modulation conditions. Symbols: circle, passive bulged air-film; plus sign, 5 Hz low-power modulation; triangle, 20 Hz low-power modulation; star, 20 Hz high-power modulation; cross, 20 Hz high-power modulation with saw-tooth profile; diamond, 50 Hz low-power modulation; solid line, baseline TBL. Air-films are between 760 x_0^+ and 3200 x_0^+.

Not all observations shown in Chapter 4 occur in the test cases, such as the wave shear stress ($-\widetilde{U}\widetilde{V}$). Figure 9.4 shows the time-averaged wave shear stress ($-\overline{\widetilde{U}\widetilde{V}}$) for all test cases. It is found $-\overline{\widetilde{U}\widetilde{V}}$ is not visible with low-power 5 Hz and 20 Hz modulation. However, $-\overline{\widetilde{U}\widetilde{V}}$ shows up with high-power 20 Hz modulation or low-power 50 Hz modulation. It seems the oscillatory motions are only produced when the oscillation frequency and amplitude, or their product is large enough. This observation indicates that the air-film oscillation amplitude and frequency might be critical for the generation of organized flow structures. Some preliminary non-dimensional analysis will be discussed in Section 9.3.
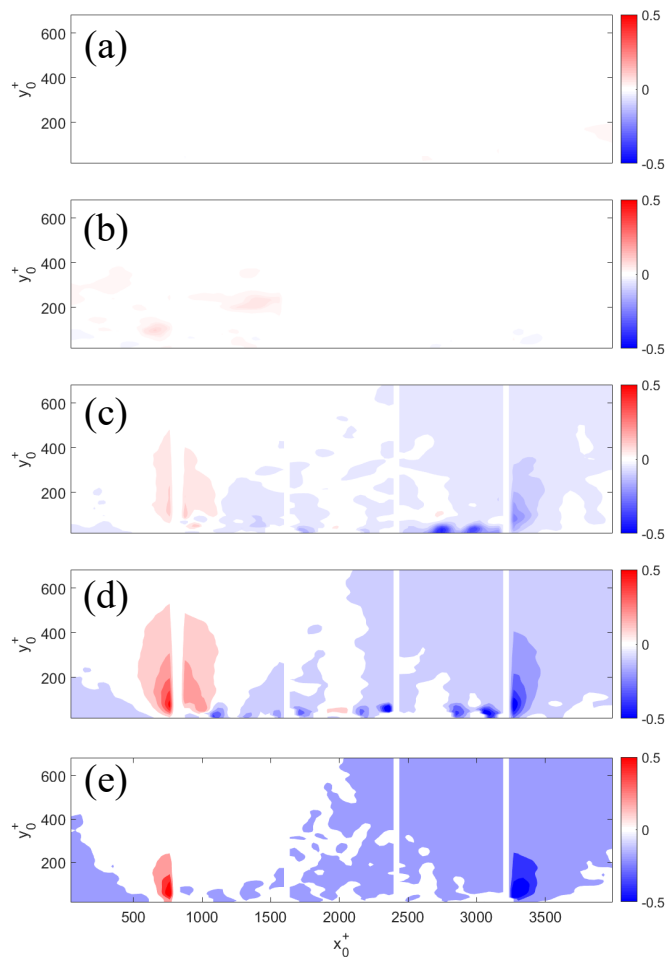
Figure 9.4: Time-averaged wave shear stress ($-\overline{\widetilde{U}\widetilde{V}}$) contour under various modulation conditions. The modulation conditions are (a) no modulation (b) 5 Hz low-power modulation (c) 20 Hz low-power modulation (d) 20 Hz high-power modulation (e) 20 Hz high-power modulation with saw-tooth profile and (f) 50 Hz low-power modulation. Air-films are between 760 x_0^+ and 3200 x_0^+. Air-films are between 760 x_0^+ and 3200 x_0^+.

9.2 Effect of TBL Reynolds Number and Air-film Dimension

To investigate the effect of Reynolds number, air-films were sustained in TBLs with Re_θ equal to 1200 and 2200. The air-films were formed over dimple surface **Design 2** and **Design 3**, which sustain 8 mm and 4 mm sized air-films, respectively, while maintaining the same air-film coverage ratio (80% of the total surface). The 4 mm and 8 mm sized air-films were initially set to bulge out into TBL for 2 mm and 1 mm respectively. Therefore, the air-films in both test cases are of a similar configuration. Through all the tests, air-films were modulated by a fixed 50 Hz sinusoidal signal. Because the TBL inner scale depends on TBL Reynolds number,

the air-films streamwise span is from 170 x_0^+ to 1300 x_0^+ in TBL with Re_θ equal to 1200 and from 290 x_0^+ to 2200 x_0^+ in TBL with Re_θ equal to 2200.

Figure 9.5 (a) and (b) depict the TBL shape factor (H^*) in two different Reynolds number TBLs, which show elevated H^* over both 4 mm and 8 mm sized air-films. With larger-sized air-films, the TBL shape factors are relatively higher in both TBLs, probably because of the more compliant air-film interface. The elevated shape factor relaxes to the baseline case downstream of air-films. However, the relaxation process finishes in a shorter distance in TBL with higher Reynolds number. The TBL shape factor depends on both the air-film size and TBL Reynolds number. A potential optimal air-film size for effectively modifying the TBL might exist for TBL with certain Reynolds number. The details require future in-depth studies.
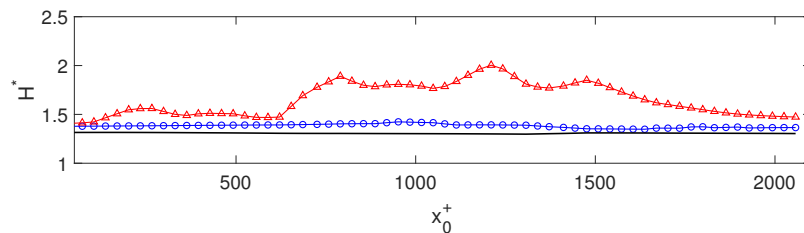
(a) shape factor (H^*) of TBL at Re_θ = 1200. The air-films are located between 170 x_0^+ and 1300 x_0^+.
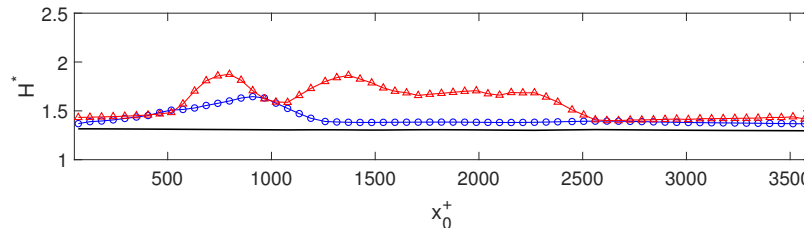
(b) shape factor (H^*) of TBL at Re_θ = 2200. The air-films are between 290 x_0^+ and 2200 x_0^+.

Figure 9.5: Shape factor (H^*) of TBL with (a) Re_θ = 1200 and (b) Re_θ = 2200 in the presence of 50 Hz modulated air-films. Symbols: circle, 4 mm air-film; triangle, 8 mm air-film; solid line, baseline TBL.

9.3 Non-dimensional Analysis

It is desirable to model the air-film/TBL dynamic interaction using non-dimensional parameters. However, due to the highly unsteady and non-linear nature of air-film/TBL interaction and also the vast parameter space, constructing a complete non-dimensional air-film/TBL interaction model is almost impossible. Although it is difficult to search through the complete parameter space, a few important

non-dimensional parameters have been identified.

As was shown in Section 9.1, the air-film oscillation frequency f and amplitude Δh are critical for the onsets of organized flow structures such as Stokes-type oscillatory motion and wave shear motion ($\widetilde{U}\widetilde{V}$). The product $f\Delta h$ has the dimension of velocity, which can be understood as the periodic velocity induced by the oscillating air-films. Because the periodic velocity mainly exists in the near-wall region, the velocity ratio $\frac{f\Delta h}{u_{\tau 0}}$ represents the relative significance of the oscillatory velocity to the TBL inner layer velocity. The streamwise oscillatory velocity ($\widetilde{U}$) is detectable from the near-wall region up to the maximum air-film height (h), which defines a length scale for the organized flow motions. To this end, the length scale ratio $\frac{hu_{\tau 0}}{\nu}$ is also important. In the case shown in Chapter 7 in which re-laminarization is observed, the following values are found for the above-mentioned quantities: $\Delta h = 1.6mm$, $h = 2.4mm, f = 50Hz, u_{\tau 0} = 0.02m/s$. With these values the velocity ratio $\frac{f\Delta h}{u_{\tau 0}}$ is equal to 4, which is close to the amplitude of Stokes-type oscillatory motion shown in figure 6.1 (b). The length ratio $\frac{hu_{\tau 0}}{\nu}$ is 48, which approximately reflects the length scale of streamwise oscillatory velocity. Based on this set of velocity and length scale, an oscillatory Reynolds number Re_o can be defined as shown in equation 9.1 .

$$Re_o = \frac{f\Delta h h}{\nu} \tag{9.1}$$

In the re-laminarization case, Re_o is approximately 175. Hino et al. (1983) found that a purely oscillating flow remains laminar if $Re_o < 400$. The oscillatory Reynolds number Re_o is consistent with the observation that Stokes-type oscillatory motion remains laminar-like. The oscillatory velocity has a significant impact on the near-wall turbulence dynamics. If $f\Delta h$ is large, the near-wall region turbulent motion is not determined by the inner layer Reynolds number Re_τ only, but is also influenced by the oscillatory Reynolds number Re_o.

From the air-film induced vorticity point of view, the oscillatory motions can be understood as induced by periodically varying vorticity. In this end, $f\Delta h$ represents the velocity induced by vorticity and Δh represents the dimension of injected vorticity. Therefore, the product of velocity ratio and length ratio $\frac{f\Delta h}{u_{\tau 0}}\frac{\Delta h u_{\tau 0}}{\nu} = \frac{f\Delta h^2}{\nu}$ may reflect the amount of vorticity generated by oscillating air-films. It is found that the generated vorticity is independent of TBL intrinsic scales, which is a reasonable guess as vorticity was injected into still water when no TBL presented.

A length ratio $\frac{\Delta h}{R}$ seems to be important as well, where R is the mean air-film radius. As was briefly mentioned in Chapter 7, with initially flat air-films, strong vorticity is generated in the near-region of air-films. A preliminary guess is with small R the air-film surface tension effect is weaker, therefore the air-film expansion and contraction processes are less constrained and thus can generate stronger vorticity. More non-dimensional analysis for air-film dynamic oscillation is discussed in Appendix C

In summary, this chapter demonstrated several parameter studies for the modification effect on TBLs. Control parameters such as dynamic modulation, air-film size and Reynolds number are briefly analyzed. In the dynamic modulation study, the previously observed zero-shear-stress layer and elevated TBL shape factor (H^*) are observed in the near-region air-films. The wave shear stress ($-\overline{\widetilde{U}\widetilde{V}}$) is only visible with large enough air-film oscillation frequency and amplitude. The elevated TBL shape factor can be influenced by air-film size and TBL Reynolds number. Non-dimensional analysis shortlists a few key non-dimensional parameters. A new set of velocity and length scale is identified in the near-wall region, which defines an oscillatory Reynolds number Re_o. Together with TBL inner Reynolds number Re_τ, Re_o influences the near-wall turbulence dynamics. The complete air-film/TBL interaction mechanism requires future in-depth studies. The results of this chapter might be useful for the search of a potentially optimal turbulent drag reduction strategy.

Chapter 10

CONCLUSION

In this thesis work, an innovative air-retaining system that can manipulate the near-wall turbulence in hydrodynamic TBL was developed. Motivated to address the constraints of existing hydrodynamic drag reduction techniques, this work explored enhancing wall-attached air-films' stability in TBL and controlled the air-film's interaction with near-wall turbulence. Through the combination of surface textures (surface dimple) and patterned surface wettability, we demonstrate that wall-attached air-films can be sustained in TBL and their static configuration and dynamic oscillation can be controlled.

It is found that dynamically modulated air-films generate vorticity in both still water and TBLs. TBL is greatly modified in the presence of oscillating air-films. With dynamic modulation, a layer of zero-shear-stress exists over the air-film covered region. In the vicinity region of oscillating air-films, 'inactive' turbulent motion dominates, and the viscous shear stress substantially reduces in the near-wall region.

The physical mechanisms behind these modifications are potentially related to the air-film generated vorticity interacting with TBL near-wall vortical structures. It is observed that the near-wall transverse vorticity is *'pushed away'* from the wall. As a result, the near-wall transverse vorticity reduces and the displaced vorticity forms large vortex structures. The modified vorticity field provides a plausible explanation for the modifications in TBL. Analysis shows that turbulent momentum transfer toward the wall is suppressed in the air-film region, which indicates reduced wall-skin friction.

Besides the momentum transfer process, the energy exchange process in the near-wall region is also significantly modified. A re-laminarization mechanism is induced near the wall through negative turbulent kinetic energy production, which not only cuts the energy supply for turbulence but also directly reduces the turbulent kinetic energy. As a result, in the near-wall region, turbulent large eddies are suppressed and strong 'inactive' turbulent motion is produced. Following Townsend's insightful comments about 'inactive' turbulence, the above observations seem to be related to the process of near-wall vorticity being *'pushed away'* from the wall and forming eddy-like structures. Other observations such as reduced near-wall Reynolds shear

stress also supports this hypothesis. Future in-depth investigation is needed to verify the hypothesis. Because the near-wall region is critical for the generation of wall-shear stress, the re-laminarization mechanism indicates reduced skin friction.

Through an order-of-magnitude analysis, the potential form drag on air-films is shown to be irrelevant. Estimated using the Clauser chart method, the wall-skin friction substantially reduces (up to 40%) downstream of air-films. Parameter studies shortlist a few critical control parameters for effectively modifying TBL. The preliminary non-dimensional analysis points to a new set of velocity and length scales generated in the near-wall region by oscillating air-films, which influences the near-wall turbulence dynamics. The complete mechanism for air-film/TBL will require future studies.

One limitation of the current study is its two–dimensional perspective for the essentially three-dimensional air-film/TBL interaction process. Therefore, detailed physical mechanisms such as the process of near-wall vortical structures being *'pushed away'* remain unknown. To address this concern, one future work worth exploring is to investigate the streamwise vorticity field, especially in the edge-region of air-film array. Such work may shed light on the understanding of vorticity dynamics in turbulent shear flow.

BIBLIOGRAPHY

Batchelor, CK and GK Batchelor (1967). *An introduction to fluid dynamics*. Cambridge university press.

Bidkar, Rahul A et al. (2014). "Skin-friction drag reduction in the turbulent regime using random-textured hydrophobic surfaces". In: *Physics of Fluids* 26.8, p. 085108.

Bobba, Kumar Manoj (2004). "Robust flow stability: theory, computations and experiments in near wall turbulence". PhD thesis. California Institute of Technology.

Bourassa, Corey and FO Thomas (2009). "An experimental investigation of a highly accelerated turbulent boundary layer". In: *Journal of Fluid Mechanics* 634, pp. 359–404.

Bradshaw, P (1967a). "'Inactive' motion and pressure fluctuations in turbulent boundary layers". In: *Journal of Fluid Mechanics* 30.2, pp. 241–258.

– (1967b). "The turbulence structure of equilibrium boundary layers". In: *Journal of Fluid Mechanics* 29.4, pp. 625–645.

Ceccio, Steven L (2010). "Friction drag reduction of external flows with bubble and gas injection". In: *Annual Review of Fluid Mechanics* 42, pp. 183–203.

Choi, Chang-Hwan and Chang-Jin Kim (2006). "Large slip of aqueous liquid flow over a nanoengineered superhydrophobic surface". In: *Physical review letters* 96.6, p. 066001.

Clauser, Francis H. (1954). "Turbulent boundary layers in adverse pressure gradients". In: *Journal of the Aeronautical Sciences* 21.2, pp. 91–108.

Coles, Donald (1956). "The law of the wake in the turbulent boundary layer". In: *Journal of Fluid Mechanics* 1.2, pp. 191–226.

Cutler, Andrew D and James P Johnston (1989). "The relaxation of a turbulent boundary layer in an adverse pressure gradient". In: *Journal of Fluid Mechanics* 200, pp. 367–387.

De Graaff, David B and John K Eaton (2000). "Reynolds-number scaling of the flat-plate turbulent boundary layer". In: *Journal of Fluid Mechanics* 422, pp. 319–346.

Dean, Brian and Bharat Bhushan (2010). "Shark-skin surfaces for fluid-drag reduction in turbulent flow: a review". In: *Philosophical Transactions of the Royal Society A: Mathematical, Physical and Engineering Sciences* 368.1929, pp. 4775–4806.

Elbing, Brian R et al. (2008). "Bubble-induced skin-friction drag reduction and the abrupt transition to air-layer drag reduction". In: *Journal of Fluid Mechanics* 612, pp. 201–236.

Fukuda, Kazuhiro et al. (2000). "Frictional drag reduction with air lubricant over a super-water-repellent surface". In: *Journal of Marine Science and Technology* 5.3, pp. 123–130.

Garcia-Mayoral, Ricardo, Garazi Gómez-de-Segura, and Chris T Fairhall (2019). "The control of near-wall turbulence through surface texturing". In: *Fluid Dynamics Research* 51.1, p. 011410.

Garcia-Mayoral, Ricardo and Javier Jiménez (2011). "Hydrodynamic stability and breakdown of the viscous regime over riblets". In: *Journal of Fluid Mechanics* 678, pp. 317–347.

Gharib, Morteza and Alexander Weigand (1996). "Experimental studies of vortex disconnection and connection at a free surface". In: *Journal of Fluid Mechanics* 321, pp. 59–86.

Golovin, Kevin B et al. (2016). "Bioinspired surfaces for turbulent drag reduction". In: *Philosophical Transactions of the Royal Society A: Mathematical, Physical and Engineering Sciences* 374.2073, p. 20160189.

Hino, Mikio et al. (1983). "Experiments on the turbulence statistics and the structure of a reciprocating oscillatory flow". In: *Journal of Fluid Mechanics* 131, pp. 363–400.

Hinze, JO (1975). "Turbulence McGraw-Hill". In: *New York* 218, p. 457.

Hussain, Abul Khair Muhammad Fazle and William C Reynolds (1970). "The mechanics of an organized wave in turbulent shear flow". In: *Journal of Fluid Mechanics* 41.2, pp. 241–258.

Jiménez, Javier and Alfredo Pinelli (1999). "The autonomous cycle of near-wall turbulence". In: *Journal of Fluid Mechanics* 389, pp. 335–359.

Kline, Stephen J et al. (1967). "The structure of turbulent boundary layers". In: *Journal of Fluid Mechanics* 30.4, pp. 741–773.

Launder, BE (1964). "Laminarization of the turbulent boundary layer in a severe acceleration". In: *Journal of Applied Mechanics* 31.4, pp. 707–708.

Le, Hung, Parviz Moin, and John Kim (1997). "Direct numerical simulation of turbulent flow over a backward-facing step". In: *Journal of fluid mechanics* 330, pp. 349–374.

Lighthill, MJ (1963). *Boundary layer theory*.

Lu, Jiacai, Arturo Fernández, and Gretar Tryggvason (2005). "The effect of bubbles on the wall drag in a turbulent channel flow". In: *Physics of Fluids* 17.9, p. 095102.

Lumley, John L (1977). "Drag reduction in two phase and polymer flows". In: *The Physics of Fluids* 20.10, S64–S71.

Meng, James CS and James S Uhlman (1989). "Microbubble Formulation and Splitting in a Turbulent Boundary Layer for Turbulenee Reduction". In: *Advances in Fluid Dynamics*. Springer, pp. 168–217.

Millikan, Clark B (1939). "A critical discussion of turbulent flow in channels and circular tubes". In: *Proc. 5th Int. Congress on Applied Mechanics (Cambridge, MA, 1938)*. Wiley, pp. 386–392.

Mukund, R et al. (2006). "Relaminarization in highly favourable pressure gradients on a convex surface". In: *Journal of Fluid Mechanics* 566, pp. 97–115.

Narasimha, R and KR Sreenivasan (1979). "Relaminarization of fluid flows". In: *Advances in applied mechanics*. Vol. 19. Elsevier, pp. 221–309.

Narayanan, MA Badri and V Ramjee (1969). "On the criteria for reverse transition in a two-dimensional boundary layer flow". In: *Journal of Fluid Mechanics* 35.2, pp. 225–241.

Ou, Jia and Jonathan P Rothstein (2005). "Direct velocity measurements of the flow past drag-reducing ultrahydrophobic surfaces". In: *Physics of Fluids* 17.10, p. 103606.

Park, Hyungmin, Guangyi Sun, et al. (2014). "Superhydrophobic turbulent drag reduction as a function of surface grating parameters". In: *Journal of Fluid Mechanics* 747, pp. 722–734.

Pope, Stephen B (2001). *Turbulent flows*.

Procaccia, Itamar, Victor S L'vov, and Roberto Benzi (2008). "Colloquium: Theory of drag reduction by polymers in wall-bounded turbulence". In: *Reviews of Modern Physics* 80.1, p. 225.

Raffel, Markus et al. (2018). *Particle image velocimetry: a practical guide*. Springer.

Reynolds, WC and AKMF Hussain (1972). "The mechanics of an organized wave in turbulent shear flow. Part 3. Theoretical models and comparisons with experiments". In: *Journal of Fluid Mechanics* 54.2, pp. 263–288.

Rothstein, Jonathan P (2010). "Slip on superhydrophobic surfaces". In: *Annual Review of Fluid Mechanics* 42, pp. 89–109.

Schraub, Frederic Anthony and Stephen Jay Kline (1965). *A study of the structure of the turbulent boundary layer with and without longitudinal pressure gradients*. Tech. rep. STANFORD UNIV CA THERMOSCIENCES DIV.

Seo, J, R García-Mayoral, and A Mani (2015). "Pressure fluctuations and interfacial robustness in turbulent flows over superhydrophobic surfaces". In: *Journal of Fluid Mechanics* 783, pp. 448–473.

Skaare, Per Egil and Per-åge Krogstad (1994). "A turbulent equilibrium boundary layer near separation". In: *Journal of Fluid Mechanics* 272, pp. 319–348.

Sreenivasan, KR (1982). "Laminarescent, relaminarizing and retransitional flows". In: *Acta Mechanica* 44.1-2, pp. 1–48.

Stratford, BS (1959). "An experimental flow with zero skin friction throughout its region of pressure rise". In: *Journal of Fluid Mechanics* 5.1, pp. 17–35.

Tennekes, Hendrik, John Leask Lumley, JL Lumley, et al. (1972). *A first course in turbulence*. MIT press.

Townsend, AA (1961). "Equilibrium layers and wall turbulence". In: *Journal of Fluid Mechanics* 11.1, pp. 97–120.

Townsend, AAR (1980). *The structure of turbulent shear flow*. Cambridge university press.

Verschoof, Ruben A et al. (2016). "Bubble drag reduction requires large bubbles". In: *Physical review letters* 117.10, p. 104502.

Warnack, D and HH Fernholz (1998). "The effects of a favourable pressure gradient and of the Reynolds number on an incompressible axisymmetric turbulent boundary layer. Part 2. The boundary layer with relaminarization". In: *Journal of Fluid Mechanics* 359, pp. 357–381.

White, Christopher M and M Godfrey Mungal (2008). "Mechanics and prediction of turbulent drag reduction with polymer additives". In: *Annu. Rev. Fluid Mech.* 40, pp. 235–256.

Appendix A

APPENDIX I: DERIVATION OF PHASE-AVERAGED ACCELERATION FIELD

Consider the incompressible Navier-Stokes equation:

$$\frac{\partial U_i}{\partial t} + U_j \frac{\partial U_i}{\partial x_j} = -\frac{\partial P}{\partial x_j} + \frac{1}{Re}\frac{\partial^2 U_i}{\partial x_i \partial x_j} \tag{A.1}$$

$$\frac{\partial U_i}{\partial x_i} = 0 \tag{A.2}$$

By substituting $U_i = \overline{U}_i + \widetilde{U}_i + u_i'$ and $P = \overline{P} + \widetilde{P} + p'$ into equation A.1, we get:

$$\frac{\partial\left(\overline{U}_i + \widetilde{U}_i + u_i'\right)}{\partial t} + \left(\overline{U}_j + \widetilde{U}_j + u_j'\right)\frac{\partial\left(\overline{U}_i + \widetilde{U}_i + u_i'\right)}{\partial x_j} = -\frac{\partial\left(\overline{P} + \widetilde{P} + p'\right)}{\partial x_j}$$
$$+ \frac{1}{Re}\frac{\partial^2\left(\overline{U}_i + \widetilde{U}_i + u_i'\right)}{\partial x_i \partial x_j} \tag{A.3}$$

Expanding the left hand side of equation A.3, we get:

$$\frac{\partial\left(\overline{U}_i + \widetilde{U}_i\right)}{\partial t} + \left(\overline{U}_j + \widetilde{U}_j\right)\frac{\partial\left(\overline{U}_i + \widetilde{U}_i\right)}{\partial x_j} + \left(\overline{U}_j + \widetilde{U}_j\right)\frac{\partial\left(u_i'\right)}{\partial x_j} + \left(u_j'\right)\frac{\partial\left(u_i'\right)}{\partial x_j}$$
$$+ \left(u_j'\right)\frac{\partial\left(\overline{U}_i + \widetilde{U}_i\right)}{\partial x_j} = -\frac{\partial\left(\overline{P} + \widetilde{P} + p'\right)}{\partial x_j} + \frac{1}{Re}\frac{\partial^2\left(\overline{U}_i + \widetilde{U}_i + u_i'\right)}{\partial x_i \partial x_j} \tag{A.4}$$

Utilizing the following properties of phase-averaging operation, we have:

$$\langle u_i'\rangle = 0, \left\langle \overline{U}_i \right\rangle = 0, \langle p'\rangle = 0 \tag{A.5}$$

Taking time-averaging and then phase-averaging of the continuity condition shown in equation A.2, we get:

$$\frac{\partial \overline{U}_i}{\partial x_i} = \frac{\partial \widetilde{U}_i}{\partial x_i} = \frac{\partial u'_i}{\partial x_i} = 0 \tag{A.6}$$

Substituting equations in A.5 and A.6 into equation A.4, we get the phase-averaged momentum equation A.4:

$$\frac{\partial \left(\widetilde{U}_i \right)}{\partial t} + \overline{U}_j \frac{\partial \overline{U}_i}{\partial x_j} + \overline{U}_j \frac{\partial \widetilde{U}_i}{\partial x_j} + \widetilde{U}_j \frac{\partial \overline{U}_i}{\partial x_j} + \widetilde{U}_j \frac{\partial \widetilde{U}_i}{\partial x_j} + \frac{\partial \left\langle u'_i u'_j \right\rangle}{\partial x_j} =$$
$$- \frac{\partial (\overline{P} + \widetilde{P})}{\partial x_j} + \frac{1}{Re} \left(\frac{\partial^2 \overline{U}_i}{\partial x_j \partial x_j} + \frac{\partial^2 \widetilde{U}_i}{\partial x_j \partial x_j} \right) \tag{A.7}$$

Collecting items, equation A.7 is simplified to:

$$\frac{\partial \left(\widetilde{U}_i \right)}{\partial t} + \left(\overline{U}_j + \widetilde{U}_j \right) \frac{\partial \left(\overline{U}_i + \widetilde{U}_i \right)}{\partial x_j} + \frac{\partial \left\langle u'_i u'_j \right\rangle}{\partial x_j} = - \frac{\partial (\overline{P} + \widetilde{P})}{\partial x_j} + \frac{1}{Re} \left(\frac{\partial^2 \overline{U}_i}{\partial x_j \partial x_j} + \frac{\partial^2 \widetilde{U}_i}{\partial x_j \partial x_j} \right) \tag{A.8}$$

the phase-averaged acceleration is the left hand side of equation A.7. Using U and V to represent streamwise and wall-normal velocity, the phase-averaged accelerations are shown in equations in A.9:

$$\frac{D(\widetilde{U})}{Dt} = \frac{\partial(\widetilde{U})}{\partial t} + (\overline{U} + \widetilde{U})\frac{\partial(\overline{U}+\widetilde{U})}{\partial x} + (\overline{V} + \widetilde{V})\frac{\partial(\overline{U}+\widetilde{U})}{\partial y} + \frac{\partial \langle u'^2 \rangle}{\partial x} + \frac{\partial \langle u'v' \rangle}{\partial y}$$
$$\frac{D(\widetilde{V})}{Dt} = \frac{\partial(\widetilde{V})}{\partial t} + (\overline{U} + \widetilde{U})\frac{\partial(\overline{V}+\widetilde{V})}{\partial x} + (\overline{V} + \widetilde{V})\frac{\partial(\overline{V}+\widetilde{V})}{\partial y} + \frac{\partial \langle v'^2 \rangle}{\partial y} + \frac{\partial \langle u'v' \rangle}{\partial x} \tag{A.9}$$

A p p e n d i x   B

APPENDIX II: ENERGY PRODUCTION IN TBL

The TBL energy production terms are given in the kinetic energy equations. In canonical flat plate TBL, with Reynolds decomposition (i.e., $U_i = \overline{U}_i + u'_i$, $P = \overline{P} + p'$), the mean flow kinetic energy equation and the turbulent kinetic energy equation are shown in equation B.1 and B.2:

$$
\left[\frac{\partial}{\partial t} + \overline{U}_i \frac{\partial}{\partial x_j} \right] K = \frac{\partial}{\partial x_j} \left\{ -\frac{1}{\rho} \left(\overline{PU_i} \right) \delta_{ij} - \frac{1}{2} \left(\overline{u'_i u'_j} \right) \overline{U}_i + \nu \left(\left[\frac{\partial \overline{U}_i}{\partial x_j} + \frac{\partial \overline{U}_j}{\partial x_i} \right] U_i \right) \right\}
$$
$$
+ \left(\boldsymbol{\overline{u'_i u'_j}} \right) \boldsymbol{\frac{\partial U_i}{\partial x_j}} - \frac{1}{2} \nu \left[\frac{\partial \overline{U}_i}{\partial x_j} + \frac{\partial \overline{U}_j}{\partial x_i} \right]
$$

(B.1)

where K is the mean flow kinetic energy ($K = \frac{1}{2} \overline{U_i U_i}$).

$$
\left[\frac{\partial}{\partial t} + \overline{U}_j \frac{\partial}{\partial x_j} \right] k = \frac{\partial}{\partial x_j} \left\{ -\frac{1}{\rho} (\overline{p' u'_i}) \delta_{ij} - (\overline{k u_j}) + \nu \left(\left[\frac{\partial \overline{u'_i}}{\partial x_j} + \frac{\partial \overline{u'_j}}{\partial x_i} \right] u'_i \right) \right\}
$$
$$
- \boldsymbol{\overline{u'_i u'_j}} \boldsymbol{\frac{\partial U_i}{\partial x_j}} - \frac{1}{2} \nu \left[\frac{\partial \overline{u'_i}}{\partial x_j} + \frac{\partial \overline{u'_j}}{\partial x_i} \right]
$$

(B.2)

where k is the turbulent kinetic energy ($k = \frac{1}{2} \overline{u'_i u'_i}$).

It can be seen that the turbulent kinetic energy production (TKP, highlighted in bold font) flips sign in the mean kinetic energy equation and turbulent kinetic energy equation. Therefore it represents the energy exchange rate between the mean flow and the turbulent flow. Positive $-\overline{u'_i u'_j} \frac{\partial U_i}{\partial x_j}$ represents energy is transferred from the mean motion to the turbulent motion and vice versa.

In the presence of periodic perturbations, the flow field can be triple-decomposed, i.e., $U_i = \overline{U}_i + \widetilde{U}_i + u'_i$ and $P = \overline{P} + \widetilde{P} + p'$. The total kinetic energy with triple de-composition is expressed as: $K_{total} = \frac{1}{2} (\overline{U}_i \overline{U}_i + \widetilde{U}_i \widetilde{U}_i + \overline{u'_i u'_i})$. The kinetic energy

equations for the mean flow motion, oscillatory motion and turbulent motion derived by W. Reynolds and A. Hussain (1972) and are shown in equation B.3 - B.5.

$$
\frac{D}{Dt}\left(\frac{1}{2}\overline{U}_i\overline{U}_i\right) = -\frac{\partial \overline{PU}_i}{\partial x_i} - \left(-\overline{u_i'u_j'} - \overline{\widetilde{U}_i\widetilde{U}_j}\right)\frac{\partial \overline{U}_i}{\partial x_j} - \frac{\partial}{\partial x_j}\left[\overline{U}_i\left(\overline{u_i'u_j'} + \overline{\widetilde{U}_i\widetilde{U}_j}\right)\right]
$$
$$
+ \frac{1}{Re}\frac{\partial}{\partial x_j}\left[\overline{U}_i\left(\frac{\partial \overline{U}_i}{\partial x_j} + \frac{\partial \overline{U}_j}{\partial x_i}\right)\right] - \frac{1}{2Re}\left(\frac{\partial \overline{U}_i}{\partial x_j} + \frac{\partial \overline{U}_j}{\partial x_i}\right)\left(\frac{\partial \overline{U}_i}{\partial x_j} + \frac{\partial \overline{U}_j}{\partial x_i}\right)
$$
$$(B.3)$$

$$
\frac{D}{Dt}\left(\overline{\widetilde{U}_i\widetilde{U}_i}\right) = -\frac{\partial}{\partial x_j}\left[\overline{\widetilde{U}_j\left(\widetilde{P} + \frac{1}{2}\widetilde{U}_i\widetilde{U}_i\right)}\right] + \left(-\overline{\widetilde{U}_i\widetilde{U}_j}\right)\frac{\partial \overline{U}_i}{\partial x_j}
$$
$$
- \overline{\left(-\left\langle u_i'u_j'\right\rangle\right)\frac{\partial \widetilde{U}_i}{\partial x_j}} - \frac{\partial}{\partial x_j}\left[\overline{\widetilde{U}_i\left\langle u_i'u_j'\right\rangle}\right]
$$
$$
+ \frac{1}{Re}\frac{\partial}{\partial x_j}\left[\overline{\widetilde{U}_i\left(\frac{\partial \widetilde{U}_i}{\partial x_j} + \frac{\partial \widetilde{U}_j}{\partial x_i}\right)}\right] - \frac{1}{2Re}\overline{\left(\frac{\partial \widetilde{U}_i}{\partial x_j} + \frac{\partial \widetilde{U}_j}{\partial x_i}\right)\left(\frac{\partial \widetilde{U}_i}{\partial x_j} + \frac{\partial \widetilde{U}_j}{\partial x_i}\right)}
$$
$$(B.4)$$

$$
\frac{D}{Dt}\left(\frac{1}{2}\overline{u_i'u_i'}\right) = -\frac{\partial}{\partial x_j}\left[\overline{u_j'\left(p' + \frac{1}{2}u_i'u_i'\right)}\right] + \left(-\overline{u_i'u_j'}\right)\frac{\partial \overline{U}_i}{\partial x_j}
$$
$$
+ \left(-\overline{\left\langle u_i'u_j'\right\rangle}\right)\frac{\partial \widetilde{U}_i}{\partial x_j} - \overline{\widetilde{U}_j\frac{\partial}{\partial x_j}\left\langle\frac{1}{2}u_i'u_i'\right\rangle}
$$
$$
+ \frac{1}{Re}\frac{\partial}{\partial x_j}\overline{\left[u_i'\left(\frac{\partial u_i'}{\partial x_j} + \frac{\partial u_j'}{\partial x_i}\right)\right]} - \frac{1}{2Re}\overline{\left(\frac{\partial u_i'}{\partial x_j} + \frac{\partial u_j'}{\partial x_i}\right)\left(\frac{\partial u_i'}{\partial x_j} + \frac{\partial u_j'}{\partial x_i}\right)}
$$
$$(B.5)$$

The generalized kinetic energy production terms (KP_{MT}, KP_{MO} and KP_{OT}) are therefore defined as follows:

$$
KP_{MT} = \left(-\overline{u_i'u_j'}\right)\frac{\partial \overline{U}_i}{\partial x_j}, KP_{MO} = \left(-\overline{\widetilde{U}_i\widetilde{U}_j}\right)\frac{\partial \overline{U}_i}{\partial x_j}, KP_{OT} = \left(-\left\langle u_i'u_j'\right\rangle\right)\frac{\partial \widetilde{U}_i}{\partial x_j} \quad (B.6)
$$

where 'M' represents mean motion, 'O' represents the oscillatory motion and 'T' represents turbulent motion) are highlighted by bold font in the equations. Positive KP_{MT}, KP_{MO} and KP_{OT} represents energy is transferred from mean motion to turbulent motion, from mean motion to oscillatory motion and from oscillatory motion

to turbulent motion. In the same function role as TKP in canonical TBL, the three generalized kinetic energy production terms are only responsible for redistributing energy within TBL and do not generate or dissipate energy.

A p p e n d i x   C

APPENDIX III: MODELING THE AIR-FILM OSCILLATION

Influenced by a broad spectrum of contributing parameters, the air-film oscillation in TBL is highly non-linear. This nature makes constructing a mathematical model for the air-film dynamic oscillation in TBL extremely challenging. However, a simplified force balance model might provide insights for the essential physical mechanisms of air-film/TBL dynamic interaction. This appendix discusses several critical force quantities that contribute to the air-film dynamic oscillation. To compare their relative significance, the ratios of these force quantities which are essentially non-dimensional parameters is discussed as well.

C.1   Force Balance Analysis for Air-film Oscillation

Before the detailed force balance analysis, the air-film oscillation is first qualitatively described. With pressure modulation, the air-film oscillation is driven by the dynamic pressure inside the surface dimples and resisted by the surface tension effect on the air-film interface. The surface tension effect depends on air-film radius of curvature, which tends to minimize the air-film surface area. A radial viscous force also resists the air-film expansion or contraction because of water viscosity. In addition, the large density difference between air and water results in buoyancy force on the air-films. With the current configuration in which air-films face downward, the buoyancy force always resists air-film expansion and favors its contraction. Furthermore, the air-films are subjected to the shear and inertial force of TBL.

The dynamic modulation air-films induce inertia forces in the near-region of air-films by periodically accelerating and decelerating the surrounding liquid. Therefore, an unsteady inertia and a quasi-steady inertia force are induced in the vicinity of air-films. The unsteady inertia force is the added mass effect associated with the acceleration and deceleration. The quasi-steady inertia is associated with the periodically time-varying velocity following the air-film periodic oscillation.

The force balance analysis is conducted along the wall-normal and streamwise direction. Along the wall-normal direction, the buoyancy force, radial viscous force, surface tension effect as well as the induced unsteady/quasi-steady inertia forces can make a difference. Along the streamwise direction, all the above-mentioned force

quantities are still critical except the buoyancy force. Additionally, the TBL shear and inertia force could distort air-films along the streamwise direction. The force balance along the two directions are coupled together. Some force quantities such as surface tension effect, depends on the air-film's dynamic curvature. The dynamic coupling between force quantities makes things complicated.

Because all air-films are identical and modulated in phase, the entire air-film array can be represented as a single air-film. To simplify the model, the air-film is modeled as a part of spherical surface that is attached to the edge of circular shaped surface dimple, as shown in figure C.1. The surface has a radius R and the surface dimple radius is r. By assuming the air-film height is h, the air-film radius R can be expressed as $R = \frac{r^2+h^2}{2h}$ by Pythagorean theorem. Because the air-film is pinned at the edge of dimple, the air-film expansion and contraction only result in the air-film height change. Therefore, the air-film oscillation velocity and acceleration can be roughly estimated as $\frac{dh}{dt}$ and $\frac{d^2h}{dt^2}$.
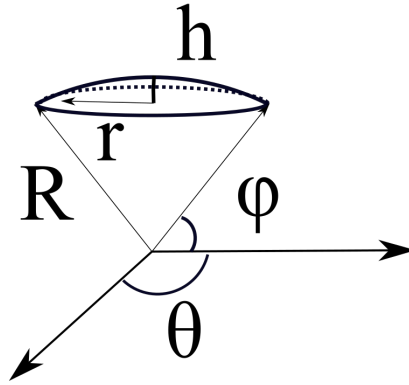
Figure C.1: Air-film as a part of spherical surface. The air-film radius is R and surface dimple radius is r. Air-film height is h.

The force quantities' relative order-of-magnitudes shortlist the critical force quantities for air-film dynamic oscillation. Integrating the above-mentioned force quantities over the air-film surface gives the following integrated forces: pressure modulation force f_p, surface tension effect f_γ, buoyancy force f_g, radial viscous force f_τ, TBL inertia and shear force f_{i0} and $f_{\tau 0}$ as well as the induced steady and unsteady fluid inertia force I_s and I_u. The detailed integration is shown below:

1. Pressure modulation force f_p:

$$f_p = \int_0^{2\pi} R^2 \int_{\theta_1}^{\pi-\theta_1} (p_0 + \Delta p \sin(\omega t)) \sin(\phi) d\phi d\theta$$

$$= (p_0 + \Delta p \sin(\omega t)) \pi \frac{r^4 - h^4}{2h^2}$$

(C.1)

where $p_0 + \Delta p \sin(\omega t)$ is the air-film inner pressure.

2. Surface tension effect:

$$f_\gamma = \int_0^{2\pi} R^2 \int_{\phi_1}^{\pi-\phi_1} \frac{2\gamma}{R} \sin(\phi) d\phi d\theta$$

$$= 8\pi\gamma R \cos(\phi_1) |$$

(C.2)

Simplifying with the relation $\cos(\phi_1) = \frac{r^2-h^2}{r^2+h^2}$, we get:

$$f_\gamma = 4\pi\gamma \frac{r^2 - h^2}{h}$$

(C.3)

3. Buoyancy force f_g:

$$f_g = \rho_L g \int_{R-h}^{R} r'^2 \int_0^{2\pi} \int_{\phi_1}^{\pi-\phi_1} \sin(\phi) d\phi d\theta dr'$$

$$= \rho_L g \pi \frac{3r^2+h^2}{2h} \frac{r^2-h^2}{r^2+h^2}$$

(C.4)

where ρ_L is the water density and g is gravitational acceleration.

4. Radial viscous force:

The radial viscous force depends on the radial velocity gradient $\frac{dV_r}{dr'}$, where r' is the distance from the center of air-film (as part of a sphere). Due to the air-film spherical symmetry, the radial viscous stress resists τ_{rr} is expressed as:

$$\tau_{rr} = -2\mu \frac{dV_r}{dr'}$$

(C.5)

Where ν is the dynamic viscosity. By continuity, the radial velocity V_r at some distance r' from the virtual center of air-film is related to the air-film oscillation velocity $\frac{dh}{dt}$:

$$V_r r'^2 = \frac{dh}{dt} R^2$$

(C.6)

Substitute V_r into the expression for τ_{rr}:

$$\frac{dV_r}{dr'} = -2\left(\frac{dh}{dt}R^2\right)\frac{1}{r'^3}$$
$$\tau_{rr}(r') = 4\mu\frac{dh}{dt}\frac{R^2}{r'^3}$$

(C.7)

Therefore, the radial viscous force is:

$$f_\tau = \int_0^{2\pi} R^2 \int_{\phi_1}^{\pi-\phi_1} \tau_{rr|r'=R} \sin(\phi)d\phi d\theta$$
$$= 4\pi\mu\frac{dh}{dt}\frac{r^2-h^2}{h}$$

(C.8)

5. The TBL inertia and shear force:

The TBL inertia and shear force deforms the air-film along the streamwise direction. By approximating the effective cross-sectional area of air-film as a half oval, the TBL inertia force f_{i0} is estimated as the flow inertia multiplying the air-film cross-sectional area:

$$f_{i0} = \rho u_o^2 \pi r h$$

(C.9)

where u_0 is the characteristic velocity. The TBL shear force can be estimated by integrating the shear stress over the air-film surface. With the approximation that local shear stress equal to $\frac{\mu u_0}{h}$, we have:

$$f_{\tau 0} = \int_0^{2\pi} R^2 \int_{\phi_1}^{\pi-\phi_1} \mu\frac{u_0}{h} \sin(\phi)d\phi d\theta$$
$$= \pi\mu u_0 \frac{r^4-h^4}{2h^3}$$

(C.10)

The ratio of TBL inertia force over shear force is:

$$\frac{f_{i0}}{f_{\tau 0}} = \frac{u_0 r h^4}{\nu\left(r^4-h^4\right)} \sim o\left(\frac{u_0 r}{\nu}\right)$$

(C.11)

Since $r \sim O(\delta)$ and $u_0 \sim O(u_\tau)$, $\frac{f_{i0}}{f_{\tau 0}} \sim O\left(\frac{u_\tau \delta}{\nu}\right) = Re_\tau$. Because Re_τ is large in TBL, f_{i0} dominates over $f_{\tau 0}$.

6. The quasi-steady inertia force:

Integrating the air-film oscillating velocity $\frac{dh}{dt}$ over the air-film surface, we have:

$$I_S = \int_0^{2\pi} R^2 \int_{\phi_1}^{\pi-\phi_1} \rho\left(\frac{dh}{dt}\right)^2 \sin(\phi)d\phi d\theta$$
$$= \rho\pi\frac{r^4-h^4}{h^2}\left(\frac{dh}{dt}\right)^2$$

(C.12)

7. The unsteady inertia force:

the unsteady inertia force is associated with some volume of fluid that is accelerated. Assume the fluid within a thickness of δ is accelerated (as can be seen in figure 5.1), therefore:

$$
\begin{aligned}
I_u &= \int_0^{2\pi} R^2 \int_{\phi_1}^{\pi-\phi_1} \rho \frac{d^2 h}{dt^2} h \sin(\phi) d\phi d\theta \\
&= \rho\pi \frac{(r^2-h^2)(r^2+h^2)}{h} \frac{d^2 h}{dt^2}
\end{aligned}
\tag{C.13}
$$

C.2 Non-dimensional Parameters for Air-film Oscillation

The ratio of any two force quantities define a non-dimensional parameter. Due to the large number of force quantities involved, only a few representative non-dimensional parameters will be listed below:

- Unsteady/quasi-steady Webber number as the ratio of unsteady/quasi-steady inertia force over surface tension effect:

$$
We_u = \frac{I_u}{f_\gamma}, We_s = \frac{I_s}{f_\gamma}
\tag{C.14}
$$

- Unsteady/quasi-steady Froude number as the ratio of unsteady/quasi-steady inertia over buoyancy force:

$$
Fr_u = \frac{I_u}{f_g}, Fr_s = \frac{I_s}{f_g}
\tag{C.15}
$$

- Bond number as the ratio of buoyancy force over surface tension effect:

$$
Bo = \frac{f_g}{f_\gamma}
\tag{C.16}
$$

- Strouhal number as the ratio of unsteady inertia over quasi-steady inertia:

$$
St = \frac{I_u}{I_s}
\tag{C.17}
$$

- Reynolds number based on the radial viscous force as the ratio of quasi-steady inertia over radial viscous force:

$$
Re_r = \frac{I_u}{f_\tau}
\tag{C.18}
$$

- Womersley number as the ratio of unsteady inertia over radial viscous force:

$$\alpha_r^2 = \frac{I_u}{f_\tau} \tag{C.19}$$

- Webber number based on the TBL inertia force as the ratio of TBL inertia force over surface tension effect:

$$We_0 = \frac{f_{i0}}{f_\gamma} \tag{C.20}$$

- TBL Reynolds number as the ratio of TBL inertia over viscous shear force:

$$Re_\tau \sim \frac{f_{i0}}{f_{\tau 0}} \tag{C.21}$$

- Strouhal number based on the air-film quasi-steady inertia and TBL inertia:

$$St_{s0} = \frac{I_s}{f_{i0}} = \frac{\left(\frac{dh}{dt}\right)^2}{u_0^2} \tag{C.22}$$

u_0 is picked to be the TBL velocity at air-film height (h) away from the wall, thus:

$$St_{s0} \sim \left(\frac{\frac{dh}{dt}}{\overline{U}_{|y=h}}\right)^2 \tag{C.23}$$

- Strouhal number based on the air-film unsteady inertia and TBL inertia:

$$\begin{aligned} St_{u0} &= \frac{I_u}{f_{i0}} \\ &= \frac{2R\delta}{r}\frac{(r^2-h^2)}{h^2}\frac{\frac{d^2h}{dt^2}}{\left(\overline{U}_{|y=h}^2\right)} \end{aligned} \tag{C.24}$$

- Quasi-steady/Unsteady velocity ratios in TBL:

The oscillating air-films induce velocity and acceleration in TBL. In the near-wall region, besides the TBL inner velocity $u_{\tau 0}$, there also exists the oscillatory velocity $\frac{dh}{dt}$ and unsteady velocity associated with the acceleration $\frac{d^2h}{dt^2}\frac{1}{f}$, where f is the modulation frequency. Therefore, a quasi-steady and unsteady velocity ratio can be defined as:

$$I_{q0} = \frac{\frac{dh}{dt}}{u_{\tau 0}}, I_{u0} = \frac{d^2h}{dt^2}\frac{1}{f u_{\tau 0}} \tag{C.25}$$

C.3   Case Study

To have an idea about the values of non-dimensional parameters, the test case in which re-laminarization process is observed (shown in Chapter 7) is selectively analyzed. In that case, the baseline TBL frictional velocity $u_{\tau 0}$ is 0.02 m/s. The air-film base radius r is approximately 4 mm and air-film maximum height h is approximately 2 mm. Based on the DPIV measurements, $\overline{U}_{|y=h}$ is 0.2 m/s, the oscillatory velocity $\frac{dh}{dt}$ maximum magnitude is 0.15m/s and the oscillatory acceleration $\frac{d^2h}{dt^2}$ is 40 m/s^2.

The values of non-dimensional parameters are calculated using the expressions derived in Section C.2. The Bond number **Bo** is approximately 1, which indicates the surface tension effect and buoyancy force are of the same order of magnitude. The Strouhal number **St** is approximately 50, which indicates the unsteady inertia force dominates over the quasi-steady inertia force. The quasi-steady and unsteady Webber numbers are found to be approximately $We_s \sim 0.8$ and $We_u \sim 40$, respectively. Since the Bond number is approximately 1, the quasi-steady and unsteady Froude number (Fr_s and Fr_u) are of the same order-of-magnitude as We_s and We_u respectively. The non-dimensional parameter values indicate that the surface tension effect, buoyancy force, quasi-steady and unsteady inertia force are of similar order-of-magnitude. The Reynolds number associated with the radial viscous force Re_r is approximately 500 and the Womersley number α_r^2 is approximately 5000, indicating the viscous shear force is less significant than the quasi-steady/unsteady inertia forces. The quasi-steady and unsteady Strouhal number based on TBL inertia, St_{s0} and St_{u0}, are approximately 0.3 and 15 respectively, which indicates the TBL inertia force is comparable to the quasi-steady inertia but smaller than the unsteady inertia. In TBL, the quasi-steady velocity ratio I_{q0} is approximately 8 and unsteady velocity ratio I_{u0} is approximately 40, which shows the oscillatory quasi-steady/unsteady inertia force dominates over the TBL inner layer inertia force. In short summary, the important force quantities for the air-film dynamic oscillation include: pressure modulation force, surface tension effect, buoyancy force, quasi-steady/unsteady inertia force generated by oscillating air-films as well as TBL inertia force.